

Self-learning mechanical circuits

Vishal P. Patil^{1,†}, Ian Ho^{1,†}, Manu Prakash^{1,2,3,*}

¹*Department of Bioengineering, Stanford University, Stanford CA 94305 USA*

²*Department of Biology, Stanford University, Stanford CA 94305 USA*

³*Department of Oceans, Stanford University, Stanford CA 94305 USA*

[†] *Equal contributions*

** To whom correspondence should be addressed: manup@stanford.edu*

(Dated: April 19, 2023)

Computation, mechanics and materials merge in biological systems [1], which can continually self-optimize through internal adaptivity across length scales, from cytoplasm [2] and biofilms [3, 4] to animal herds [5]. Recent interest in such material-based computation [6–11] uses the principles of energy minimization, inertia and dissipation to solve optimization problems [12]. Although specific computations can be performed using dynamical systems [13–17], current implementations of material computation lack the ability to self-learn [6]. In particular, the inverse problem of designing self-learning mechanical systems which can use physical computations to continuously self-optimize remains poorly understood. Here we introduce the concept of self-learning mechanical circuits, capable of taking mechanical inputs from changing environments and constantly updating their internal state in response, thus representing an entirely mechanical information processing unit. Our circuits are composed of a new mechanical construct: an adaptive directed spring (ADS), which changes its stiffness in a directional manner, enabling neural network-like computations. We provide both a theoretical foundation and experimental realization of these elastic learning units and demonstrate their ability to autonomously uncover patterns hidden in environmental inputs. By implementing computations in an embodied physical manner, the system directly interfaces with its environment, thus broadening the scope of its learning behavior. Our results pave the way towards the construction of energy-harvesting, adaptive materials which can autonomously and continuously sense and self-optimize to gain function in different environments.

INTRODUCTION

Mechanical principles guide continual autonomous adaptivity in a range of biological systems [1, 2, 18–20]. At small scales, the interactions and reorganization of intracellular [21, 22] and intercellular [3] components have functional mechanical consequences [23], determining cellular contractility [24], screening stress [25], and encoding memory [26]. The behavior of larger living systems, such as animal herds [5] and collectives [27], has further inspired a variety of optimization algorithms which utilize their dynamics [28]. Due to its self-optimization across length scales, the structure and organization of biological matter has the potential to yield general design principles for self-learning materials. However, building such materials first requires isolating key self-learning mechanisms, in order to understand their functionality free from the complexity inherent within biological systems.

Adaptive abiotic materials can be engineered with tunable properties [11, 29], from amorphous solids [30–35] to deformable sheets [36, 37]. By integrating soft materials with external computational optimization, systems can also be designed to map specific inputs to target outputs, allowing for the construction of materials with desired mechanical properties [38–41] such as the ability to solve classification problems [42, 43]. In contrast, biological adaptive matter responds autonomously and continually to changing environments [44–46], without the need for a central controller or an external reset. These

examples raise the question of whether distributed, self-learning behavior can be embedded in purely mechanical systems, without electronics [16, 47]. Such purely mechanical forms of adaptivity, in which sensing and actuation are directly encoded in the mechanical domain, provide advantages for building monolithic, self-regulating structures [48].

Here we report the invention of self-learning mechanical circuits, which interact with their environment mechanically, and continually update their internal state as the environment changes. We define mechanical circuits to be composed of adaptive springs connected in network configurations, which learn by updating their own stiffness in response to various inputs. To mimic neural network-like computations, we additionally engineer these springs to be directed, so that their stiffness update depends upon which end of the spring experiences a greater force. To our knowledge, this construction is the first realization of an adaptive directed spring (ADS), and constitutes the fundamental unit of our mechanical circuits. By combining dynamical systems theory with an experimental realization of an ADS, we demonstrate that ADS networks can integrate information about a changing environment and modulate their behavior. Crucially, this learning behavior is embodied in the mechanical domain itself, allowing for environmental interaction unmediated by a separate sensory layer [49, 50]. We present a combinatorial design framework and a library of mechanical circuits that exhibit a broad range of self-learning behavior.

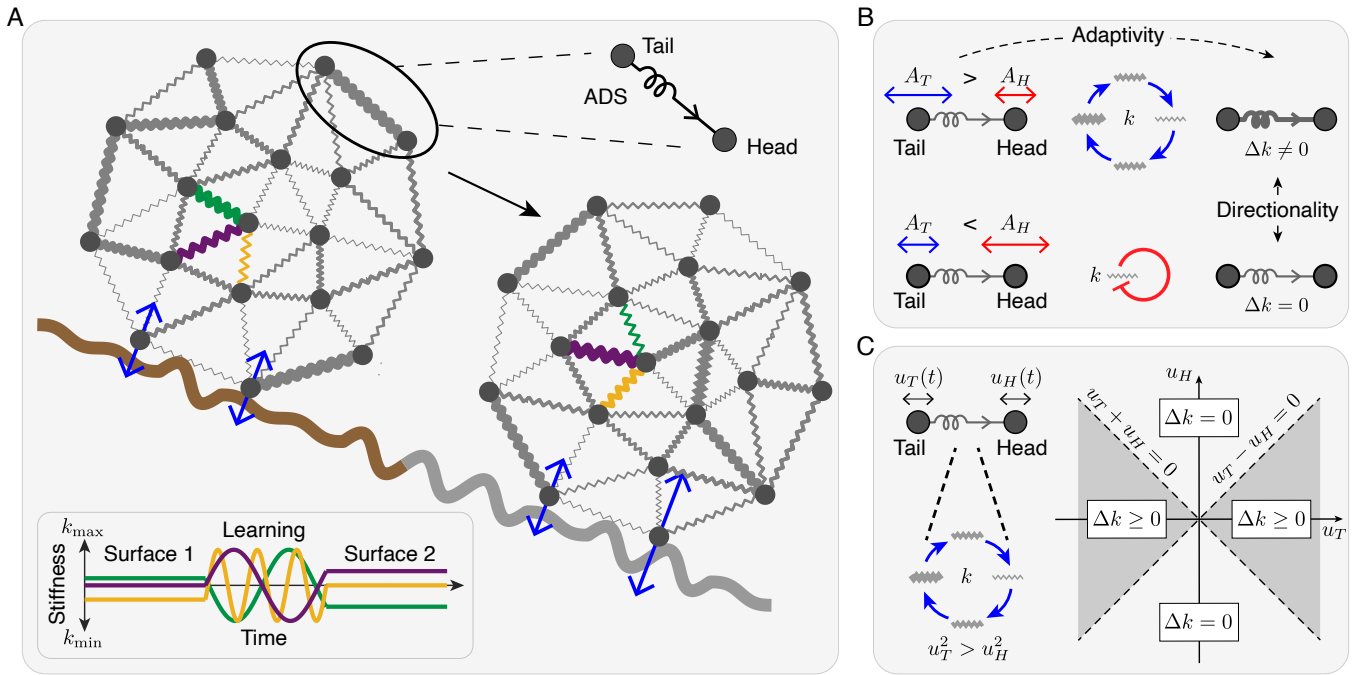


FIG. 1. **Theoretical conceptualization of a self-learning mechanical circuit** (A) Toy example of a self-learning mechanical circuit rolling over a textured surface (brown and grey curves). Our circuits are elastic networks composed of adaptive directed springs (ADSs), introduced below. The network experiences input forces from the surface roughness (blue arrows), and responds by changing its internal spring stiffness pattern (thickness of springs). When the surface patterning changes (grey curve), the network must learn a new stiffness pattern (inset graph). For continual learning, the springs must both stiffen and soften (inset graph). (B) We define the properties of an ADS axiomatically. Directionality requires an ADS to break symmetry and have a head and a tail. The update dynamics of an ADS depends on the amplitude of oscillation at its tail, A_T , and head A_H . Larger oscillations at the tail of the ADS (top left, $A_T > A_H$) cause the spring stiffness, k , to change cyclically (top row, center). Larger head oscillations (bottom left, $A_H > A_T$) leave the spring state unchanged. The learning behavior of an ADS mimics the dynamics of an artificial neural network. (C) Theoretical requirements of an ADS guide its construction. The ADS only updates its stiffness k if the tail oscillations $u_T(t)$, have a larger magnitude than the head oscillations, $u_H(t)$: update thus only occurs if $u_T^2 > u_H^2$ (left hand column). Visualizing this region on the (u_T, u_H) plane (right hand graph, shaded region) indicates that an ADS only updates when $u_T - u_H$ and $u_T + u_H$ have the same sign.

LEARNING IN ELASTIC NETWORKS

Consider a toy example of a purely mechanical self-learning elastic network that takes inputs from its environment, for example through interaction with a textured surface (Fig. 1A, brown and grey curves). In order to learn from and respond favorably to these periodic inputs, the network must be adaptive, changing its stiffness in response to input forces (Fig. 1A, blue arrows). Since our self-learning networks are purely mechanical, this adaptivity must be powered by the environmental forces themselves. The learned, internal state of the network can then be thought of as its spring stiffness pattern. To capture biological adaptivity, this learning process must additionally be continual: when the environment changes (Fig. 1A, brown and grey curves), the internal state of the network, as quantified by the stiffness pattern, must also change (Fig. 1A, bottom left). The state of the network should also reflect functionality, which will typically depend on context. For example, in the case of

a tumbling wheel (Fig. 1A), this internal network state could predictably dampen bumps on a road. This class of continual, adaptive behavior resembles artificial neural network dynamics [51]. Neuron activities correspond to node oscillations in our self-learning network (Fig. 1A), and the neural network edge weights correspond to spring stiffness. Our construction of self-learning networks is motivated by this analogy.

Neural networks work on the principle of information flow through directed graphs [52]. In order to implement neural networks purely in mechanical domains we need adaptive connectors, directional update rules and threshold non-linearities. The adaptive directed springs (ADSs) introduced here capture these properties (Fig. 1A,B). In elastic networks, adaptivity corresponds to changes in the spring stiffness k [53]. For continual adaptivity, the stiffness $k(t)$ of an ADS must be cyclic, implying that $k = k(\psi(t))$ for an auxiliary angular variable ψ . Directional update within an ADS is required for controlled information flow, akin to update rules in traditional neu-

ral networks [52, 54]. To achieve this, an ADS must break symmetry and have a tail end and a head end (Fig. 1B), which interact differently with the spring stiffness k . Since elastic networks take vector inputs, such as forces and displacements, there is a space of springs with different directional update rules (SI section IA). We choose the ADS to be the simplest such unit which can compare the motion of its two endpoints. More precisely, we define an ADS to update if and only if the parallel oscillation amplitude of the tail node, A_T , exceeds that of the head node, A_H (Fig. 1B). Taken together, the rules for adaptivity, directionality and threshold activation of an ADS are thus

$$k = k(\psi(t)) \quad \text{Continual adaptivity} \quad (1a)$$

$$\Delta k \neq 0 \quad \text{if} \quad |A_T| > |A_H| + \delta \quad \text{Directional adaptivity} \quad (1b)$$

$$\Delta k = 0 \quad \text{if} \quad |A_T| \leq |A_H| \quad \text{Self-regulation} \quad (1c)$$

$$|A_H| = \sigma(|A_T|, k), \quad |A_T| = \sigma(|A_H|, k) \quad \text{Activation} \quad (1d)$$

where σ is an activation non-linearity, and $\delta \geq 0$ is an additional threshold that can arise in physical implementations of an ADS (SI section IA). By balancing adaptivity (1a and 1b) and stability (1c), these axioms give rise to networks exhibiting continual self-learning behavior.

The ADS rules allow us to identify the internal degrees of freedom that an ADS must possess. For example, in order to display continual adaptivity (1a), an ADS must manifest an angular degree of freedom, ψ . The rules governing directionality (1b and 1c) can be similarly analyzed. In terms of the node displacements, $u_T(t)$, $u_H(t)$ (Fig. 1C), the directional update rules require the stiffness to change only when $u_T^2 - u_H^2 > 0$. Factorizing this condition implies that an ADS updates only when $u_T \pm u_H$ have the same sign (Fig. 1C). These quantities are captured by the spring extension $u_H - u_T$, and center of mass motion $u_H + u_T$. Constructing an ADS therefore hinges upon coupling spring extension and center of mass motion to spring stiffness k , via an angle ψ . These degrees of freedom can be realized using an elastic ring and a pendulum (SI section IB), motivating our physical implementation of an ADS.

PHYSICAL REALIZATION OF ADAPTIVE DIRECTED SPRINGS

Our physical realization of an ADS relies upon two mechanical gadgets: an elastic ring of non-uniform thickness provides a unit with variable stiffness, and a coupled spring-pendulum system harvests energy from the environment to enable adaptivity in a directional manner (Fig. 2A-C). Placing the system on a substrate addi-

tionally introduces contact friction, which implements a threshold function on the head and tail ends of the ADS (Fig. 2A). Taken together, an adaptive elastic unit, an energy harvester and a threshold friction, are the three ingredients which constitute the key components of our ADS, enabling it to satisfy all the properties of equation (1). For example, when subject to environmental forces, the stiffness of the ADS can change if the elastic ring rotates (Fig. 2A,B). Crucially, this rotation is coupled to the oscillations of the spring-pendulum system via a ratchet, which converts the energy of the pendulum into uni-directional rotation of the ring. Analyzing these mechanical gadgets mathematically explains how our ADS robustly realizes directional adaptivity.

The elastic ring angle, ψ (Fig. 2B), the pendulum angle, θ (Fig. 2C), and the spring extension, η , are the internal degrees of freedom of the ADS which give rise to adaptivity and directionality. The ring angle ψ determines the spring stiffness k , and is thus responsible for adaptivity. When compressed, the distance between points of highest curvature and thickness along the ring (Fig. 2B) determines the value of stiffness, yielding a relationship $k = k(\psi)$ (SI section IIIB). Next, we introduce a pendulum, which requires choosing a positive direction for its angle θ (Fig. 2A,C), and thereby breaks symmetry and contributes to directionality. The head and the tail of the spring are defined with respect to the positive θ direction (Fig. 2A,C). Examining the spring-pendulum system reveals that the head and tail ends also have dynamically distinct behavior. For example, stretching the spring from the tail node causes $\dot{\theta}, \dot{\eta} > 0$ (Fig. 1C, top left), whereas stretching from the head node leads to $\dot{\eta} > 0$ and $\dot{\theta} < 0$ (Fig. 1C, bottom left). More formally, the dynamics of θ, η are approximately (SI section IB)

$$\ddot{\eta} = -\ddot{u}_T + \ddot{u}_H, \quad 2\ell_p\ddot{\theta} = -\ddot{u}_T - \ddot{u}_H \quad (2)$$

where u_T, u_H are the tail and head node displacements (Fig. 2A), and ℓ_p is the pendulum length. In-phase motion of θ and $\dot{\eta}$ therefore occurs when the amplitude of the tail node exceeds the head node, but antiphase motion occurs otherwise (SI section IB). To satisfy the directional update rules, the ADS stiffness must therefore change only when $\dot{\theta}$ and $\dot{\eta}$ are oscillating in phase, which corresponds to $-u_T \pm u_H$ having the same sign over an oscillation cycle (Fig. 1C, right). We will achieve this by constructing an ADS whose stiffness updates only when $\dot{\theta}, \dot{\eta} > 0$.

To complete the ADS construction, we require an energy harvesting mechanism which uses the oscillations of the spring-pendulum system to update the spring stiffness whenever $\dot{\theta}, \dot{\eta} > 0$ (SI section IIA). We achieve this by coupling both θ and η to the elastic ring ψ , via a ratchet, so that the elastic ring exhibits uni-directional rotation, $\dot{\psi} \geq 0$, if $\dot{\eta}, \dot{\theta} > 0$. The ratchet itself is rigidly attached to a gear (Fig. 2D, top gear), which, upon rotation, engages the geared inner profile of the elastic ring

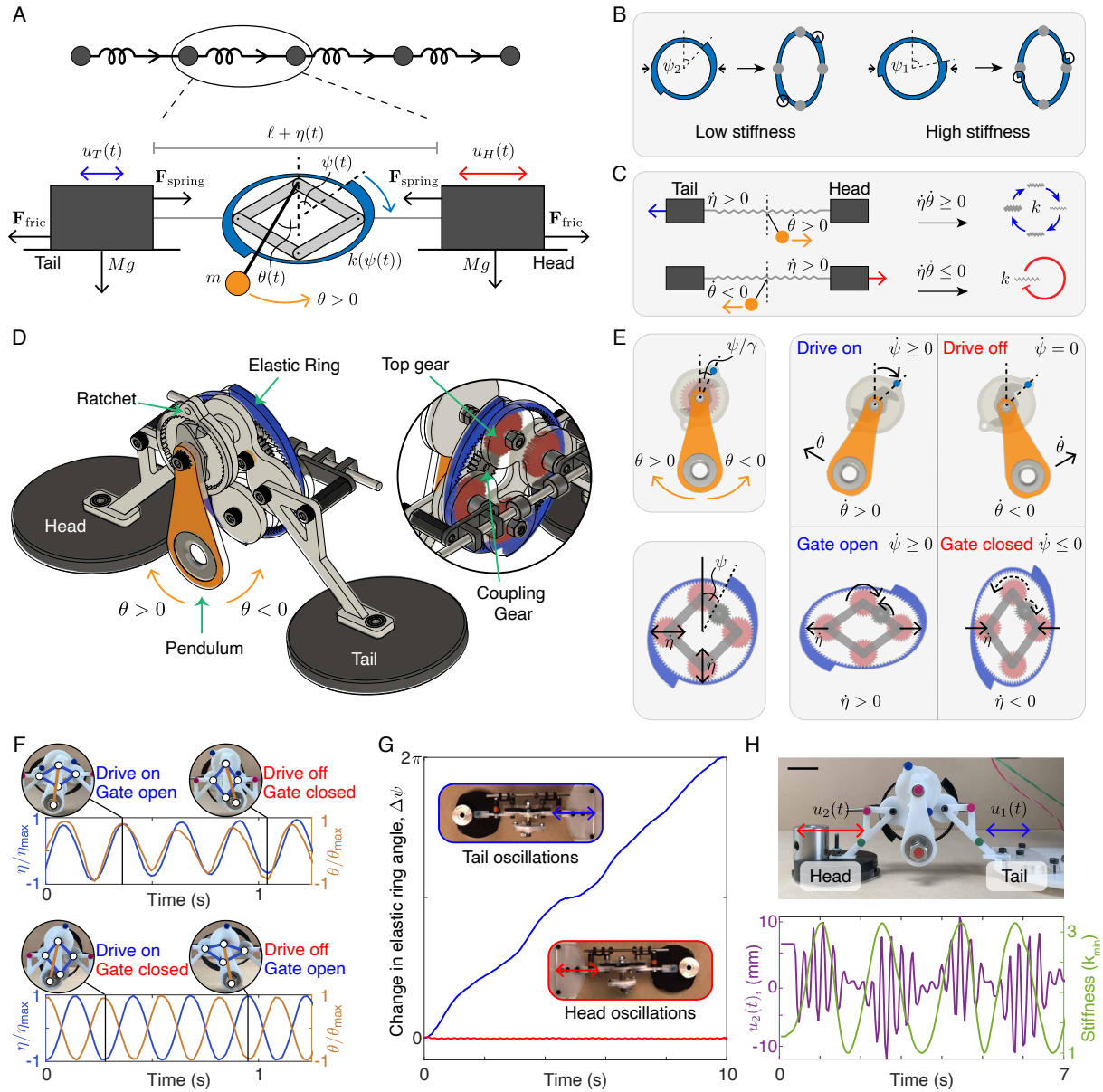


FIG. 2. Physical construction of adaptive directed springs. (A) Free body diagram of an ADS joining two nodes (grey rectangles). We implement an ADS by coupling a pendulum (orange) and an elastic ring of varying thickness (blue), mounted on a four-bar linkage (grey). The ring is ratcheted and can only rotate in one direction, $\dot{\psi} \geq 0$ (blue arrow). The spring stiffness, k is a function of ψ . The positive pendulum direction (orange arrow) points from tail to head by definition. The spring stiffness, k , depends on the node oscillations, u_T, u_H , through the pendulum angle, θ and the spring extension η . k updates only when $\dot{\eta}, \dot{\theta} > 0$. Coulomb friction acts as a threshold nonlinearity on the spring. (B) The force required to compress the elastic ring depends on ring angle ψ . The distance between the thickest portions of the deformed ring (black circles) and the portions under greatest strain (grey circles) determines spring stiffness. (C) The coupling between the pendulum, θ , and the spring extension, η , breaks symmetry in the ADS: $\dot{\theta}$ and $\dot{\eta}$ have the same sign if the tail end of the spring is moved (top row) but $\dot{\eta}\dot{\theta} \leq 0$ when the head end is moved (bottom row). For directionality, we need the stiffness k to update only when θ, η move in the same direction, or equivalently, $\dot{\psi} \geq 0$ when $\dot{\theta}, \dot{\eta} > 0$. (D,E) CAD rendering of our ADS implementation. The $\theta > 0$ direction points from tail to head. The ratchet is rigidly attached to the top gear (inset), which is coupled to the elastic ring (SI section IIA); all three objects rotate together, up to a gear ratio γ (E, first column). (E) The ring angle ψ responds differently to θ and η . When $\dot{\theta} > 0$ (top row), the pendulum (orange) engages the ratchet (drive on, $\dot{\psi} \geq 0$). The gear mechanism (bottom row) does not produce enough force to independently rotate the heavy ratchet, and instead functions as a gating mechanism. When the spring is stretched (compressed), the gear torques and constraints only permit the top gear to rotate clockwise (counterclockwise), forcing $\dot{\psi} \geq 0$ ($\dot{\psi} \leq 0$), and leading to the gate open (closed) state. Only the drive on, gate open state leads to spring update, $\dot{\psi} > 0$ (SI section IIA). (F,G) Oscillating a physical ADS from the tail (F, top row) produces in-phase η, θ motions, whereas head oscillations (F, bottom row) cause η, θ to be in antiphase (as in C). In-phase motion hits the drive on, gate open state ($\dot{\theta}, \dot{\eta} > 0$), leading to $\dot{\psi} > 0$ (G, blue curve). (H) Elastic response of a physical ADS under input tail oscillations displays the hallmarks of adaptivity and thresholding (movie S1). The changing stiffness (green curve) causes the output amplitude (purple curve) to increase and decrease. Scale bar 2 cm.

(Fig. 2D). The gear ratio, γ (Fig. 2E, top left), between these two objects determines the rotation rate of the elastic ring. Rotating the ratchet thus rotates both the top gear and the elastic ring (SI section IIA), increasing the angle ψ and updating the spring stiffness (Fig. 2E).

The update behavior of an ADS can be understood by breaking down its dynamics into four states according to the signs of $\dot{\theta}$ and $\dot{\eta}$ (Fig. 2E). Depending on sign, the pendulum oscillation and spring extension have the effect of driving and gating the ratchet (Fig. 2E). When $\dot{\theta} > 0$, the pendulum engages the ratchet, driving its rotation and increasing ψ , whereas if $\dot{\theta} < 0$, the ratchet remains stationary and $\dot{\psi} = 0$ (Fig. 2E, top row). In contrast, the stretching of the spring does not produce enough torque to directly drive the ratchet, due to its large mass. Spring stretching instead enforces a gear rotation pattern which either permits or prevents rotation of the ratchet (Fig. 2E, bottom row). In particular, when the spring stretches, the top gear, which is rigidly attached to the ratchet, can either rotate clockwise or remain stationary ($\dot{\psi} \geq 0$), whereas when the spring is compressed, the top gear can either rotate counterclockwise or remain stationary ($\dot{\psi} \leq 0$). In this way, η acts as a gating mechanism for the spring update (SI section IIA). Since update requires the ADS to be in both the “drive on” ($\dot{\theta} > 0$) and “gate open” ($\dot{\eta} > 0$) states, the ADS learning rule takes the form

$$\dot{k} = \gamma k'(\psi) \text{Relu}(\dot{\theta} - \tau_0) \Theta(\dot{\eta} - \tau_1) \quad (3)$$

where τ_0 and τ_1 are additional internal thresholds, the learning rate, γ , is a function of gear ratios (SI section IIA) and Θ denotes the Heaviside step function. The update rate, \dot{k} , is only nonzero when θ and η move in phase, which in turn requires the tail oscillations of the spring to be larger than the head oscillations (equation 2). The driving and gating mechanism of the pendulum, ratchet and gears therefore produces a directional spring update law which satisfies the ADS rules.

Our physical realization of an ADS exhibits adaptive and directional behavior (movie S1, Fig. 2F-H), and thus represents a purely mechanical self-learning unit. Oscillating an ADS at its tail leads to in-phase oscillations of the spring, η , and the pendulum, θ , (Fig. 2F, top row) which in turn rotates the elastic ring (Fig. 2G), and changes the spring stiffness. On the other hand, head oscillations produce antiphase η, θ oscillations (Fig. 2F, bottom row) which fix the spring stiffness (Fig. 2G). Provided the oscillation frequency is far from resonance for either θ or η , this phase behavior is robust to perturbations (movie S2, SI section IIB), demonstrating the viability of our ADS construction for applications. The dynamics of an ADS with changing stiffness (Fig. 2G,H) exhibits parallels with non-reciprocal systems [55–59]. In contrast with these objects, however, the breakdown of reciprocity in an ADS occurs internally, manifesting within its update rules. This form of non-reciprocity is

crucial to the learning dynamics of ADSs. Indeed, owing to its directionality, ADS learning dynamics resembles certain models [60, 61] of neuron-synapse dynamics.

SELF-LEARNING MECHANICAL CIRCUITS

Connecting multiple ADSs produces networks with rich landscapes of limit cycles and fixed points, which we term mechanical circuits. The complexity of these distinct dynamical systems illustrates how unique learning functionality emerges from fundamental units. Mechanical circuits receive external input forces and displacements which then flow through the network, causing certain ADSs to update (Fig. 3A, movie S3, SI section III). Although our networks possess geometric degrees of freedom, these flows can be understood topologically. In addition to the circuit graphs themselves, where each ADS is a directed edge (Fig. 3B), we construct flow diagrams, in which ADSs are represented by nodes (Fig. 3B). Flow diagrams are subgraphs of the circuit adjoint graph (SI section IVC) which contain all oriented paths starting at input nodes within the mechanical circuit (Fig. 3B). These diagrams thus provide a means for visualizing information propagation. Since the nodes of a flow diagram are ADSs with oscillating stiffnesses, $k_e(t)$, these diagrams are also networks of interacting oscillators. The interaction rules between neighboring ADSs follow from their directional update behavior. When an ADS e meets a second ADS e' at its tail, it promotes the update of e' . If, however, this intersection occurs at the head of e' , then e regulates the stiffness of e' by slowing down its update rate (Fig. 3B, column 3). Flow diagrams therefore encode key features of ADS update dynamics and provide guidance for choosing mechanical circuits with desired stability properties (SI section IVC). The combinatorial design space of mechanical circuits increases rapidly with size (Fig. 3C), allowing us to identify specific learning behaviors, even within relatively small graphs (Fig. 3D, movie S4). The interplay between regulation and promotion is the key mechanism by which ADS networks process mechanical information.

We demonstrate the functionality of mechanical circuits by implementing a simple, self-learning task (Fig. 4) in a very small network. Through directional information flow, small ADS networks can be used to identify ambient patterns in stochastic input forces (Fig. 4A-C), in a similar manner to neural networks [54]. In particular, by choosing combinations of ADSs which regulate each other appropriately, the network can find steady output states, in which the spring stiffnesses k reach a stable value. The final combination of stiffnesses constitutes an output for the circuit. For example, consider a many-to-one mechanical circuit of 3 ADSs, represented topologically in Fig. 4A. Here all ADSs meet at their heads, so the dynamics of each spring inhibits the up-

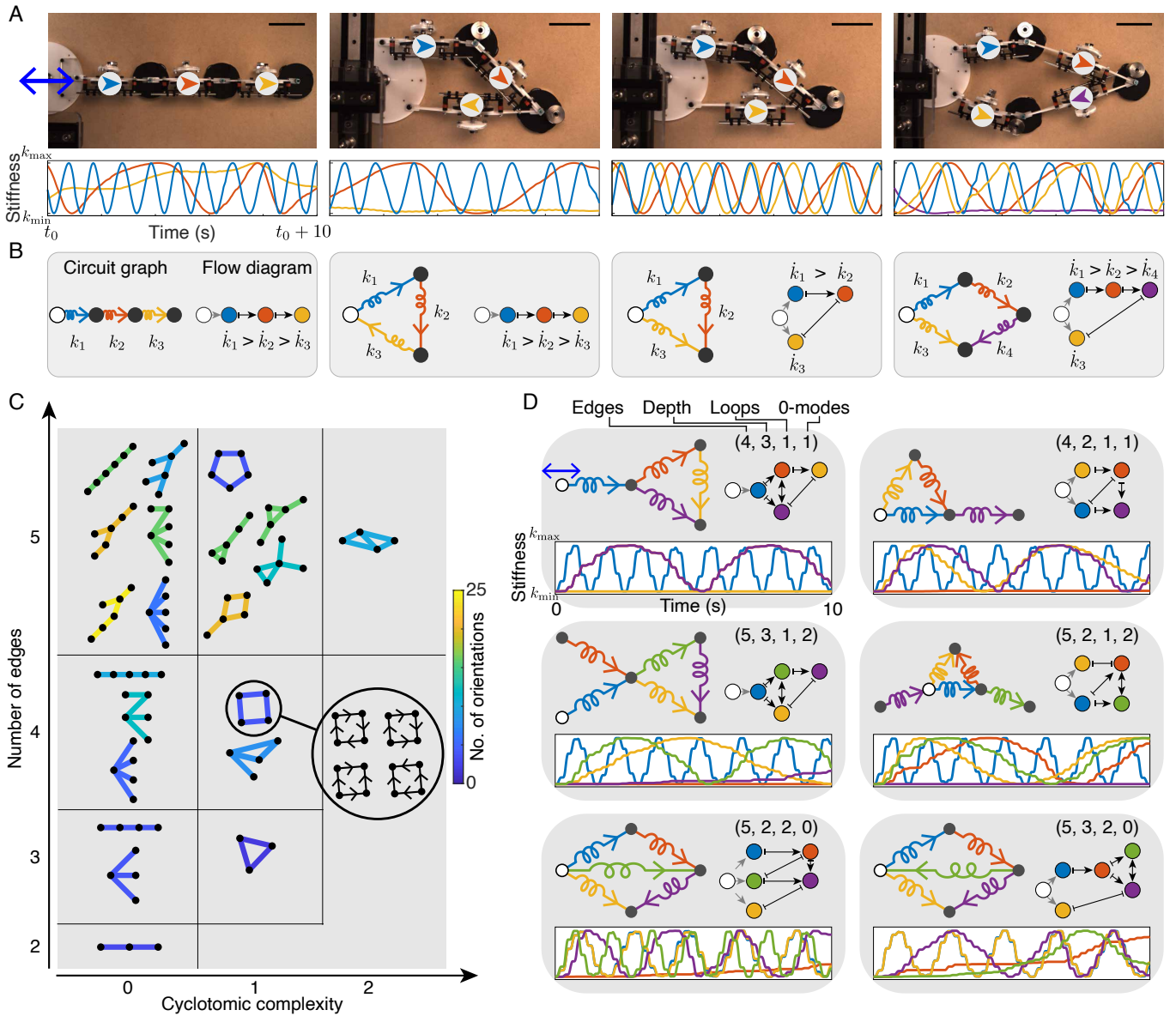


FIG. 3. Landscape of self-learning mechanical circuits. (A) Physical mechanical circuits of 3 and 4 ADSs produce a variety of distinct learning dynamics (movie S3), as revealed by their spring stiffness time series (bottom row). The input node (large white disk) oscillates at constant amplitude (≈ 1 cm) and frequency (≈ 3 Hz); the remainder of the network is purely mechanical (SI section III). Arrows point from the tail to the head of each ADS. Changing the direction of a single ADS (columns 2 and 3; yellow arrows) can dramatically alter the learning dynamics (second row). Scale bars 6 cm. (B) Topological representations of mechanical circuits. The circuit graphs show the ADS orientations, with the input forcing node colored white. Flow diagrams (SI section IVC) represent ADSs as nodes (colored circles) receiving forces from input nodes (white nodes, short grey arrows). All the oriented ADS paths emanating from the input node are displayed. Arrowhead style denotes promotory (sharp arrowhead) or inhibitory (flat arrowhead) interactions: in column 1, the blue ADS meets the red ADS at its tail (promotory), but the red ADS meets the blue ADS at its head (inhibitory). When two paths cross (columns 3 and 4), additional edges are drawn between ADSs at the crossing point (e.g. column 3, yellow ADS and red ADS). Edges further downstream of the input node update more slowly (A-C, second row), and thus store information about the long timescale variations of the input signal. (C) The number of topologically distinct oriented graphs increases exponentially, demonstrating the breadth of learning functionality accessible even with small circuits. Loops, which mimic recurrent connections in certain neural network architectures, are measured by cyclotomic complexity. Each depicted graph has multiple non-isomorphic orientations (inset). (D) Learning outcomes can be selected for by analyzing different networks (grey boxes) chosen from (C). Each box displays a mechanical circuit (top left) with an input node (white circle), a flow diagram (colored circles), and the resulting learning dynamics (second row). Flow diagrams encode certain features of the learning dynamics (SI section IVC). Along with edges and loops, the depth of the flow diagram and zero modes of the elastic network are key determinants of mechanical circuit behavior (movie S4). See SI section IVE for simulation parameters.

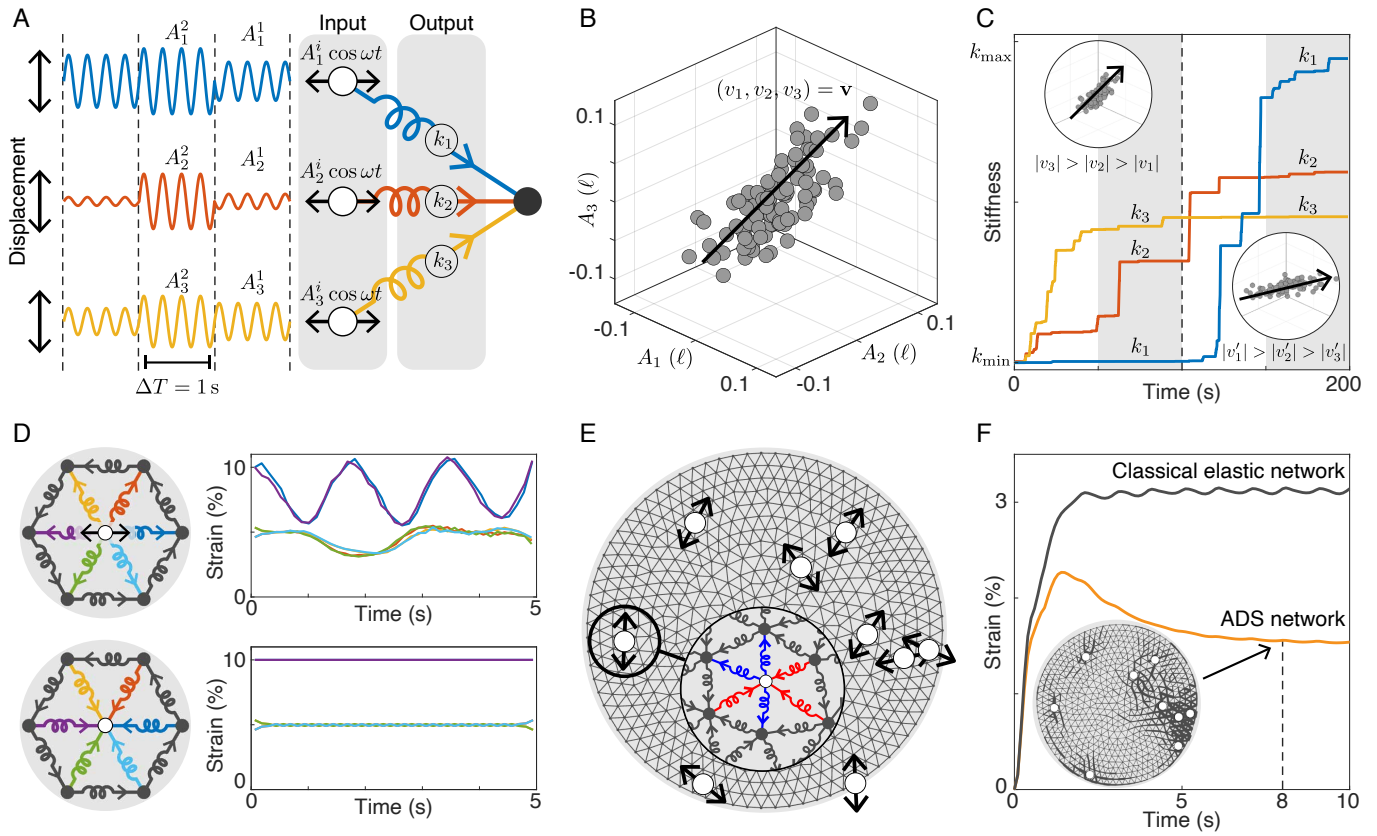


FIG. 4. Functional self-learning in mechanical circuits (A-C) An ADS network exposed to time-varying environmental perturbations uncovers the pattern hidden within its input. (A) Topological representation of a particular mechanical circuit with inhibitory head-connections. Every ADS regulates every other ADS, thus processing the oscillatory inputs received at each tail (white nodes). The network receives single-frequency oscillations with a sequence of amplitudes, $\mathbf{A}^i = (A_1^i, A_2^i, A_3^i)$, representing environmental interactions. All oscillations have equal frequency and phase modulo π ; negative amplitudes correspond to oscillations phase-shifted by π . (B) The amplitudes, \mathbf{A}^i are assumed to be drawn from a structured distribution, with principal direction \mathbf{v} , representing an underlying pattern in the environment. (C) The pattern, \mathbf{v} , underlying the oscillation amplitudes, \mathbf{A}^i received by the network, is recovered by the spring stiffnesses (k_1, k_2, k_3) (shaded region) with high probability (SI section IVD). The stiffnesses evolve so that their ordering matches the ordering of the components ($|v_1|, |v_2|, |v_3|$). When the pattern changes, $\mathbf{v} \rightarrow \mathbf{v}'$ (dashed line at $t = 100s$), the network is able to adapt and learn the new pattern for a class of vectors \mathbf{v}' (SI section IVD). (D) Directional adaptivity controls how strain is transmitted through an ADS network. ADSs adjacent to oscillating nodes with large out-degree (top row, white node) stiffen and redistribute strain, thus reducing their average strain over oscillation cycles (colored curves). ADSs around forced nodes with large in-degree (bottom row) experience higher average strain. In the latter case, the strain is effectively caged (bottom row, movie S5). In both cases, the ADSs are initially in their softest state, and the input oscillation is horizontal (top row, black arrow). (E,F) Strain redistribution within a large ADS network, initially in its softest state. (E) Caging is unlikely in large ADS networks with randomly chosen forcing nodes (white) and random ADS orientations. Forcing nodes are typically adjacent to both inward pointing ADSs (red) and outward ADSs (blue), which enable strain distribution. (F) The ADS network experiences a lower average strain (orange curve) than a non-adaptive elastic network (black curve) undergoing the same input oscillations (movie S5). Stiffening ADSs redistribute strain (inset). See SI section IVE for simulation parameters.

date rate of every other spring (Fig. 3B). In such a mechanical circuit, the tail ends of the ADSs function as input nodes, through which the network interacts with its environment. A simple model of environmental inputs consists of horizontal displacement waves (Fig. 4A) with amplitudes which are time varying and random, but possess underlying correlations, represented by a vector (v_1, v_2, v_3) (Fig. 4B). To perform computations on these horizontal inputs, the geometric shape of the mechan-

ical circuit (Fig. 4A) must be chosen to minimize the angle difference between the ADSs and the input oscillations (SI section IVD). The stiffness pattern within a simulated network then evolves to reflect the statistical properties of these inputs (Fig. 4C). In particular, the ordering of the ADS stiffnesses k_1, k_2, k_3 (Fig. 4B) updates to match the ordering of the absolute correlation vector components, $|v_1|, |v_2|, |v_3|$, (Fig. 4C) with probability greater than 80% (SI section IVD, Fig. S29). To learn

a new pattern the network must first forget its previous state. For significant changes in the input pattern (SI section IVD), the network can adapt (Fig. 4C), identifying the new pattern with probability greater than 50%. (SI section IVD). This computational task represents an idealized scenario, in which the environmental inputs consist of waves with equal frequency and phase (Fig. 4A). Despite these simplifications, this example demonstrates the ability of mechanical circuits to compute features of a changing environment.

Complementing its unsupervised learning behavior, ADS networks also represent a platform for creating materials with designer properties. For example, even within structured lattice-like networks, ADS directionality gives rise to an exponentially large design space. In general, nodes within such networks are characterized by the number of adjacent ADSs which point inwards or outwards (Fig. 4D). Oscillations of nodes with large out-degree cause adjacent ADSs to update, ultimately leading to the redistribution of strain throughout the network (Fig. 4D, top). On the other hand, friction and directionality combine to cage the motion of a node with zero out-degree (Fig. 4D, bottom; movie S5), acting as a form of mechanical camouflage. In a large network with randomly oriented ADSs, forcing nodes are very likely to have non-zero out-degree (Fig. 4E,F). When initialized with soft springs (SI section IVD), such ADS networks exhibit an adaptive damping behavior, in which spring stiffening distributes loads throughout the network and reduces local strains (movie S5). In particular, ADS networks distribute and reduce overall strains more effectively than a classical, non-adaptive, elastic network (Fig. 4F).

DISCUSSION

By virtue of their purely mechanical construction, our self-learning mechanical circuits represent an alternative to the embedded electronics paradigm [62], merging sensing, computation and actuation for the design of monolithic materials with embodied intelligence [63, 64]. Mechanical circuits provide advantages in environments incompatible with electronic operation, from high-radiation and extreme-temperature conditions to settings involving integration with living matter [63]. Furthermore, our ADS implementations are battery-free, and draw power from their input signal. Although the balance between external environmental energy input and internal dissipation could limit a mechanical circuit, this construction presents advantages when power is scarce. Additionally, due to the absence of an on-board power source, the ADS mechanism relies only on the physics of elasticity, a domain with few manufacturing constraints. In particular, elasticity does not require heterogeneous materials, so mechanical circuits can be built from a va-

riety of raw materials. Scaling of such systems could therefore be achieved using abundant monolithic materials and existing micro-fabrication methods.

Using adaptive directed springs with embedded memory, we construct mechanical circuits which can learn information about their environment by interfacing with it mechanically. The combinatorial landscape of mechanical circuits presented here provides a design space for constructing networks that solve classes of learning tasks. A breadth of functions can be implemented with these motifs, analogous to previous demonstrations in the field of genetic circuits [65]. Furthermore, our approach can be augmented with a variety of mechano-dynamical systems [66] which could be harnessed as additional sources of nonlinearities for self-learning behavior. Although our physical realization of an ADS involves several components, the individual mechanisms of a spring, pendulum and ratchet, are generic. Their simplicity suggests that ADS functionality could be harnessed in different domains and length scales [67–70], such as fluidic [67, 71] and electromechanical [62] systems. A particularly interesting question is whether ADS-type dynamics plays a role in adaptivity in biological contexts [2, 20]. The framework developed here could thus improve our understanding of self-learning in living matter. More generally, our results provide a toolbox for the construction of self-learning mechanical circuits which continually adapt themselves, presenting a paradigm for self-learning materials as machines.

ACKNOWLEDGEMENTS

V.P.P., I.H. and M.P. conceptualized this work. V.P.P. performed simulations and analytic calculations. I.H. designed and performed experiments. All authors contributed to interpreting data, and writing the manuscript. This work was financially supported by a Stanford Science Fellowship (V.P.P.), a Tau Beta Pi Fellowship (I.H.), a HHMI Faculty Fellowship (M.P.), BioHub Investigator Fellowship (M.P.), Schmidt Innovation Fellowship (M.P.), Moore Foundation Research Grant (M.P.) and NSF CCC (DBI1548297 (M.P.)).

-
- [1] P. Fleig, M. Kramar, M. Wilczek, and K. Alim, Emergence of behaviour in a self-organized living matter network, *elife* **11**, e62863 (2022).
 - [2] P. J. Foster, S. Fürthauer, M. J. Shelley, and D. J. Needleman, From cytoskeletal assemblies to living materials, *Curr. Opin. Cell Biol.* **56**, 109 (2019).
 - [3] C. D. Nadell, K. Drescher, N. S. Wingreen, and B. L. Bassler, Extracellular matrix structure governs invasion resistance in bacterial biofilms, *ISME J.* **9**, 1700 (2015).

- [4] C. K. Lee, J. De Anda, A. E. Baker, R. R. Bennett, Y. Luo, E. Y. Lee, J. A. Keefe, J. S. Helali, J. Ma, K. Zhao, *et al.*, Multigenerational memory and adaptive adhesion in early bacterial biofilm communities, *Proc. Natl. Acad. Sci.* **115**, 4471 (2018).
- [5] A. H. Gandomi and A. H. Alavi, Krill herd: a new bio-inspired optimization algorithm, *Comm. Nonlinear Sci. Numer.* **17**, 4831 (2012).
- [6] M. Stern and A. Murugan, Learning without neurons in physical systems, *Annu. Rev. Condens. Matter Phys.* **14**, 417 (2023).
- [7] G. Tanaka, T. Yamane, J. B. Héroux, R. Nakane, N. Kanazawa, S. Takeda, H. Numata, D. Nakano, and A. Hirose, Recent advances in physical reservoir computing: A review, *Neural Netw.* **115**, 100 (2019).
- [8] H. Hauser, A. J. Ijspeert, R. M. Füchslin, R. Pfeifer, and W. Maass, Towards a theoretical foundation for morphological computation with compliant bodies, *Biol. Cybern.* **105**, 355 (2011).
- [9] X. Xia, C. M. Spadaccini, and J. R. Greer, Responsive materials architected in space and time, *Nat. Rev. Mater.* **7**, 683 (2022).
- [10] A. Vergis, K. Steiglitz, and B. Dickinson, The complexity of analog computation, *Math. Comput. Simul.* **28**, 91 (1986).
- [11] B. VanSaders and V. Vitelli, Informational active matter, arXiv preprint arXiv:2302.07402 (2023).
- [12] D. E. Rumelhart, G. E. Hinton, and R. J. Williams, Learning representations by back-propagating errors, *Nature* **323**, 533 (1986).
- [13] H. T. Siegelmann and S. Fishman, Analog computation with dynamical systems, *Physica D* **120**, 214 (1998).
- [14] H. T. Siegelmann, Computation beyond the turing limit, *Science* **268**, 545 (1995).
- [15] B. Scellier and Y. Bengio, Equilibrium propagation: Bridging the gap between energy-based models and back-propagation, *Front. Comput. Neurosci.* **11**, 24 (2017).
- [16] S. Dillavou, M. Stern, A. J. Liu, and D. J. Durian, Demonstration of decentralized physics-driven learning, *Phys. Rev. Appl.* **18**, 014040 (2022).
- [17] S. Aaronson, Guest column: Np-complete problems and physical reality, *ACM Sigact News* **36**, 30 (2005).
- [18] M. Kramar and K. Alim, Encoding memory in tube diameter hierarchy of living flow network, *Proc. Natl. Acad. Sci.* **118**, e2007815118 (2021).
- [19] J. Devany, D. M. Sussman, T. Yamamoto, M. L. Manning, and M. L. Gardel, Cell cycle-dependent active stress drives epithelia remodeling, *Proc. Natl. Acad. Sci.* **118**, e1917853118 (2021).
- [20] F. Rashid, W. Liu, Q. Wang, B. Ji, J. Irudayaraj, and N. Wang, Mechanomemory in protein diffusivity of chromatin and nucleoplasm after force cessation, *Proc. Natl. Acad. Sci.* **120**, e2221432120 (2023).
- [21] M. Pittman, E. Iu, K. Li, J. Chen, S. Potnikov, and Y. Chen, Membrane ruffling is a mechanosensor of extracellular fluid viscosity, *Biophys. J.* **121**, 267a (2022).
- [22] H. Kim, D. J. Skinner, D. S. Glass, A. E. Hamby, B. A. Stuart, J. Dunkel, and I. H. Riedel-Kruse, 4-bit adhesion logic enables universal multicellular interface patterning, *Nature* **608**, 324 (2022).
- [23] C. Squarci, P. Bianco, M. Reconditi, I. Pertici, M. Caremani, T. Narayanan, Á. I. Horváth, A. Málnási-Csizmadia, M. Linari, V. Lombardi, *et al.*, Titin activates myosin filaments in skeletal muscle by switching from an extensible spring to a mechanical rectifier, *Proc. Natl. Acad. Sci.* **120**, e2219346120 (2023).
- [24] P. J. Foster, W. Yan, S. Fürthauer, M. J. Shelley, and D. J. Needleman, Connecting macroscopic dynamics with microscopic properties in active microtubule network contraction, *New J. Phys.* **19**, 125011 (2017).
- [25] A. Mahuzier, A. Shihavuddin, C. Fournier, P. Lansade, M. Faucourt, N. Menezes, A. Meunier, M. Garfa-Traoré, M.-F. Carlier, R. Voituriez, *et al.*, Ependymal cilia beating induces an actin network to protect centrioles against shear stress, *Nat. Commun.* **9**, 2279 (2018).
- [26] B. T. Goult, N. H. Brown, and M. A. Schwartz, Talin in mechanotransduction and mechanomemory at a glance, *J. Cell. Sci.* **134**, jcs258749 (2021).
- [27] S. Phonekeo, T. Dave, M. Kern, S. V. Franklin, and D. L. Hu, Ant aggregations self-heal to compensate for the ringmann effect, *Soft Matter* **12**, 4214 (2016).
- [28] A. Chakraborty and A. K. Kar, Swarm intelligence: A review of algorithms, *Nat.-Inspired Comput. Optim.* , 475 (2017).
- [29] T. Chen, M. Pauly, and P. M. Reis, A reprogrammable mechanical metamaterial with stable memory, *Nature* **589**, 386 (2021).
- [30] M. Stern, M. B. Pinson, and A. Murugan, Continual learning of multiple memories in mechanical networks, *Phys. Rev. X* **10**, 031044 (2020).
- [31] D. Fiocco, G. Foffi, and S. Sastry, Encoding of memory in sheared amorphous solids, *Phys. Rev. Lett.* **112**, 025702 (2014).
- [32] S. Mukherji, N. Kandula, A. Sood, and R. Ganapathy, Strength of mechanical memories is maximal at the yield point of a soft glass, *Phys. Rev. Lett.* **122**, 158001 (2019).
- [33] N. C. Keim, J. D. Paulsen, Z. Zeravcic, S. Sastry, and S. R. Nagel, Memory formation in matter, *Rev. Mod. Phys.* **91**, 035002 (2019).
- [34] V. F. Hagh, S. R. Nagel, A. J. Liu, M. L. Manning, and E. I. Corwin, Transient learning degrees of freedom for introducing function in materials, *Proc. Natl. Acad. Sci.* **119**, e2117622119 (2022).
- [35] D. Oktay, M. Mirramezani, E. Medina, and R. P. Adams, Neuromechanical autoencoders: Learning to couple elastic and neural network nonlinearity, arXiv preprint arXiv:2302.00032 (2023).
- [36] J. L. Silverberg, A. A. Evans, L. McLeod, R. C. Hayward, T. Hull, C. D. Santangelo, and I. Cohen, Using origami design principles to fold reprogrammable mechanical metamaterials, *Science* **345**, 647 (2014).
- [37] P. Bhovad and S. Li, Physical reservoir computing with origami and its application to robotic crawling, *Sci. Rep.* **11**, 13002 (2021).
- [38] R. H. Lee, E. A. Mulder, and J. B. Hopkins, Mechanical neural networks: Architected materials that learn behaviors, *Sci. Robot.* **7**, eabq7278 (2022).
- [39] D. R. Reid, N. Pashine, J. M. Wozniak, H. M. Jaeger, A. J. Liu, S. R. Nagel, and J. J. de Pablo, Auxetic metamaterials from disordered networks, *Proc. Natl. Acad. Sci.* **115**, E1384 (2018).
- [40] N. Pashine, D. Hexner, A. J. Liu, and S. R. Nagel, Directed aging, memory, and nature's greed, *Sci. Adv.* **5**, eaax4215 (2019).
- [41] D. Hexner, A. J. Liu, and S. R. Nagel, Periodic training of creeping solids, *Proc. Natl. Acad. Sci.* **117**, 31690 (2020).

- [42] M. Stern, C. Arinze, L. Perez, S. E. Palmer, and A. Murugan, Supervised learning through physical changes in a mechanical system, *Proc. Natl. Acad. Sci.* **117**, 14843 (2020).
- [43] L. G. Wright, T. Onodera, M. M. Stein, T. Wang, D. T. Schachter, Z. Hu, and P. L. McMahon, Deep physical neural networks trained with backpropagation, *Nature* **601**, 549 (2022).
- [44] K. Bhattacharyya, D. Zwicker, and K. Alim, Memory formation in adaptive networks, *Phys. Rev. Lett.* **129**, 028101 (2022).
- [45] H. Ronellenfitsch and E. Katifori, Global optimization, local adaptation, and the role of growth in distribution networks, *Phys. Rev. Lett.* **117**, 138301 (2016).
- [46] J. Gräwer, C. D. Modes, M. O. Magnasco, and E. Katifori, Structural self-assembly and avalanchelike dynamics in locally adaptive networks, *Phys. Rev. E* **92**, 012801 (2015).
- [47] J. Wycoff, S. Dillavou, M. Stern, A. Liu, and D. Durian, Desynchronous learning in a physics-driven learning network, *J. Chem. Phys.* **156**, 144903 (2022).
- [48] F. Zangeneh-Nejad, D. L. Sounas, A. Alù, and R. Fleury, Analogue computing with metamaterials, *Nat. Rev. Mater.* **6**, 207 (2021).
- [49] J. F. Yang, A. T. Liu, T. A. Berrueta, G. Zhang, A. M. Brooks, V. B. Koman, S. Yang, X. Gong, T. D. Murphey, and M. S. Strano, Memristor circuits for colloidal robotics: Temporal access to memory, sensing, and actuation, *Adv. Intell. Syst.* **4**, 2100205 (2022).
- [50] A. Prabhakar and T. Murphey, Mechanical intelligence for learning embodied sensor-object relationships, *Nat. Commun.* **13**, 4108 (2022).
- [51] G. Hinton, The forward-forward algorithm: Some preliminary investigations, arXiv preprint arXiv:2212.13345 (2022).
- [52] N. Rodgers, P. Tiño, and S. Johnson, Network hierarchy and pattern recovery in directed sparse hopfield networks, *Phys. Rev. E* **105**, 064304 (2022).
- [53] T. Umedachi and A. Ishiguro, A development of a fully self-contained real-time tunable spring, in *2006 IEEE/RSJ International Conference on Intelligent Robots and Systems* (IEEE, 2006) pp. 1662–1667.
- [54] E. Oja, Simplified neuron model as a principal component analyzer, *J. Math. Biol.* **15**, 267 (1982).
- [55] C. Coullais, D. Sounas, and A. Alu, Static non-reciprocity in mechanical metamaterials, *Nature* **542**, 461 (2017).
- [56] D. L. Sounas and A. Alù, Non-reciprocal photonics based on time modulation, *Nat. Photonics* **11**, 774 (2017).
- [57] M. Fruchart, R. Hanai, P. B. Littlewood, and V. Vitelli, Non-reciprocal phase transitions, *Nature* **592**, 363 (2021).
- [58] M. Brandenbourger, C. Scheibner, J. Veenstra, V. Vitelli, and C. Coullais, Limit cycles turn active matter into robots, arXiv preprint arXiv:2108.08837 (2021).
- [59] M. Brandenbourger, X. Locsin, E. Lerner, and C. Coullais, Non-reciprocal robotic metamaterials, *Nat. Commun.* **10**, 4608 (2019).
- [60] N. Caporale and Y. Dan, Spike timing-dependent plasticity: a hebbian learning rule, *Annu. Rev. Neurosci.* **31**, 25 (2008).
- [61] R. Legenstein, D. Pecevski, and W. Maass, A learning theory for reward-modulated spike-timing-dependent plasticity with application to biofeedback, *PLOS Comput. Biol.* **4**, e1000180 (2008).
- [62] C. El Helou, B. Grossmann, C. E. Tabor, P. R. Buskohl, and R. L. Harne, Mechanical integrated circuit materials, *Nature* **608**, 699 (2022).
- [63] W. Hu, G. Z. Lum, M. Mastrangeli, and M. Sitti, Small-scale soft-bodied robot with multimodal locomotion, *Nature* **554**, 81 (2018).
- [64] D. Morton, A. Xu, A. Matute, and R. F. Shepherd, Autonomous material composite morphing wing, *J. Compos. Mater.* , 00219983231151397 (2023).
- [65] U. Alon, *An introduction to systems biology: design principles of biological circuits* (CRC press, 2019).
- [66] M. Berry, D. Limberg, M. Lee-Trimble, R. Hayward, and C. Santangelo, Controlling the configuration space topology of mechanical structures, *Phys. Rev. E* **106**, 055002 (2022).
- [67] P. Robin, T. Emmerich, A. Ismail, A. Niguès, Y. You, G.-H. Nam, A. Keerthi, A. Siria, A. Geim, B. Radha, *et al.*, Long-term memory and synapse-like dynamics in two-dimensional nanofluidic channels, *Science* **379**, 161 (2023).
- [68] T. W. Hughes, I. A. Williamson, M. Minkov, and S. Fan, Wave physics as an analog recurrent neural network, *Sci. Adv.* **5**, eaay6946 (2019).
- [69] D. J. Preston, P. Rothmund, H. J. Jiang, M. P. Nemitz, J. Rawson, Z. Suo, and G. M. Whitesides, Digital logic for soft devices, *Proc. Natl. Acad. Sci.* **116**, 7750 (2019).
- [70] S. W. Schaffter, K.-L. Chen, J. O’Brien, M. Noble, A. Murugan, and R. Schulman, Standardized excitable elements for scalable engineering of far-from-equilibrium chemical networks, *Nat. Chem.* **14**, 1224 (2022).
- [71] F. G. Woodhouse and J. Dunkel, Active matter logic for autonomous microfluidics, *Nat. Commun.* **8**, 15169 (2017).

Supplementary information: Self-learning mechanical circuits

Vishal P. Patil^{1,†}, Ian Ho^{1,†}, Manu Prakash^{1,2,3,*}

¹*Department of Bioengineering, Stanford University, Stanford CA 94305 USA*

²*Department of Biology, Stanford University, Stanford CA 94305 USA*

³*Department of Oceans, Stanford University, Stanford CA 94305 USA*

[†] *Equal contributions*

** To whom correspondence should be addressed: manup@stanford.edu*

(Dated: April 19, 2023)

CONTENTS

I. Theoretical formulation of an adaptive directed spring (ADS)	2
A. Axiomatic construction of an ADS	2
1. Axioms	2
2. Directional update rules for an ideal ADS	5
3. Directional update rules for a physical ADS	6
4. Symmetries of an ADS	7
5. Extensions of the ADS concept	8
B. Mechanical construction of an ADS	10
1. Surface friction	10
2. Adaptive spring	11
3. Pendulum on a spring	12
4. Elastic ring on a four-bar linkage	14
5. Coupling spring stiffness to mechanics	15
II. Physical realization	17
A. ADS design and manufacturing	17
1. Design	17
2. Coupling gear gating mechanism	18
3. Fabrication and assembly	20
B. Origin of directionality in adaptive springs	22
1. Directionality in update requires the existence of both η and θ oscillators	23
2. Coupling gear produces $\text{sgn}(\dot{\eta})$ dependent torque on the elastic ring	23
3. ADS orientation depends on gear mechanism pattern	24
4. Higher order effects of four-bar linkage at $k = 0$	24
5. Phase coupling is robust to perturbations	25
6. Effect of frequency on the directionality of an ADS	26
III. Experimental Methods	27
A. Setup	28
1. Top view tracking	28
2. Side view tracking	28
3. Validation of tracking code	29
4. Quality control of ADS	29
B. Experimental parameters	30
1. Measuring $k(\psi)$	30
2. Damping on nodes	30
3. Natural frequency and moment of inertia of pendulum	31
4. Friction coefficient between node and substrate	32
5. Learning rate estimate	33
6. Parameters for each experiment	33
IV. Mechanical circuits	34

A. Dynamics of a single ADS	34
B. Dynamics of ADS networks	35
1. Classical elastic networks	37
2. ADS networks	37
3. Small viscous damping	38
4. Fixed points	38
C. Small mechanical circuits	38
1. Flow diagrams	39
2. Circuit dynamics	39
D. Applications	42
1. Pattern finding	42
2. Adaptive damping	45
E. Simulation parameters	46
V. Supplementary movies	47
References	47

I. THEORETICAL FORMULATION OF AN ADAPTIVE DIRECTED SPRING (ADS)

In this section, we introduce and motivate the axioms for an adaptive directed spring (ADS). We then show how these axioms naturally point towards mechanical gadgets that can be used to construct an ADS.

A. Axiomatic construction of an ADS

An adaptive directed spring (ADS) must come with a notion of adaptivity, directionality, and an activation non-linearity. Intuitively, we want an ADS to exhibit the following behavior

1. Activation non-linearity: The spring only transmits force when the spring stiffness, and oscillation amplitudes are large enough.
2. Adaptivity: The spring can change stiffness.
3. Directionality: The spring has a head and a tail; the spring stiffness changes if and only if the tail motion is bigger than the head motion.

Adaptivity is needed in order for the springs to respond to their environment; the activation non-linearity and directionality are mechanisms which produce fixed points, allowing an ADS network to learn interesting features of its environment. Here we describe these properties precisely, and thus define the axioms for an ADS. These axioms indicate how an ADS may be constructed from a classical spring.

1. Axioms

To begin with, consider a classical spring joining two nodes with mass m . The spring is determined by the motion of each node in time, $\mathbf{x}_1(t)$, $\mathbf{x}_2(t)$, its natural length ℓ and stiffness k . Together, $\mathbf{x}_1(t)$, $\mathbf{x}_2(t)$, ℓ , k , m completely govern the spring-mass system. For simplicity, we choose coordinates so that the spring lies parallel to the x -axis (Fig. S1A). We assume that the spring dynamics is in a regime where we can decompose the node displacements in terms of slowly and rapidly varying terms

$$\mathbf{x}_i(t) = \mathbf{x}_i^0 + \mathbf{u}_i(t) \quad (1)$$

where $\mathbf{x}_i^0 = \langle \mathbf{x}_i \rangle$ is the slowly varying mean position of node i , and \mathbf{u}_i is the faster oscillatory component of motion (Fig. S1A). We further assume that $|\mathbf{x}_2^0 - \mathbf{x}_1^0| = \ell$, so that the (leading order) spring extension in our chosen coordinates (Fig. S1A) is given by

$$\eta(t) = (\mathbf{u}_2 - \mathbf{u}_1) \cdot \mathbf{e}_x$$

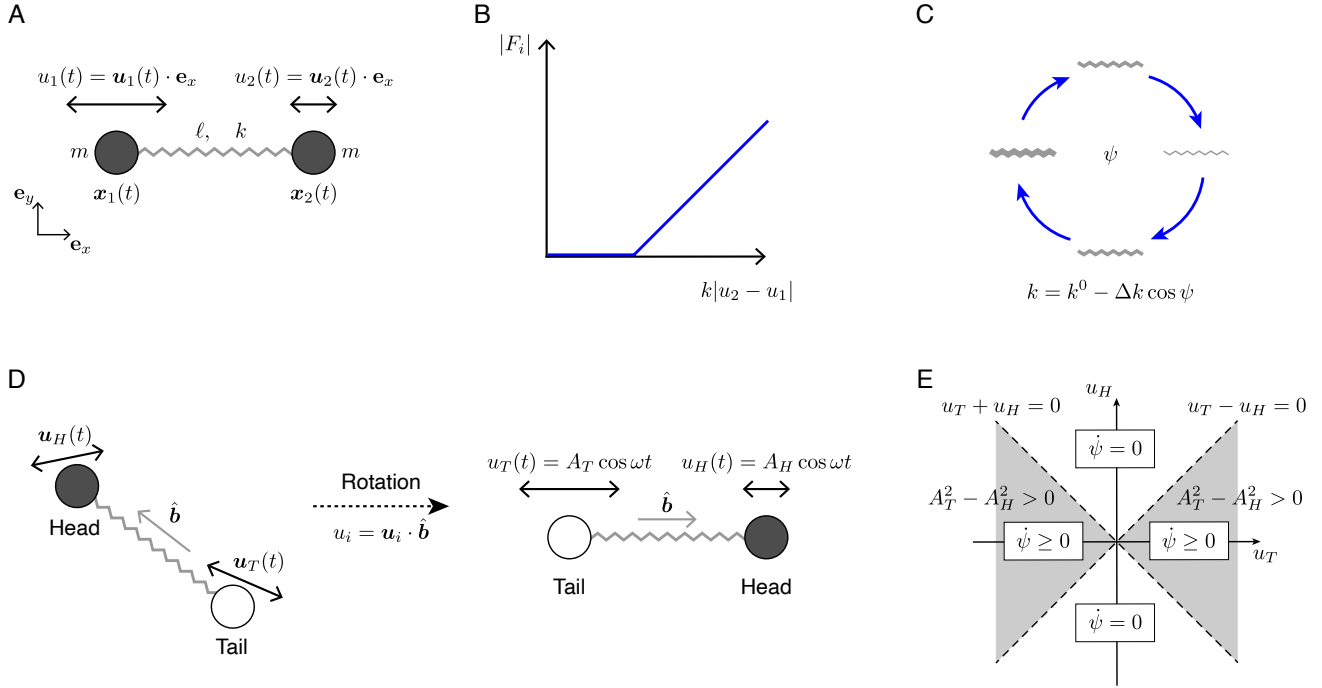


FIG. S1. **Formulation of an adaptive directed spring (ADS)** (A) A classical spring joining two nodes of mass m is characterized by its natural length ℓ , stiffness k and the displacements of each node. We assume there is a separation of timescales between fast node oscillations, $\mathbf{u}_i(t)$, and slower overall motion of the spring (equation 1). We choose coordinates so that the spring is horizontal and focus on the node oscillations in the direction of the spring, $u_i = \mathbf{u}_i \cdot \mathbf{e}_x$. To begin with, we assume that a single oscillation frequency, ω , dominates, and that the phase difference between u_1 and u_2 is close to 0 or π . This allows us to write $u_i = A_i \cos \omega t$ with $A_i \in \mathbb{R}$. (B) The response on node i due to the spring, F_i , is not equal to the product of extension $|u_2 - u_1|$ and spring constant k . Only when $k|u_2 - u_1|$ crosses a threshold value (which can in general vary from node to node), does the force on node i become non-zero. (C) For continual adaptivity, the stiffness, k of an ADS must increase and decrease. We can therefore write k in terms of a phase angle, $k = k^0 - \Delta k \cos \psi$. In general, we allow the k - ψ relation to have additional offsets (equation 3a). (D) The directionality of an ADS means that the spring must have a tail (white) and a head (grey). We choose coordinates so that the tail-to-head unit vector, $\hat{\mathbf{b}}$, coincides with the positive x -direction. The head and tail oscillations, $u_H(t)$, $u_T(t)$ in the direction of the spring are given by $u_i = \mathbf{u}_i \cdot \hat{\mathbf{b}}$. (E) The directionality axioms for an ideal ADS (equations 3b and 3c) require the spring stiffness to update (i.e. $\dot{\psi} > 0$) if and only if $|A_T| > |A_H|$. In the case where $u_i = A_i \cos \omega t$ (as in panel A), this condition can be straightforwardly expressed in terms of u_T and u_H (shaded region): the spring updates if and only if $u_T \pm u_H$ have the same sign. Since equation (3b) requires the spring to update over an oscillation cycle, $\dot{\psi}$ is allowed to be 0 at locations within the shaded region provided $\langle \dot{\psi} \rangle > 0$ over an oscillation.

Our construction of an ADS will focus on the node oscillations in the spring direction (Fig. S1A)

$$u_i = \mathbf{u}_i \cdot \mathbf{e}_x$$

The spring extension can therefore be written

$$\eta(t) = u_2(t) - u_1(t)$$

Activation non-linearity

We require that the spring has a nonlinear response. This helps ensure that the dynamics of the spring are rich enough to encode interesting functions. Mimicking neural networks, we assume that F_i , the response force on node i , has an activation non-linearity, and is not simply proportional to the spring extension, $|u_2 - u_1|$. Concretely, we set

$$|F_i| = \text{Relu}(k|u_2 - u_1| - \nu_i) \quad \text{if } \dot{u}_i = 0$$

where k is the spring constant, and ν_i is a threshold which can vary from node to node (Fig. S1B). This means that the nodes do not respond to small changes in the spring length. The thresholding is therefore a mechanism for enhancing stability.

Adaptivity

To achieve adaptivity, k must be allowed to vary in time. In particular, for continual adaptivity, we need k to loop back and forth. We can therefore write $k = k(\alpha_0\psi)$, where ψ is an angular variable, so that k is a periodic function with periodicity $2\pi/\alpha_0$. Taking a lowest Fourier mode approximation, we can further write

$$k(t) = k^0 - \Delta k \cos(\alpha_0\psi(t) + \alpha_1)$$

where the phase angle, $\psi(t)$ is time dependent, $k^0 \pm \Delta k$ are the maximum and minimum values of $k(t)$, and α_0, α_1 are shift parameters which we have included for convenience. In order for the adaptivity to affect the dynamics, we need $\langle \dot{\psi} \rangle \neq 0$ over short timescales. We can achieve this by setting $\dot{\psi} \geq 0$, so that ψ can only increase (Fig. S1C).

Directionality

Finally, we want the spring to have a directional adaptivity, which requires specifying a tail end and head end for the spring. This allows us to define a unit vector, $\hat{\mathbf{b}}$ that points from tail to head. The tail oscillations are given by \mathbf{u}_T and \mathbf{u}_H respectively. We can rotate the spring so that the tail is to the left of the head (Fig. S1D). For directional adaptivity, we want k to update when the spring is oscillated more on the tail end than the head end. More precisely, we define $u_T(t)$ and $u_H(t)$ to be the tail and head oscillations in the direction of the spring (Fig. S1D),

$$u_T = \mathbf{u}_T \cdot \hat{\mathbf{b}}, \quad u_H = \mathbf{u}_H \cdot \hat{\mathbf{b}} \quad (2)$$

We require k to update if $\langle |u_T| \rangle > \langle |u_H| \rangle$, but to remain unchanged if $\langle |u_H| \rangle \geq \langle |u_T| \rangle$, where the time averages are taken over the fast oscillation timescale (equation 1). Crucially, this means that spring responds differently to inputs on the tail and head.

Together, the above formulations of adaptivity and directionality give us the axioms of an ADS, with head and tail oscillations parallel to the spring given by $u_H(t)$ and $u_T(t)$ respectively (Fig. S1D).

$$k(t) = k^0 - \Delta k \cos(\alpha_0\psi(t) + \alpha_1), \quad \dot{\psi} \geq 0 \quad (\text{Continual adaptivity}) \quad (3a)$$

$$\langle \dot{\psi} \rangle > 0 \quad \text{if } \langle |u_T| \rangle > \langle |u_H| \rangle + \delta \quad (\text{Directional adaptivity}) \quad (3b)$$

$$\dot{\psi} = 0 \quad \text{if } \langle |u_T| \rangle \leq \langle |u_H| \rangle \quad (\text{Self-regulation}) \quad (3c)$$

$$|F_i| = \text{Relu}(k|u_H - u_T| - \nu_i), \quad \text{if } \dot{u}_i = 0 \quad (\text{Activation}) \quad (3d)$$

Axiom (a) states that the spring stiffness k loops back and forth. k^0 and Δk determine the maximum and minimum spring stiffness and satisfy $k^0 > \Delta k > 0$. The parameters α_0, α_1 are shift parameters, with α_0 defined to be positive. Axiom (b) states that the spring stiffness updates if the tail oscillates with a greater amplitude than the head, and axiom (c) states that the spring remains unchanged if the head oscillates with a greater amplitude than the tail (Fig. S1E). In each case, the time averages are taken over the fast oscillation timescale (equation 1). The threshold $\delta > 0$ in axiom (b) is useful when discussing the tolerances of a physical ADS; an ideal ADS has $\delta = 0$. Finally, axiom (d) states that the force on the i 'th node, F_i , is only non-zero if the product of spring stiffness and extension $k|u_H - u_T|$ crosses a threshold, ν_i .

A key feature of these axioms is that the directional adaptivity comes with a feedback mechanism: the spring updates when $\langle |u_T| \rangle > \langle |u_H| \rangle$ but this update can be switched off if $\langle |u_H| \rangle$ is increased. We note that this is different from a simpler form of directionality, in which ψ is only a function of u_T . For example, ψ dynamics of the form

$$\dot{\psi} = \text{Relu}(u_T)$$

fails to satisfy axiom (c).

2. Directional update rules for an ideal ADS

The ADS axioms couple spring update to oscillation amplitude. In order to build an ADS, it is simpler to couple spring update directly to the oscillation functions u_T and u_H (Fig. S1D), since these degrees of freedom are more readily accessible. Here we consider the problem of finding relationships between ψ and the node oscillations u_T, u_H , which satisfy the ideal ADS axioms (3b) and (3c), with $\delta = 0$. In this idealized scenario, we also assume that u_T and u_H oscillate at approximately the same frequency with a phase shift approximately equal to 0 or π . Concretely, we assume u_T and u_H can be written (Fig. S1D)

$$u_T = A_T \cos \omega t \quad u_H = A_H \cos \omega t \quad (4)$$

with $A_i \in \mathbb{R}$. We aim to find an update rule of the form

$$\dot{\psi} = f(u_T, \dot{u}_T, \dots, u_H, \dot{u}_H, \dots)$$

which satisfies the ideal ADS axioms (equations 3b and 3c)

$$\langle \dot{\psi} \rangle > 0 \quad \text{if} \quad \langle |u_T| \rangle > \langle |u_H| \rangle, \quad \langle \dot{\psi} \rangle = 0 \quad \text{if} \quad \langle |u_T| \rangle \leq \langle |u_H| \rangle$$

The problem of finding update rules for a physical ADS is addressed in the subsequent section, and accounts for terms such as the threshold δ in ADS axiom 3b, and the phase difference between u_T and u_H .

To satisfy the ADS axioms, we need $\langle \dot{\psi} \rangle > 0$ if $|A_T| > |A_H|$ and $\psi = 0$ otherwise (Fig. S1E). We can write this relationship in terms of u_T and u_H

$$\begin{aligned} |A_T| - |A_H| > 0 &\Leftrightarrow u_T^2 - u_H^2 > 0 \\ &\Leftrightarrow (u_T - u_H)(u_T + u_H) > 0 \end{aligned} \quad (5)$$

Therefore, we need the spring to update over an oscillation cycle if $u_T \pm u_H$ have the same sign, and remain unchanged if $u_T \pm u_H$ have different signs (Fig. S1E). The requirement that the spring only needs to update over an oscillation cycle means that $\dot{\psi}$ can sometimes be 0 when $u_T \pm u_H$ have the same sign (Fig. S1E, shaded region) provided that $\langle \dot{\psi} \rangle > 0$ over a whole cycle. A general form of the allowed update dynamics is therefore given by

$$\dot{\psi} = \Theta(u_T - u_H) \Theta(u_T + u_H) g_1(u_T, u_H) + \Theta(u_H - u_T) \Theta(-u_T - u_H) g_2(u_T, u_H) \quad (6)$$

where g_1 and g_2 are non-negative functions from $\mathbb{R} \rightarrow \mathbb{R}$, and Θ is the Heaviside step function. The first term in equation (6) selects the right hand quadrant in Fig. S1E, and the second term selects the left hand quadrant. The requirement that $\langle \dot{\psi} \rangle > 0$ over an oscillation cycle imposes an additional constraint on g_1 and g_2 . A straightforward way to satisfy this condition is to restrict equation (6) to the case where at least one of the functions g_1, g_2 is strictly positive.

The same argument as in equation (5) holds when u_i is replaced with \dot{u}_i . This allows us to write

$$\dot{\psi} = \Theta(\dot{u}_H - \dot{u}_T) \Theta(-\dot{u}_T - \dot{u}_H) g_1(\dot{u}_T, \dot{u}_H) + \Theta(\dot{u}_T - \dot{u}_H) \Theta(\dot{u}_T + \dot{u}_H) g_2(\dot{u}_T, \dot{u}_H) \quad (7)$$

Setting $g_2 = 0$ and $g_1 \propto \text{Relu}(-\dot{u}_1 - \dot{u}_2)$ gives

$$\dot{\psi} \propto \Theta[\dot{u}_H - \dot{u}_T] \text{Relu}[-\dot{u}_T - \dot{u}_H] \quad (8)$$

This is essentially the update rule satisfied by our physical realization of an ADS, up to constant scale factors. Our physical implementation necessarily has additional thresholds within the Relu and Heaviside functions, reflecting the fact that the calculation used to obtain equation (8) is essentially a zeroth order calculation, neglecting terms like the phase difference between u_T and u_H and the threshold δ in ADS axiom (3b). Furthermore, a physical implementation will not be an ideal ADS, and can only satisfy the ADS axioms up to certain tolerances.

Equation (5) also highlights the importance of the degrees of freedom $u_T \pm u_H$ in the ADS. As stated above, to leading order, the spring only updates if $u_T \pm u_H$ have the same sign. In our chosen coordinates (Fig. S1D) the spring extension, $\eta(t)$, is given by

$$\eta(t) = -(u_T - u_H)$$

and so captures one of these degrees of freedom. We use θ to denote the other degree of freedom

$$c_0\theta(t) = -(u_T + u_H)$$

where c_0 is some (positive) proportionality constant. We can write these oscillators together as

$$\begin{pmatrix} \eta \\ c_0\theta \end{pmatrix} = \begin{pmatrix} -1 & 1 \\ -1 & -1 \end{pmatrix} \begin{pmatrix} u_T \\ u_H \end{pmatrix} \quad (9)$$

The above argument shows that, to leading order, an ADS changes its stiffness if and only if θ and η have the same sign over an oscillation. In other words

$$\langle \dot{\psi} \rangle > 0 \Leftrightarrow \text{sgn}(\eta\theta) = +1 \quad (10)$$

In section IB, we show how θ can be realized by coupling a pendulum to a spring.

3. Directional update rules for a physical ADS

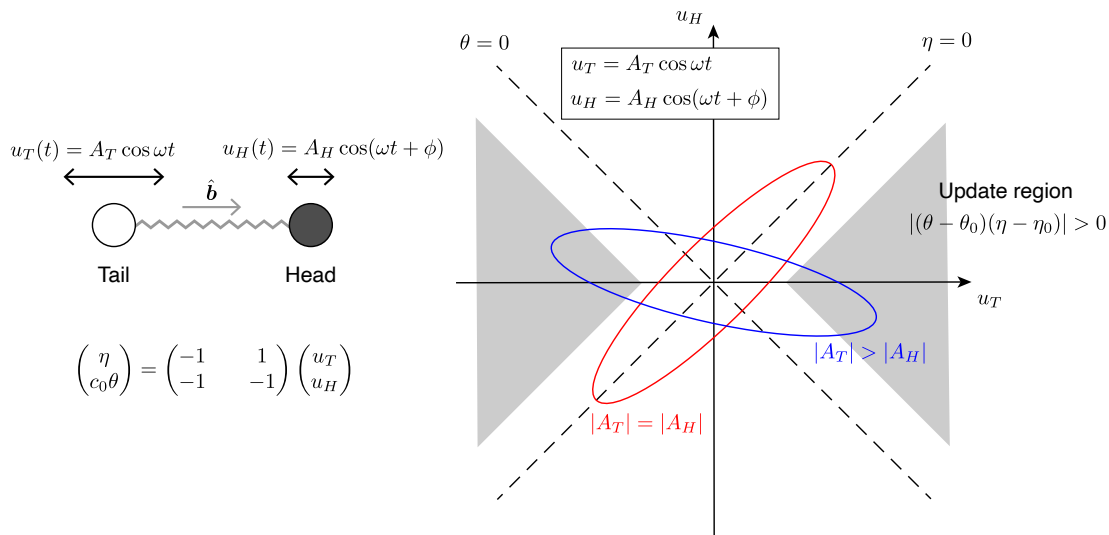


FIG. S2. **Update rules and tolerances for a physical ADS.** Example trajectories of curves $(u_T, u_H) = (A_T \cos \omega t, A_H \cos(\omega t + \phi))$ are shown in the (u_T, u_H) -plane for $|A_T| \leq |A_H|$ (red curve) and $|A_T| > |A_H|$ (blue curve). The update region (grey) denotes the values of u_T, u_H for which the spring is allowed to update. To satisfy the ADS axioms, trajectories with $|A_T| \leq |A_H|$ must lie entirely outside the update region.

To find update rules that relate ψ and u_T, u_H for a physical ADS, we can proceed in a similar way as above. In this case, we assume a phase difference ϕ between u_T and u_H and nonzero threshold δ in the directional update axiom (equation 3b). Specifically, we assume u_T and u_H can be written (Fig. S2)

$$u_T = A_T \cos \omega t \quad u_H = A_H \cos(\omega t + \phi) \quad (11)$$

The curves given by this equation are ellipses in the (u_T, u_H) -plane (Fig. S2). To see this, observe that we can write the curve as

$$\begin{pmatrix} u_T(t) \\ u_H(t) \end{pmatrix} = \begin{pmatrix} A_T & 0 \\ A_H \cos \phi & -A_H \sin \phi \end{pmatrix} \begin{pmatrix} \cos \omega t \\ \sin \omega t \end{pmatrix}$$

To find an update rule for a physical ADS, we require $\dot{\psi}$ to satisfy the ADS axioms (equations 3b and 3c)

$$\langle \dot{\psi} \rangle > 0 \quad \text{if} \quad \langle |u_T| \rangle > \langle |u_H| \rangle + \delta, \quad \langle \dot{\psi} \rangle = 0 \quad \text{if} \quad \langle |u_T| \rangle \leq \langle |u_H| \rangle$$

Modifying equation (8) to include tolerances provides a possible update rule. Defining η and θ as in equation (9) the update rule from equation (8) has the form

$$\dot{\psi} \propto \text{Relu}(\dot{\theta}) \Theta(\dot{\eta})$$

Working with θ and η as opposed to their time-derivatives, we can write down a similar update rule with thresholds as in Fig. S2

$$\dot{\psi} \propto \text{Relu}(\theta - \theta_0) \Theta(\eta - \eta_0)$$

The update region according to this rule is shown in Fig. S2. The spring will update if the elliptical u_T, u_H trajectories hit the shaded region (Fig. S2). As demonstrated pictorially in Fig. S2, the combination of the thresholds in the update rule, and the phase difference ϕ lead to ADS-like behavior. This behavior could breakdown however, for example when $\phi = \pi/2$ and A_T, A_H are sufficiently large, update will always occur. Nevertheless, such an update rule robustly produces ADS behavior, as defined by the axioms (equation 3). This is shown in simulations in section IV. Finally, we note that the update rule for our physical ADSs has thresholds and is given in terms of $\dot{\eta}$ and $\dot{\theta}$

$$\dot{\psi} \propto \text{Relu}(\dot{\theta} - \tau_0) \Theta(\dot{\eta} - \tau_1) \quad (12)$$

where τ_0, τ_1 are thresholds which arise due to internal friction within our physical ADS mechanism.

4. Symmetries of an ADS

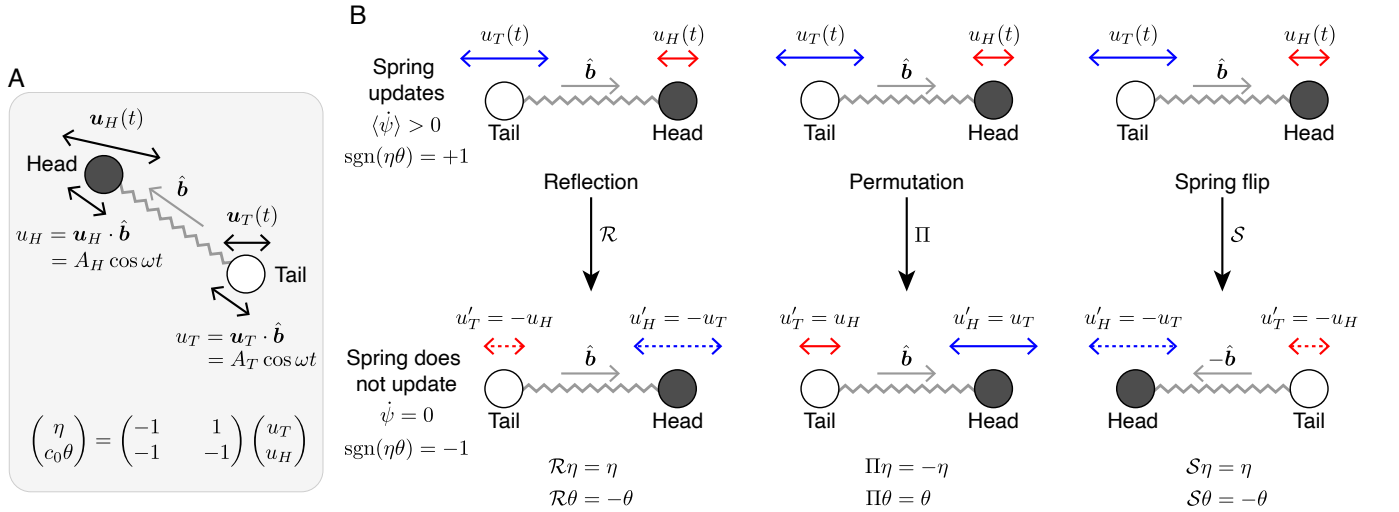


FIG. S3. **Symmetries of an ADS** (A) Summary of quantities associated with an ADS. $\hat{\mathbf{b}}$ is a unit vector pointing from the tail of the ADS (white circle) to the head (grey circle). The oscillations of the head and tail are given by $\mathbf{u}_H(t)$ and $\mathbf{u}_T(t)$ respectively. The oscillations in the direction of the spring are given by the scalar quantities $u_T = \mathbf{u}_T \cdot \hat{\mathbf{b}}$ and $u_H = \mathbf{u}_H \cdot \hat{\mathbf{b}}$. From the ADS axioms (equation 3), the spring updates if and only if $\langle u_T^2 \rangle > \langle u_H^2 \rangle$. Assuming that we can write $u_i = A_i \cos \omega t$ (equation 4), the spring updates if and only if $\eta = u_H - u_T$ and $\theta \propto -(u_T + u_H)$ have the same sign, i.e. if and only if $\text{sgn}(\eta\theta) = +1$. (B) Transformations which interchange the head and tail oscillations, u_T, u_H , in various ways, will typically alter whether or not the spring updates. We define reflection \mathcal{R} (column 1), and permutation Π (column 2) as transformations which only affect u_T (blue arrows) and u_H (red arrows). The spring flip operation \mathcal{S} (column 3), reverses the direction of the spring, affecting $\hat{\mathbf{b}}$ (grey arrows). Oscillations with flipped sign, $u_i \mapsto -u_j$, are denoted with a dashed arrow. The transformations $\mathcal{R}, \Pi, \mathcal{S}$ are given explicitly in equation (13). The top row depicts configurations in which the spring updates, so $\text{sgn}(\eta\theta) = +1$ (equation 10). By flipping the sign of one of η, θ and not the other, each transformation (\mathcal{R}, Π and \mathcal{S}) results in dynamics for which the spring does not update, and has $\text{sgn}(\eta\theta) = -1$. Spring flip (column 3) is equivalent to reflection (column 1), as can be seen by the action of \mathcal{S} and \mathcal{R} on η and θ .

The directionality of an ADS means that interchanging its oscillations on either end, u_T and u_H , should modify the update behavior of the spring. Here, we explore how an ideal ADS responds to various transformations of its inputs, with a particular focus on the role of the degrees of freedom $u_T \pm u_H$ (equation 9).

As depicted in Fig. S3A, a general ADS has tail-head axis $\hat{\mathbf{b}}$, and tail and head oscillations given by $\mathbf{u}_T(t)$ and $\mathbf{u}_H(t)$ respectively. The oscillations in the direction of the spring are given by $u_i = \mathbf{u}_i \cdot \hat{\mathbf{b}}$ (equation 2), and the oscillators η and θ are defined by equation (9). Under the assumption that $u_i = A_i \cos \omega t$ (equation 4), the ADS axioms mean that the spring updates if and only if $\text{sgn}(\eta\theta) = +1$ (equation 10).

Transformations of the oscillations u_T and u_H affect the ADS response by changing $\text{sgn}(\eta\theta)$ (Fig. S3B). We define reflection and permutation transformations, \mathcal{R} and Π , as operations which fix the tail-head axis, $\hat{\mathbf{b}}$, but interchange u_T and u_H as follows

$$\begin{aligned} \mathcal{R}u_T &= -u_H & \Pi u_T &= u_H \\ \mathcal{R}u_H &= -u_T & \Pi u_H &= u_T \end{aligned}$$

The reflection operator switches u_T and u_H and flips their sign, whereas the permutation operator only switches u_T and u_H (Fig. S3B, columns 1 and 2). The spring flip operator, \mathcal{S} reverses the direction of the spring and so switches u_T and u_H (Fig. S3B, column 3). However, since the oscillation terms are defined with respect to the tail-head axis $\hat{\mathbf{b}}$, flipping the axis also flips the sign of all the oscillation terms. The spring flip transformation is therefore equivalent to reflection (Fig. S3B, column 3). We can therefore write the transformations $\mathcal{R}, \Pi, \mathcal{S}$ as matrices acting on column vectors $(u_T, u_H)^\top$

$$\mathcal{R} = \mathcal{S} = \begin{pmatrix} 0 & -1 \\ -1 & 0 \end{pmatrix} \quad \Pi = \begin{pmatrix} 0 & 1 \\ 1 & 0 \end{pmatrix} \quad (13)$$

These transformations are diagonal in the η, θ basis

$$\begin{aligned} \mathcal{R}\eta &= \eta & \Pi\eta &= -\eta \\ \mathcal{R}\theta &= -\theta & \Pi\theta &= \theta \end{aligned}$$

Since \mathcal{R}, \mathcal{S} and Π flip the sign of exactly one of η and θ , these transformations must flip the sign of $\eta\theta$. By equation (10), we therefore have that \mathcal{R}, \mathcal{S} and Π map an updating spring, with $\text{sgn}(\eta\theta) = +1$ to a fixed spring, with $\text{sgn}(\eta\theta) = -1$. Interestingly, reflection fixes the spring extension, η , and flips the sign of θ , whereas permutation fixes θ but flips the sign of η .

5. Extensions of the ADS concept

The ADS axioms described above (equation 3) can be generalized to account for displacements in different dimensions. In general, the head and tail oscillations are given by $\mathbf{u}_H(t)$ and $\mathbf{u}_T(t)$ (Fig. S4A). As constructed above, the ADS axioms specify spring update in terms of $\langle u_T \rangle^2 - \langle u_H \rangle^2$, where

$$u_T = \mathbf{u}_T \cdot \hat{\mathbf{b}}, \quad u_H = \mathbf{u}_H \cdot \hat{\mathbf{b}}$$

and $\hat{\mathbf{b}}$ is the tail-head axis of the ADS. We could incorporate directional adaptivity by projecting the oscillations \mathbf{u}_T and \mathbf{u}_H in a direction distinct from $\hat{\mathbf{b}}$. In 2D, a natural choice is to project perpendicularly to $\hat{\mathbf{b}}$ (Fig. S4B,C)

$$u_T^\perp = \mathbf{u}_T \wedge \hat{\mathbf{b}}, \quad u_H^\perp = \mathbf{u}_H \wedge \hat{\mathbf{b}}$$

We can modify ADS axioms (3b) and (3c) to be in terms of u_T^\perp and u_H^\perp . We call the resulting object ADS'

$$\langle \dot{\psi} \rangle > 0 \quad \text{if } \langle |u_T^\perp| \rangle > \langle |u_H^\perp| \rangle \quad (\text{Directional adaptivity}) \quad (14a)$$

$$\dot{\psi} = 0 \quad \text{if } \langle |u_T^\perp| \rangle \leq \langle |u_H^\perp| \rangle \quad (\text{Self-regulation}) \quad (14b)$$

where ψ governs the spring stiffness, $k = k(\psi)$. Assuming that we can write the node oscillations as $\mathbf{u}_i = \mathbf{A}_i \cos \omega t$ (equation 4), we have that

$$\langle \dot{\psi} \rangle > 0 \Leftrightarrow \text{sgn} [(u_T^\perp - u_H^\perp)(u_T^\perp + u_H^\perp)] = +1 \quad (15)$$

The ADS' therefore updates if it rotates anticlockwise ($u_T^\perp - u_H^\perp > 0$) at the same time as moving downwards ($u_T^\perp + u_H^\perp > 0$), or rotates clockwise at the same time as moving upwards (Fig. S4C).

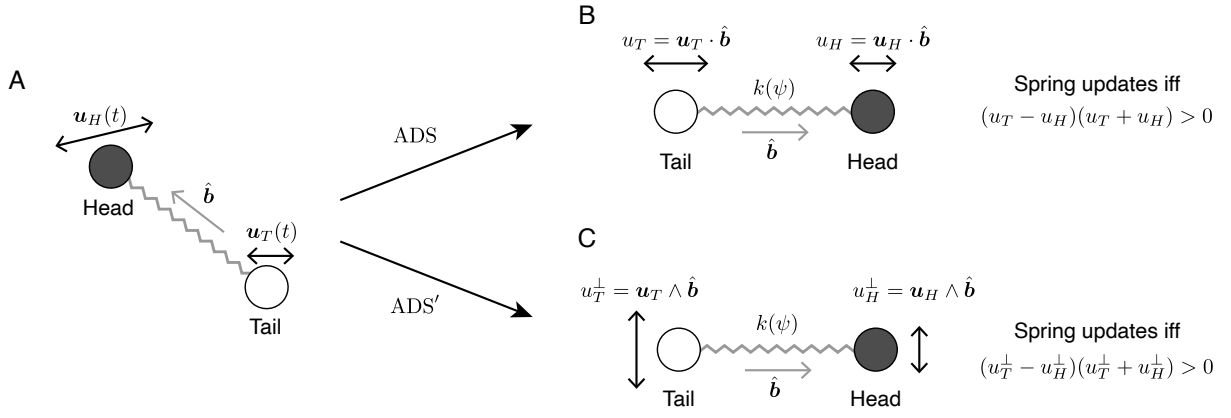


FIG. S4. **Generalizations of the ADS in higher dimensions** (A) A generic ADS in 2D, with vector $\hat{\mathbf{b}}$ pointing from tail to head. We can rotate the spring so the tail-head axis points along the positive x -direction. We assume that we can write the node oscillations as $\mathbf{u}_i = \mathbf{A}_i \cos \omega t$ (equation 4). (B) The ADS described by equation (3) focuses on oscillations parallel to the spring, $u_i = \mathbf{u}_i \cdot \hat{\mathbf{b}}$. The spring updates if and only if the tail oscillations are larger than the head oscillations, which here is equivalent to $u_T^2 - u_H^2 > 0$. (C) An alternative ADS, denoted here as ADS', focuses instead on oscillations perpendicular to the spring, $u_i^\perp = \mathbf{u}_i \wedge \hat{\mathbf{b}}$. As with the normal ADS, the spring updates if and only if the tail oscillations are larger than the head oscillations, which is now equivalent to $(u_T^\perp)^2 - (u_H^\perp)^2 > 0$. In other words, the spring updates if it rotates anticlockwise at the same time as moving downwards, or rotates clockwise at the same time as moving upwards.

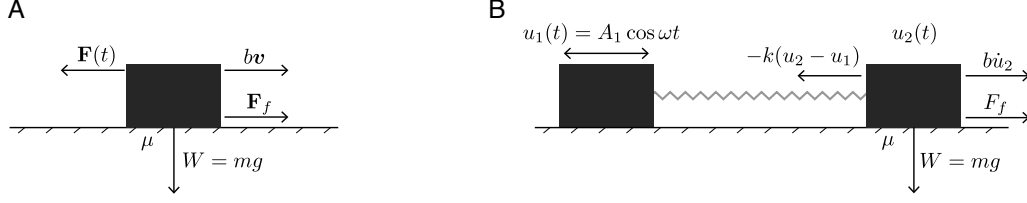


FIG. S5. **Surface friction on a single particle** (A) A single mass m on a surface. The coefficient of friction between the surface and the mass is μ . The mass experiences an external force $\mathbf{F}(t)$, a viscous damping force $b\mathbf{v}$, and a friction force \mathbf{F}_f which depends on \mathbf{v} , \mathbf{F} , and the weight force $W = mg$ (equation 16). (B) Two masses with displacements u_1 and u_2 relative to their rest position are connected by a spring with stiffness k . The motion of the mass on the left is prescribed to be $u_1 = A_1 \cos \omega t$. The second mass experiences a spring force, $-k(u_2 - u_1)$, a viscous damping force $b\dot{u}_2$ and a friction force F_f (equation 17).

B. Mechanical construction of an ADS

In this section, we will show how to construct an ADS out of a sequence of mechanical gadgets. We begin by showing how Coulomb friction gives rise to an activation non-linearity (axiom 3d). Next we show how to construct the spring out of a heterogeneous elastic ring, whose orientation defines the phase angle, ψ , governing adaptivity (axiom 3a). We then introduce mechanical components that break symmetry and induce directional behavior within the spring. This is achieved by coupling a pendulum to a spring: the pendulum and spring extension are the oscillators described by $u_T \pm u_H$ (Fig. S1D, equation 9), which gives rise to directionality. Finally, we sketch how ψ can be coupled to the oscillations of the spring extension and the pendulum in order to satisfy axioms (3b) and (3c). A detailed description of this ψ coupling is given in section II.

1. Surface friction

Surface friction naturally gives rise to an activation non-linearity of the form required by the ADS axioms (equation 3d). Consider a mass m , with position $\mathbf{x}(t)$, on a surface, with coefficient of friction μ between the mass and the surface (Fig. S5A). For simplicity, we assume the coefficients of static and dynamic friction are equal. Suppose the mass experiences a time-dependent force $\mathbf{F}(t)$, along with a viscous damping force, $b\mathbf{v}$, where $\mathbf{v} = \dot{\mathbf{x}}$. The total non-friction force on the mass is then

$$\mathbf{F}_0(t) = \mathbf{F}(t) - b\mathbf{v}$$

There are many ways to formulate Coulomb friction [1–7]. In general, the friction force, \mathbf{F}_f can depend on the velocity, and total non-friction force, \mathbf{F}_0

$$m\dot{\mathbf{v}} = \mathbf{F}_0(t) + \mathbf{F}_f(\mathbf{v}, \mathbf{F}_0; \mu mg)$$

Following references [6, 7], we choose

$$\mathbf{F}_f(\mathbf{v}, \mathbf{F}_0; \mu mg) = \begin{cases} -\mu mg \hat{\mathbf{v}} & \text{if } |\mathbf{v}| > 0 \\ -\min(\mu mg, |\mathbf{F}_0|) \hat{\mathbf{F}}_0 & \text{if } |\mathbf{v}| = 0 \end{cases} \quad (16)$$

where $\hat{\mathbf{F}}_0$ is a unit vector in the \mathbf{F}_0 direction, provided \mathbf{F}_0 is non-zero, and $\hat{\mathbf{F}}_0 = \mathbf{0}$ otherwise. $\hat{\mathbf{v}}$ is defined similarly.

To understand how the friction law above gives rise to ADS axiom 3d, consider a classical spring, with (constant) stiffness k , joining two nodes of mass m . For simplicity, we work in 1D (Fig. S5B). The displacements of the nodes relative to their rest positions are $u_1(t)$ and $u_2(t)$. We choose coordinates so that node 2 is to the right of node 1 and the spring extension is $u_2 - u_1$. Suppose the motion of node 1 is prescribed to be $u_1 = A_1 \cos \omega t$ (Fig. S5B). Then the equation of motion for u_2 is

$$\begin{aligned} m\ddot{u}_2 &= -b\dot{u}_2 - k(u_2 - A_1 \cos \omega t) + F_f(\dot{u}_2, F_0; \mu mg) \\ F_0 &= -b\dot{u}_2 - k(u_2 - A_1 \cos \omega t) \end{aligned} \quad (17)$$

Now let $\dot{u}_2 = 0$, so the total non-friction force is $F_0 = -k(u_2 - u_1)$. Using the friction law (16), the total force on node 2 is therefore

$$\begin{aligned} F_{\text{tot}} &= F_0 + F_f = -k(u_2 - u_1) + \min(\mu mg, k|u_2 - u_1|) \operatorname{sgn}(u_2 - u_1) \\ &= \begin{cases} 0 & \text{if } k|u_2 - u_1| < \mu mg \\ -k(u_2 - u_1) + \mu mg \operatorname{sgn}(u_2 - u_1) & \text{if } k|u_2 - u_1| > \mu mg \end{cases} \end{aligned}$$

We can rewrite this in terms of a Relu function

$$|F_{\text{tot}}| = \operatorname{Relu}(k|u_2 - u_1| - \mu mg)$$

The friction force described above therefore satisfies the required ADS axiom (equation 3d).

Some authors take a friction term which is purely velocity dependent [1, 2, 5]

$$F_f(\mathbf{v}, \mathbf{F}_0; \mu mg) = -\mu mg \hat{\mathbf{v}} \quad (18)$$

We note that this friction law behaves very similarly to the friction law described above. A typical equation of motion involving this friction force will have the form

$$m\dot{\mathbf{v}} = \mathbf{F}_0 - \mu mg \hat{\mathbf{v}}$$

If $|\mathbf{F}_0| < \mu mg$, then the dynamics is pinned at $\mathbf{v} = \mathbf{0}$. To see this, consider the 1D version of the above equation

$$m\dot{v} = F_0 - \mu mg \operatorname{sgn}(v)$$

We can approximate $\operatorname{sgn}(v)$ function using the arctan function

$$m\dot{v} = F_0 - \mu mg \frac{2}{\pi} \arctan(av) \quad (19)$$

where $a > 0$ is the approximation parameter: $\arctan(av)$ approaches $\pi \operatorname{sgn}(v)/2$ when $a \rightarrow \infty$. Equation (19) has a stable fixed point at

$$v_0 = \frac{1}{a} \tan\left(\frac{\pi F_0}{2\mu mg}\right)$$

This fixed point approaches 0 in the limit $a \rightarrow \infty$, illustrating the threshold properties of the simplified friction law in equation (18).

2. Adaptive spring

The axiom for ADS adaptivity (equation 3a) introduces a phase angle ψ which governs spring stiffness

$$k = k^0 - \Delta k \cos(\alpha_0 \psi(t) + \alpha_1)$$

This angle motivates our construction of a spring with variable stiffness using an elastic ring which can rotate (Fig. S6A). The rotation angle of the elastic will then correspond to ψ .

More concretely, consider a circular elastic ring with thickness that varies over its circumference (Fig. S6A, top row). When compressed horizontally, the ring deforms into an ellipse (Fig. S6A, bottom row). The points of maximum curvature change between the ellipse and the circle lie along its major and minor axes. However, deforming the thicker portions of the ring is more energetically costly. Therefore, the energy required to compress the circular elastic ring depends on the relative location of the thickest sections of the ring and the points of maximum curvature change on the ellipse (Fig. S6A, bottom row). Thick portions of the ring can be moved to higher curvature regions by rotation (Fig. S6A). A spring can be constructed out of the elastic ring by mounting it on a four-bar linkage in such a way that it is free to rotate (Fig. S6B-D). The stiffness of the spring therefore depends on its rotation angle, ψ , as defined in Fig. S6A.

To leading order, the post-deformation ellipse has 4 points of maximum curvature change, spaced evenly around its perimeter (Fig. S6, bottom row). By symmetry, the stiffness function k must therefore have period $\pi/2$. Taking a lowest Fourier mode approximation, we can therefore write

$$k(t) = k^0 - \Delta k \cos(4\psi(t) + \alpha_1) \quad (20)$$

for some $k^0, \Delta k, \alpha_1$. This is exactly the form required by the ADS adaptivity axiom (equation 3).

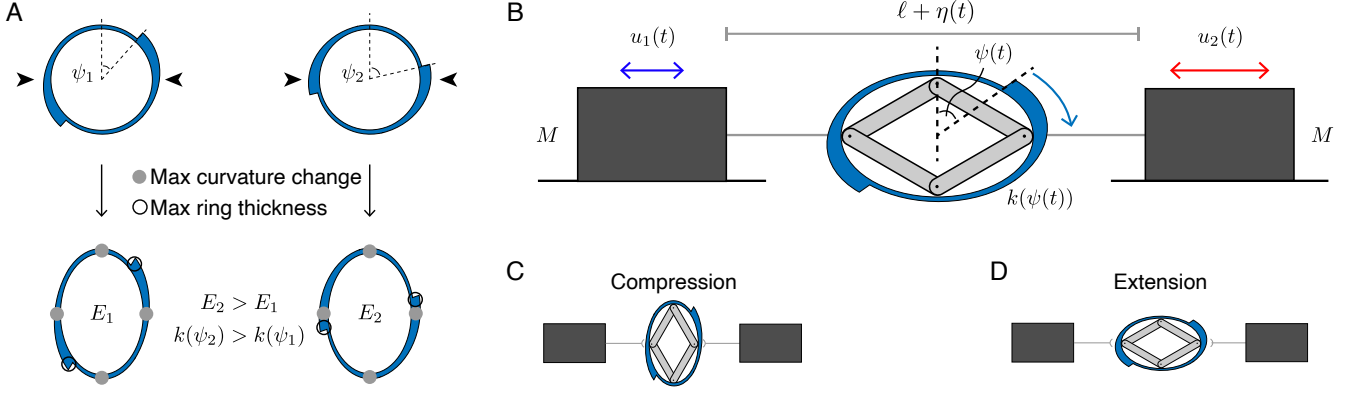


FIG. S6. **Achieving variable spring stiffness through a rotating elastic ring.** (A) A circular elastic ring (blue) with a thickness which varies along its circumference can be used to construct a spring with variable stiffness. At different rotation angles, ψ_i (top row), the energy needed to compress the ring, E_i (bottom row), changes. Compressing the spring horizontally produces an ellipse; the points of maximum curvature change are shown in grey (filled circles). The compression energy is determined by the distance between the thickest regions of the ring (black circles) and the points of maximum curvature change (filled grey circles). (B) An adaptive spring constructed out of the elastic ring from panel (A). The spring consists of the elastic ring mounted on a four-bar linkage and attached to the masses with rigid rods. In order to satisfy the ADS axioms, the ring angle ψ must satisfy $\dot{\psi} > 0$, so the ring can only rotate in one direction (blue arrow). (C,D) Shapes of the spring upon compressing (C) and stretching (D) the spring.

3. Pendulum on a spring

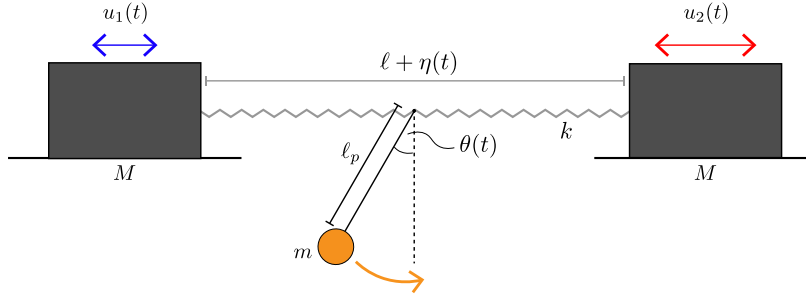


FIG. S7. **Mechanics of a spring coupled to a pendulum.**

Our goal is to construct a spring whose stiffness changes if $u_T \pm u_H$ have the same sign (equation 5), where u_T, u_H are the displacements at the head and tail of the spring (Fig. S1). To do this we need to explicitly realize the degrees of freedom $u_T \pm u_H$. Here, we show that these degrees of freedom can be accessed by coupling a pendulum to an ordinary spring (Fig. S7). In particular, we will let the pendulum angle be θ , and show that it coincides with the definition of $\theta \propto -(u_T + u_H)$ defined above (equation 9). The choice of orientation for the pendulum angle will set a direction for the spring, allowing us to define a head and a tail.

Since a classical spring is symmetric and lacks a head and a tail, we will initially denote the positions of each node by x_1 and x_2 , and their relative displacements from rest by $u_1(t), u_2(t)$ (Fig. S7). We orient the spring with node 2 to the right of node 1, so that the spring extension η is given by $\eta = u_2 - u_1 = x_2 - x_1 - \ell$, where ℓ is the rest length of the spring. The spring additionally has stiffness k , and the two nodes have mass M . The coupled pendulum has mass m , and length ℓ_p (Fig. S7). The pendulum angle is θ , so the pendulum vector is $\mathbf{n}_\theta = (\sin \theta, -\cos \theta)$. We choose the positive θ direction to point from node 1 to node 2 (Fig. S7, orange arrow).

The pendulum mass then has position, $\mathbf{r}_p(t)$ given by

$$\begin{aligned}\mathbf{r}_p &= \ell_p \mathbf{n}_\theta + \frac{1}{2}(x_1 + x_2) \mathbf{e}_x \\ \dot{\mathbf{r}}_p &= \ell_p \dot{\theta} \mathbf{n}_\theta^\perp + \frac{1}{2}(\dot{x}_1 + \dot{x}_2) \mathbf{e}_x = \ell_p \dot{\theta} \mathbf{n}_\theta^\perp + \frac{1}{2}(\dot{u}_1 + \dot{u}_2) \mathbf{e}_x\end{aligned}$$

where $\mathbf{n}_\theta^\perp = (\cos \theta, \sin \theta)$. The Lagrangian is thus

$$L = \frac{1}{2}M\dot{u}_1^2 + \frac{1}{2}M\dot{u}_2^2 + \frac{1}{4}m(\dot{u}_1 + \dot{u}_2)^2 + \frac{1}{2}m\ell_p^2\dot{\theta}^2 + \frac{1}{2}m\ell_p(\dot{u}_1 + \dot{u}_2)\dot{\theta} \cos \theta + mg\ell_p \cos \theta - \frac{1}{2}k(u_2 - u_1)^2$$

The equations of motion are

$$\begin{aligned}M\ddot{u}_1 + \frac{1}{2}m \frac{d}{dt} \left(\dot{u}_1 + \dot{u}_2 + \ell_p \dot{\theta} \cos \theta \right) &= -k(u_1 - u_2) \\ M\ddot{u}_2 + \frac{1}{2}m \frac{d}{dt} \left(\dot{u}_1 + \dot{u}_2 + \ell_p \dot{\theta} \cos \theta \right) &= -k(u_2 - u_1) \\ m\ell_p^2\ddot{\theta} + \frac{1}{2}m\ell_p(\ddot{u}_1 + \ddot{u}_2) \cos \theta &= -mg\ell_p \sin \theta\end{aligned}$$

Next we assume that $m/M, \theta \ll 1$, which gives

$$M\ddot{u}_1 = -k(u_1 - u_2) \quad (21a)$$

$$M\ddot{u}_2 = -k(u_2 - u_1) \quad (21b)$$

$$\ell_p \ddot{\theta} = -g\theta - \frac{1}{2}(\ddot{u}_1 + \ddot{u}_2) \quad (21c)$$

To zeroth order, we can write the relationship between η, θ, \ddot{x}_i as

$$\frac{d^2}{dt^2} \begin{pmatrix} \eta \\ 2\ell_p \theta \end{pmatrix} = \begin{pmatrix} -1 & 1 \\ -1 & -1 \end{pmatrix} \begin{pmatrix} \ddot{u}_1 \\ \ddot{u}_2 \end{pmatrix} \quad (22)$$

Now we make the assumption that the nodes approximately oscillate in-phase at the same frequency, so $u_i(t) = A_i \cos \omega t$ (equation 4). The above equation is then equivalent to equation (9) up to constants, provided we make the identification

$$u_T = u_1, \quad u_H = u_2$$

If we chose the positive θ direction for the pendulum (Fig. S7, orange arrow) to point in the other direction, this relationship would be reversed.

Under the assumption that u_1, u_2, η, θ all oscillate with frequency ω , we can write equation 21c as

$$-\omega^2 \theta = -\omega_p^2 \theta + \frac{1}{2\ell_p} \omega^2 (u_1 + u_2)$$

where $\omega_p^2 = g/\ell_p$ is the natural frequency of the pendulum. The relationship between η, θ and u_1, u_2 can then be written to first order in θ

$$\begin{pmatrix} \eta \\ 2\ell_p \left(1 - \frac{\omega_p^2}{\omega^2}\right) \theta \end{pmatrix} = \begin{pmatrix} -1 & 1 \\ -1 & -1 \end{pmatrix} \begin{pmatrix} \ddot{u}_1 \\ \ddot{u}_2 \end{pmatrix} \quad (23)$$

If $\omega_p/\omega \ll 1$, the approximation in equation (22) is valid. The above equation also demonstrates that the spring-pendulum system comes with a frequency switch: when $\omega_p/\omega > 1$, the coefficient of θ flips sign, which has the effect of flipping the head and tail of the spring.

The spring extension η , and the pendulum angle θ , are therefore the two fundamental degrees of freedom that we require to make an ADS, as in equation (10). Following this equation, in section II we will show how to make an ADS which updates only when $\dot{\eta}, \dot{\theta} > 0$. We note that when the nodes are allowed to move in 2D, the required oscillator law still holds (Fig. S3A). The analogue of equation (22) is

$$\frac{d^2}{dt^2} \begin{pmatrix} \eta \\ 2\ell_p \theta \end{pmatrix} = \begin{pmatrix} -\hat{\mathbf{b}}^\top & \hat{\mathbf{b}}^\top \\ -\hat{\mathbf{b}}^\top & -\hat{\mathbf{b}}^\top \end{pmatrix} \begin{pmatrix} \ddot{\mathbf{u}}_1 \\ \ddot{\mathbf{u}}_2 \end{pmatrix}$$

where $\mathbf{u}_1, \mathbf{u}_2$ are the relative displacements of the nodes in 2D and $\hat{\mathbf{b}}$ is a unit vector pointing along the spring in the positive θ direction (i.e. Fig. S7, orange arrow).

Finally, we can write down the full equations of motion for the spring-pendulum system, including forcing and damping terms. Introducing node driving forces $F_i e^{i\omega t}$, node damping forces $b\dot{u}_i$, and a pendulum damping force $b_p\dot{\theta}$, the full equations of motion become

$$M\ddot{u}_1 + b\dot{u}_1 = -k(u_1 - u_2) + F_1 e^{i\omega t} \quad (24a)$$

$$M\ddot{u}_2 + b\dot{u}_2 = -k(u_2 - u_1) + F_2 e^{i\omega t} \quad (24b)$$

$$\ddot{\eta} = \ddot{u}_2 - \ddot{u}_1 \quad (24c)$$

$$\ddot{\theta} + b_p\dot{\theta} = -\omega_p^2\theta - \frac{1}{2\ell_p}(\ddot{u}_1 + \ddot{u}_2) \quad (24d)$$

where $\omega_p^2 = g/\ell_p$ is the natural frequency of the pendulum. In order for equation (22) to hold, we work in the strong forcing regime,

$$\frac{A}{\ell_p} \gg \frac{b_p}{\omega}, \frac{g}{\omega^2 \ell_p}$$

where A is the characteristic amplitude of u_i .

4. Elastic ring on a four-bar linkage

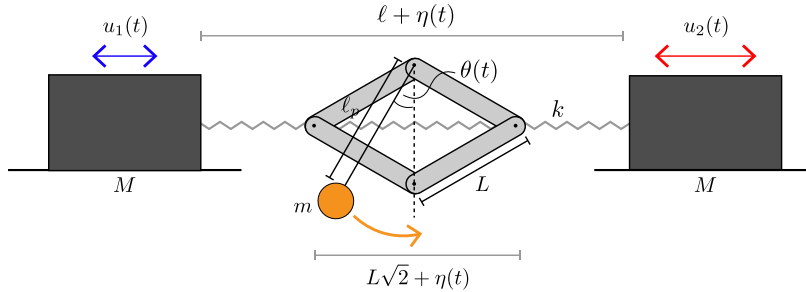


FIG. S8. Mechanics of a spring coupled to a pendulum through a four-bar linkage

A straightforward way to couple the pendulum (Fig. S7) to the elastic ring (Fig. S6) is to attached the pendulum to the four-bar linkage supporting the elastic ring-based adaptive spring (Fig. S6). This introduces additional height fluctuations to the pendulum dynamics described above. In this section, we analyze the problem of a pendulum on a four-bar linkage on spring; a simplified model of this system is shown in Fig. S8. We will show that the height fluctuations are sub-leading, and the analysis of the previous section is therefore valid. The height fluctuations of the pendulum can typically be neglected in realistic dynamical scenarios.

Our notation for the spring, nodes and pendulum remains as in the previous section (Fig. S8). However, the pendulum pivot is now attached to the top of the four-bar linkage. Let this height be z . Then z can be written in terms of the spring extension $\eta = u_2 - u_1$

$$\begin{aligned} z^2 &= L^2 - \frac{1}{4} \left(L\sqrt{2} + \eta \right)^2 \\ &= \frac{1}{2} L^2 - \frac{1}{\sqrt{2}} L\eta - \frac{1}{4} \eta^2 \\ \Rightarrow z &= \frac{1}{\sqrt{2}} L - \frac{1}{2} \eta + O(\eta^2) \end{aligned}$$

The pendulum mass then has position, $\mathbf{r}_p(t)$ given by

$$\begin{aligned}\mathbf{r}_p &= \ell_p \mathbf{n}_\theta + \frac{1}{2}(x_1 + x_2) \mathbf{e}_x + \frac{1}{2}(L\sqrt{2} - \eta) \mathbf{e}_z \\ \dot{\mathbf{r}}_p &= \ell_p \dot{\theta} \mathbf{n}_\theta^\perp + \frac{1}{2}(\dot{u}_1 + \dot{u}_2) \mathbf{e}_x + \frac{1}{2}(\dot{u}_1 - \dot{u}_2) \mathbf{e}_z\end{aligned}$$

where $\mathbf{n}_\theta^\perp = (\cos \theta, \sin \theta)$ as before. The new Lagrangian, L' now includes an extra term

$$\begin{aligned}L' &= L + \frac{1}{2}m\ell_p(\dot{u}_1 - \dot{u}_2)\dot{\theta} \sin \theta \\ L &= \frac{1}{2}M\dot{u}_1^2 + \frac{1}{2}M\dot{u}_2^2 + \frac{1}{4}m(\dot{u}_1 + \dot{u}_2)^2 + \frac{1}{2}m\ell_p^2\dot{\theta}^2 \\ &\quad + \frac{1}{2}m\ell_p(\dot{u}_1 + \dot{u}_2)\dot{\theta} \cos \theta + \frac{1}{2}m\ell_p(\dot{u}_1 - \dot{u}_2)\dot{\theta} \sin \theta + mg\ell_p \cos \theta - \frac{1}{2}k(u_2 - u_1)^2\end{aligned}$$

The equations of motion are

$$\begin{aligned}M\ddot{u}_1 + \frac{1}{2}m \frac{d}{dt} \left(\dot{u}_1 + \dot{u}_2 + \ell_p \dot{\theta} (\cos \theta + \sin \theta) \right) &= -k(u_1 - u_2) \\ M\ddot{u}_2 + \frac{1}{2}m \frac{d}{dt} \left(\dot{u}_1 + \dot{u}_2 + \ell_p \dot{\theta} (\cos \theta - \sin \theta) \right) &= -k(u_2 - u_1) \\ m\ell_p^2 \ddot{\theta} + \frac{1}{2}m\ell_p(\ddot{u}_1 + \ddot{u}_2) \cos \theta + \frac{1}{2}m\ell_p(\ddot{u}_1 - \ddot{u}_2) \sin \theta &= -mg\ell_p \sin \theta\end{aligned}$$

We assume that $m/M, \theta \ll 1$, as before. The equations of motion become

$$\begin{aligned}M\ddot{u}_1 &= -k(u_1 - u_2) \\ M\ddot{u}_2 &= -k(u_2 - u_1) \\ \ell_p \ddot{\theta} &= -g\theta - \frac{1}{2}(\ddot{u}_1 + \ddot{u}_2) + \frac{1}{2}(\ddot{u}_2 - \ddot{u}_1)\theta\end{aligned}$$

Under the assumption that $\ddot{u}_i\theta/\ell_p$ is small, these equations are identical to those of the previous section (equation 21). Thus the picture of the pendulum on a spring (Fig. S7) is sufficient to leading order.

5. Coupling spring stiffness to mechanics

An ADS can be constructed by mounting an elastic ring on a four-bar linkage with a pendulum (Fig. S9A,B). To satisfy the ADS axioms, the pendulum angle θ and spring extension η must be coupled to the elastic ring angle ψ , which determines the spring stiffness $k = k(\psi)$ (Fig. S9A). We couple these degrees of freedom to spring stiffness by allowing the stiffness k to update only when the pendulum swings in the positive direction and the spring extends (i.e. when $\dot{\theta}, \dot{\eta} > 0$)

$$k = k^0 - \Delta k \cos(4\psi + \alpha_0) \quad (25a)$$

$$\dot{\psi} = \gamma \text{Relu}(\dot{\theta} - \tau_0) \Theta(\dot{\eta} - \tau_1) \quad (25b)$$

where $\gamma > 0$ is the learning rate, α_0 is an offset and τ_0 and τ_1 are thresholds that arise due to our construction being a physical (i.e. non-ideal) ADS. The Relu functions ensure that the spring only updates in one direction, $\dot{\psi} \geq 0$. The spring stiffness therefore evolves over moderate timescales as ψ increases from 0 to 2π , instead of simply oscillating rapidly about a fixed value. The minimum and maximum values of k are given by

$$\begin{aligned}k_{\min} &= k^0 - \Delta k \\ k_{\max} &= k^0 + \Delta k\end{aligned}$$

In this construction, directionality arises due to the in-phase and anti-phase oscillations of θ and η . When $\langle u_1^2 \rangle > \langle u_2^2 \rangle$, we have that η and θ oscillate in phase (Fig. S9C, left), and the spring updates. When $\langle u_1^2 \rangle < \langle u_2^2 \rangle$ we have that η and θ oscillate in antiphase (Fig. S9C, right), and the spring does not update. Thus, u_1 is the tail end of the ADS, and u_2 is the head end (Fig. S9A).

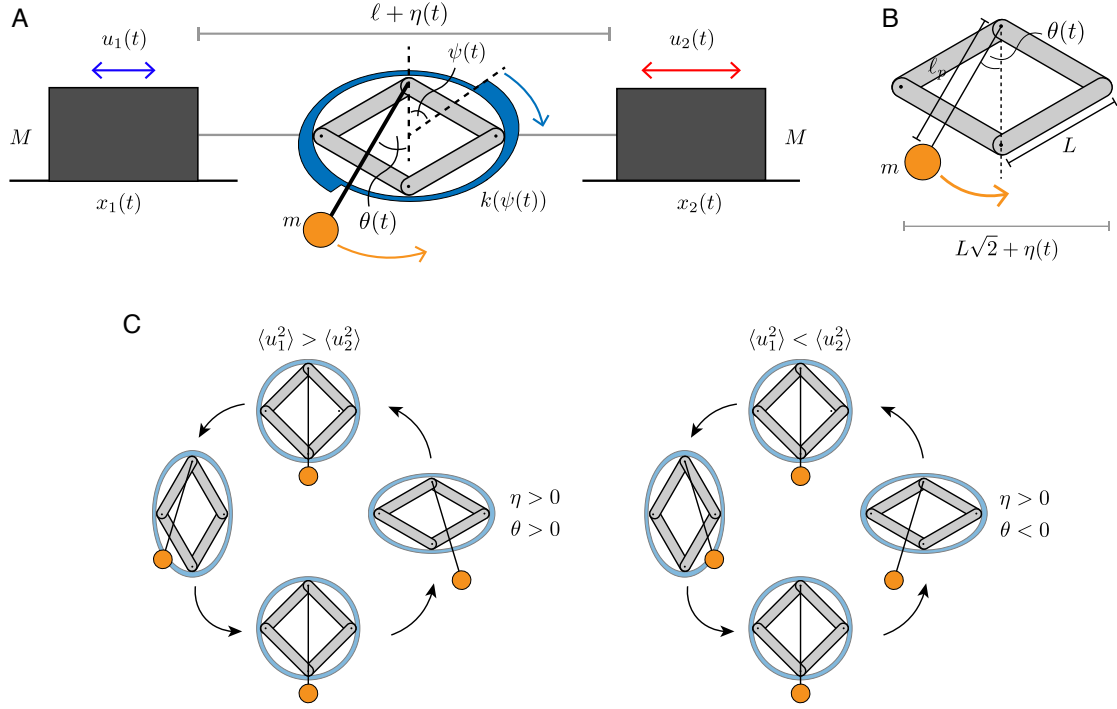


FIG. S9. **Sketch of an adaptive directed spring (ADS).** Free body diagram of an ADS consisting of a non-uniform elastic ring (Fig. S6), a pendulum (Fig. S7) and a four-bar linkage (Fig. S8). (B) Measurements of the linkage and the pendulum from panel (A). (C) Visualizations of the possible oscillation cycles of the pendulum θ , and spring extension, η . These oscillators can either be in-phase (left, $\langle u_1^2 \rangle > \langle u_2^2 \rangle$) or out of phase (right, $\langle u_1^2 \rangle < \langle u_2^2 \rangle$), as described in equation (22). For simplicity these cycles are visualized with a uniform elastic ring (blue). As in equation (22), u_1 can be identified with the tail end of the ADS and u_2 with the head end of the ADS.

II. PHYSICAL REALIZATION

A. ADS design and manufacturing

1. Design

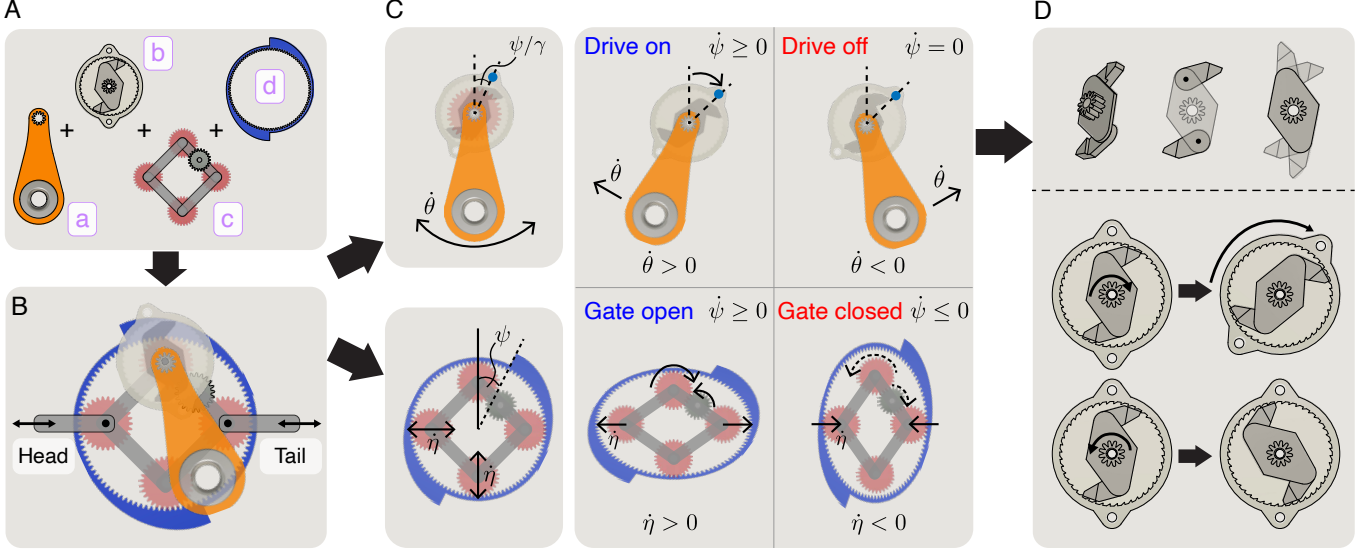


FIG. S10. **Design of an ADS.** (A) The key components of which an ADS is comprised of: (a) a pendulum that acts as the additional oscillator degree of freedom, (b) a ratchet that only allows uni-directional update of ψ , (c) a four-bar linkage and coupling gear that acts as a gating mechanism, and (d) a variable stiffness spring that stiffens and softens as a function of its angle ψ (Fig. S6). (B) Combining these fundamental components produces our implementation of an ADS. (C) We utilize a ratchet and coupling gear mechanism to produce a sign dependent coupling of $\dot{\theta}$ and $\dot{\psi}$ (top row) and $\dot{\eta}$ and $\dot{\psi}$ (bottom row). (D) Detailed illustration of how the ratchet mechanism works.

The physical realization of an ADS must encompass two key functionalities: adaptivity and directionality. **Adaptivity** comes from the continual update in stiffness of a spring. In order to realize a spring that can stiffen and soften, we designed an elastic ring with a variable thickness profile such that under horizontal displacement, the spring displays variable stiffness as a function of its orientation ψ . The elastic ring's cyclic nature is what allows the ADS to continually learn. In order to structurally support the elastic ring, we introduce an upright symmetric four-bar linkage (with equal linkage bar lengths) such that the elastic ring rests on the four hinged points of the linkage mechanism when it is in its untensioned equilibrium state. As a result, the extension and compression of the four-bar linkage (its only degree of freedom) corresponds directly to the extension and compression of the elastic ring. The four-bar linkage is oriented as a diamond. **Directionality** fundamentally comes from the in-phase and anti-phase locking of two oscillators, one oscillator being the intrinsic extension of the spring η , and a second an oscillator we couple to the spring extension θ . In order to do this, we directly mount a pendulum which rotates about the top most hinge point of the four-bar linkage.

As a result, the fundamental components necessary for adaptivity and directionality (Fig. S10A) consist of the pendulum (a), ratchet (b), four-bar linkage and coupling gear (c), and variable elastic ring (d). When linked together (Fig. S10B), these fundamental components result in in-phase and anti-phase locking behavior depending on the head or tail input oscillations (equation 22). We choose an update scheme such that anti-phase locking leads to no update of spring stiffness (this happens when the ADS is driven at its head), while in-phase locking leads to non-zero update of spring stiffness (this happens when the ADS is driven at its tail). Specifically, we choose update to happen only when $\dot{\eta} > 0$ and $\dot{\theta} > 0$. In order to realise this in a physical system, we first couple the pendulum's oscillatory motion $\dot{\theta}$ to the elastic ring's rotation $\dot{\psi}$. Likewise, the four-bar linkage's extension $\dot{\eta}$ has to also be coupled to the elastic ring's rotation $\dot{\psi}$. This is achieved by introducing gears at the hinged points of the four-bar linkage. Gear toothing is also introduced to the inner profile of the elastic ring such that the ring can rotate about the four-bar linkage. Our

goal is couple the pendulum's oscillation rate $\dot{\theta}$ and the four-bar linkage's extension and compression rate $\dot{\eta}$ to the rotation rate of these gears. However, for update to only occur for $\dot{\theta} > 0$, we have to pass $\dot{\theta}$ through a activation function, for example $\dot{\psi} \propto \text{Relu}(\dot{\theta})$. This is realized in the design by passing the pendulum's oscillation through a ratchet, which is in turn linked to the top gear. This is illustrated in the top row of Fig. S10C. The 'drive on' state refers to the configuration where the pendulum's oscillation rotates the ratchet, while the 'drive off' state refers to the configuration where the pendulum's oscillation does not rotate the ratchet. Fig. S10D illustrates how the ratchet works: Two chiral flaps are hinged on a main body (top row). As a result, the flaps engage ratchet teeth during clockwise rotation, but cannot during counter-clockwise rotation (bottom row). Similarly, for update to only occur for $\dot{\eta} > 0$, we have to pass $\dot{\eta}$ through an activation function, for example $\dot{\psi} \propto \Theta(\dot{\eta})$, where Θ is the heavy side step function. In our implementation, we chose to add a coupling gear between the top gear and right adjacent gear such that the sign of $\dot{\eta}$ (compression or extension) produces either counter-clockwise or clockwise torque on the top gear. This is illustrated in the bottom row of Fig. S10C.

An important aspect of this ADS design is that the coupling gear acts as a gating mechanism whereas the pendulum acts as a driver, harvesting energy from oscillations to update the ADS. This means that the coupling gear mechanism can only act to either supplement or suppress the existing θ -dynamics, but does not have enough inertia on its own to update ψ , as this would require rotation of the ratchet body. To best describe this, let us consider the possible states in the configuration space of the ADS: the pendulum can be in the 'drive on' or 'drive off' states, and the spring extension can be in the 'gate open' or 'gate closed' states (Fig. S10C). In the 'drive on' ($\dot{\theta} > 0$) and 'gate closed' ($\dot{\eta} < 0$) state, the pendulum rotates clockwise, and the ratchet engages the ratchet body which in turn exerts a clockwise torque on the top gear. Simultaneously, the four-bar linkage is in the extending state, which exerts a clockwise torque on the top gear. In this scenario, θ and η dynamics act constructively, leading to update of ψ . In the 'drive on' ($\dot{\theta} > 0$) and 'gate open' ($\dot{\eta} > 0$) state, the pendulum rotates clockwise, and the ratchet engages the ratchet body which in turn exerts a clockwise torque on the top gear. Simultaneously, the four-bar linkage is in the compressing state, which exerts a counter-clockwise torque on the top gear. In this scenario, θ and η dynamics act destructively, leading to no update of ψ . In the 'drive off' ($\dot{\theta} < 0$) and 'gate closed' ($\dot{\eta} < 0$) state, the pendulum rotates counter clockwise, and the ratchet does not engage the ratchet body and so no torque is exerted on the ratchet body. Simultaneously, the four-bar linkage is in the compressing state, which exerts a counter clockwise torque on the top gear. However, the gears do not have enough inertia to rotate the entire ratchet body and pendulum, so this scenario leads to no update of ψ . In the 'drive off' ($\dot{\theta} < 0$) and 'gate open' ($\dot{\eta} > 0$) state, the pendulum rotates counter clockwise, and the ratchet does not engage the ratchet body and so no torque is exerted on the ratchet body. Simultaneously, the four-bar linkage is in the extending state, which exerts a clockwise torque on the top gear. However, the gears do not have enough inertia to rotate the ratchet body, so this scenario leads to no update of ψ . We describe the gating mechanism in greater detail in the subsequent section. A consequence of this design is that the ADS has an update rate described by equation 25, reproduced below

$$k = k^0 - \Delta k \cos(4\psi + \alpha_0)$$

$$\dot{\psi} = \gamma \text{Relu}(\dot{\theta} - \tau_0) \Theta(\dot{\eta} - \tau_1)$$

where α_0 is an offset, and τ_0, τ_1 are thresholds arising from internal friction within the ADS mechanism. The learning rate, γ , of the ADS is given by the gear ratio between the top gear and the elastic ring. This learning rate is tunable; in our case $\gamma = 0.3$.

2. Coupling gear gating mechanism

The gear rotations caused by stretching and compressing the spring can be understood using Fig. S11, which depicts the gears mounted on a portion of the four-bar linkage within the ADS. These gears are mounted so that they are always collinear. The top gear is rigidly attached to the ratchet, and can only rotate in the clockwise (positive) direction. Additionally, due to the presence of the ratchet, the applied torque, τ , on the top gear is always in the clockwise direction.

Compression (Fig. S11A) and stretching (Fig. S11B) of the spring cause the line of gears to rotate. Under compression, we have $\dot{\chi} > 0$, whereas under stretching, $\dot{\chi} < 0$, where χ is the angle of the line along which the gears lie (Fig. S11). The central gear, with angular displacement β , responds differently to these two cases. Assuming that the rotational friction on the large gears is much higher than that on the small, central gear, we have that $\dot{\beta} > 0$ when $\dot{\chi} > 0$ and $\dot{\beta} < 0$ when $\dot{\chi} < 0$ (Fig. S11). In the former case, when $\dot{\chi}, \dot{\beta} > 0$, the central gear imparts a large reaction force on the top gear, which can cancel out the positive applied torque, τ , and prevent the gear from rotating

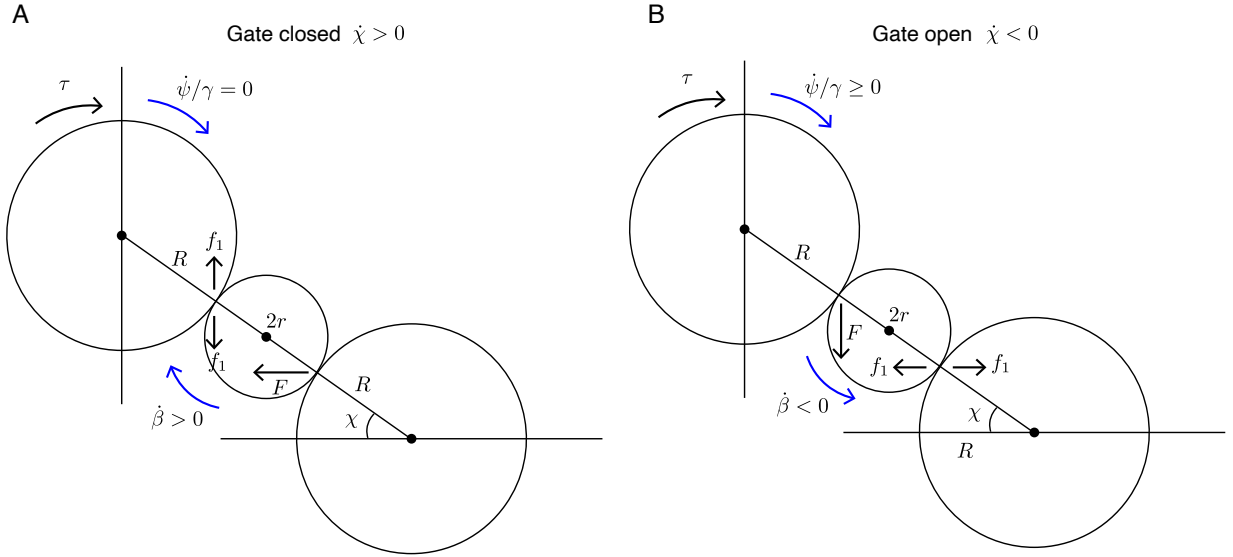


FIG. S11. **Effect of gear mechanics on ADS update.** (A,B) Sketch of gears (circles) used in the ADS. The top gear is rigidly attached to the ratchet and can only rotate in the clockwise (positive) direction. The torque τ on the top gear is always positive, due to the ratchet. The elastic ring rests around the two larger gears. All the gears are mounted on a four-bar linkage in such a way that they are constrained to lie along a line. The central, small gear has angular displacement β , and the top gear has angular displacement ψ/γ , where ψ is the elastic ring angle and γ is a gear ratio. All angles are measured in the clockwise direction. (A) Compression of the spring corresponds to $\dot{\chi} < 0$. The central gear rotates clockwise ($\dot{\beta} > 0$) which applies a reaction force to the top gear, resisting any applied torque $\tau > 0$, resulting in $\dot{\psi} = 0$ ("gate closed"). (B) Extension of the spring ($\dot{\chi} < 0$) causes the central gear to rotate anticlockwise, permitting the top gear to rotate, given an applied torque $\tau > 0$.

(Fig. S11A). Intuitively, these reaction forces arise from the fact that rotating the top gear clockwise ($\dot{\psi} > 0$) when the central gear is already rotating clockwise ($\dot{\beta} > 0$) would cause the gears to lock. When the top gear cannot rotate ($\dot{\psi} = 0$), the ADS cannot update. The $\dot{\chi} > 0$ state, which corresponds to spring compression, is therefore referred to as the "gate closed" state. On the other hand, when $\dot{\chi} < 0$, so the spring is under extension, the central gear rotates anticlockwise, $\dot{\beta} < 0$ (Fig. S11B). In this case, there is no gear constraint to prevent the top gear from rotating clockwise, $\dot{\psi} > 0$. However, under the assumption that the large gears have large rotational friction, the top gear will not rotate unless there is an applied torque τ . This scenario is therefore referred to as the "gate open" case.

3. Fabrication and assembly

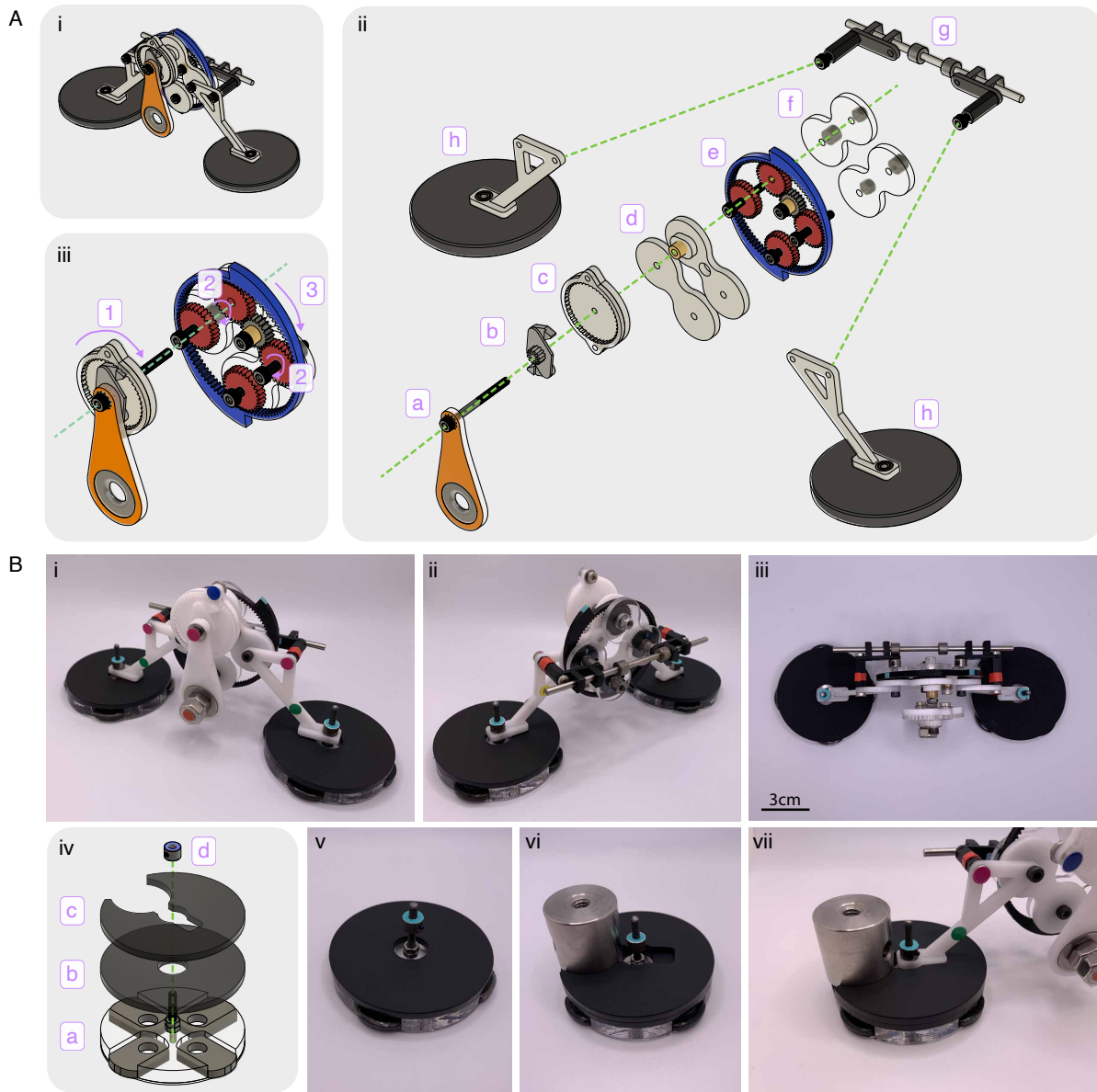


FIG. S12. **Fabrication and assembly of an ADS.** (Ai) Isometric CAD rendering of an ADS. (Aii) Exploded view of ADS with components: (a) Pendulum (b) Ratchet (c) Ratchet teeth and body (d) Front linkages (e) Elastic ring and gears (f) Back linkages (g) Guide rails (h) Legs and passive node. (Aiii) Coupling between pendulum/ratchet and the four-bar linkage. The ratchet (1) is rigidly attached to the top gear (2) of the four-bar linkage. The rotation of the gears (2) leads to rotation of the elastic ring (3) (Bi-iii) Isometric and top view images of the ADS. (Biv) CAD rendering of the nodes, where (a) four washers are stacked on an 60 mm acrylic disk. An m3 rod is threaded to the disk on which the ADS is mounted. (b) A black ring cover is placed above, with an optional additional cover (c) which constrains rotation of connected ADSs about nodes. (d) A shaft collar with a set screw passes through the m3 rod to lock the ADS's leg in place. (Bv) Image of node. (Bvi) Image of node with additional cover (Biv, c) and additional weight. (Bvii) Image of node with ADS's leg locked in place using the additional cover (Biv, c) to prevent rotation.

A full CAD rendering of the ADS is shown in Fig. S12Ai. In addition to the key components described in Fig. S10, additional support structures have been added. Fig. S12Aii shows an exploded view of the ADS, illustrating all the individual components. The pendulum (a) has a washer press fit near its base to increase the pendulum's mass. An m3 rod is passed through the top of the pendulum, but the pendulum is not rigidly coupled to the rod and can

freely rotate. A ratchet (b) is passed through the rod and rigidly press fit to the pendulum. As the ratchet rotates about the rod, its chiral flaps only engage the ratchet body (c) in the clockwise direction, and passively rotate in the counter-clockwise direction. The ratchet body is composed of two laser cut acrylic parts: an acrylic ring (clear) with ratchet teeth that is threaded to a back plate (white). The back plate is directly threaded to the m3 rod and is rigidly fixed by jamming m3 screws against it (double nutting). As a result, when the pendulum and ratchet rotate in the clockwise direction, the ratchet body is engaged which rotates the m3 rod. The m3 rod is additionally rigidly coupled to the top gear (e, red), which is also threaded and jammed with a low-profile m3 screw. As a result, rotation of the ratchet body directly rotates the top gear (Fig. S12Aiii). The ADS contains a symmetric four-bar linkage that is composed of two front (d) and two back (f) linkage bars. The ends of each linkage are hinged about four additional m3 screws. The linkage bars are laser cut, and its profile additionally prevents out of plane motion of the elastic ring. The front linkage bars also contain a linear bushing to support the load of the pendulum (d, yellow). The gears (e, red) are laser cut out of acrylic, and rotate about the four hinged axes of the four-bar linkage. The coupling gear that sits between the top gear and right adjacent gear rests on a second bushing housed at the midpoint of one of the front linkage bars. The elastic ring (e, blue) is printed out of Thermoplastic Polyurethane (TPU) at 80% infill using a 3D printer (Ultimaker). A steel linear guide rail (g) is attached to the four-bar linkage to ensure that oscillations of the ADS remain purely planar, and allows the mechanism to sit upright. The guide rails are lubricated with silicone oil. The entire structure is supported by laser cut ‘leg’ braces that are directly attached to passive nodes (h, black disk).

Images of the constructed ADS are shown in Fig. S12Bi-iii. ADSs are attached to nodes which are weighted circular disks that rest on a friction substrate. The design of the node is shown in Fig. S12Biv, while images of the physical construction of the nodes are shown in Fig. S12Bv-vii. In order to constrain rotation between ADS joints, an additional acrylic cover can be added (Fig. S12Bvi). The majority of the components of the ADS are manufactured using laser cutting and 3D printing (Ultimaker). A few parts are sourced off-the-shelf. The table below lists the material and manufacturing technique of each component.

Component	Material	Manufacturing
Pendulum (a, orange)	3mm acrylic	Laser cutter
Ratchet (b, grey)	NA	Off-the-shelf (Amazon)
Ratchet teeth (c, clear)	1mm acrylic	Laser cutter
Ratchet teeth back-plate (c, white)	3mm acrylic	Laser cutter
Linkage bars (d, white & f, clear)	3mm acrylic	Laser cutter
Sleeve bearings (d & e, yellow)	NA	Off-the-shelf (McMaster-Carr)
Elastic ring (e, blue)	TPU (80% infill)	3D printing
Gears (e, red & grey)	3mm acrylic	Laser cutter
Shaft collars (f,g grey)	NA	Off-the-shelf (McMaster-Carr)
Hexagonal standoffs (g, black)	NA	Off-the-shelf (McMaster-Carr)
Linear sleeve bearings (g, dark grey)	PLA (20% infill)	3D printing
Linear shaft (g, light grey)	Steel	Off-the-shelf (McMaster-Carr)
Support legs (h, white)	3mm acrylic	Laser cutter
Ball bearings (h, black)	NA	Off-the-shelf (McMaster-Carr)
Passive node (h, black)	3mm & 1/4" acrylic	Laser cutter

TABLE I. ADS components.

B. Origin of directionality in adaptive springs

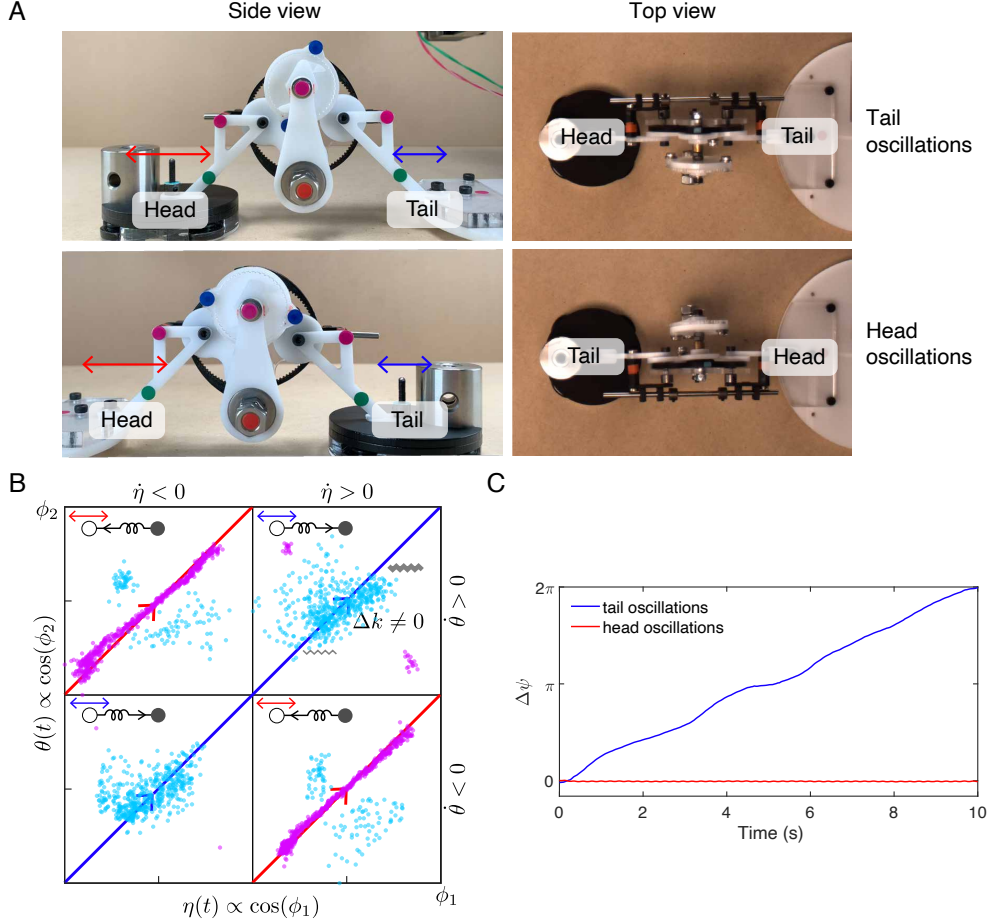


FIG. S13. **Directionality of an ADS.** (A) Side and top view of the ADS undergoing head and tail oscillations. (B) Experimental data demonstrate the phase locking behavior between η and θ . The angles η and θ are measured from the side view videos. The phase angles ϕ_1 and ϕ_2 , defined by $\cos \phi_1 \propto \eta$ and $\cos \phi_2 \propto \theta$, are then plotted (blue and pink points). The η, θ oscillations are in-phase when the ADS is oscillated from the tail (blue points), but are anti-phase under head oscillations (pink points). The driving parameters are $A=6.7\text{mm}$, $f=3.7\text{Hz}$. (C) Experimental data shows the update of the angle ψ as measured from the top view videos. The ADS updates under tail oscillations (blue), but does not update under head oscillation (red). The driving parameters are $A=6.7\text{mm}$, $f=3.7\text{Hz}$.

In this section, we seek to verify the physical picture of directionality in the ADS by conducting control experiments to simplify or alter the existing configuration of the ADS. Fig. S13A illustrates the experimental setup used to oscillate the ADS from its head and tail from both the side view and top view. The side view (directly facing the pendulum) gives us information about the phase coupling between the pendulum θ and the spring extension η . The phase correlations under both tail and head oscillations are shown in Fig S13B, which plots ϕ_1 and ϕ_2 , defined by $\cos \phi_1 \propto \eta$ and $\cos \phi_2 \propto \theta$, on the x and y axis respectively. The solid blue line represents $\phi_1 - \phi_2 = 0$ (in-phase oscillations), whereas the solid red line represents $\phi_1 - \phi_2 = \pi$ (anti-phase oscillations). Experimental data taken from side view videos are plotted (circle markers) for both tail (light blue) and head (pink) oscillations. We designed the ADS such that it updates ($\dot{\psi} > 0$) only when both $\dot{\theta} > 0$ and $\dot{\eta} > 0$ which corresponds to the upper right quadrant in Fig. S13B. The difference in phase coupling ($\phi_1 - \phi_2$) is one aspect of the directional update behavior of ψ , along with the ratchet and coupling gear components which each link the oscillator degrees of freedom to ψ . Fig. S13C illustrates the change in ψ , as measured from the top view, as a function of time for both tail and head oscillations.

1. Directionality in update requires the existence of both η and θ oscillators

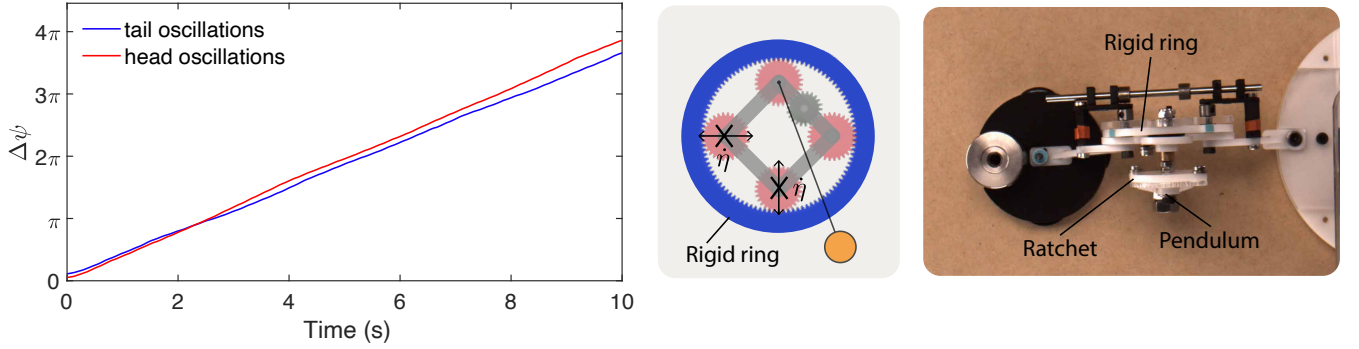


FIG. S14. **Effect of removing the η degree of freedom** The update of the spring is the same under head and tail oscillations (left panel) when the elastic ring is replaced with an effectively rigid acrylic ring of the same dimensions (middle, right panel). The rigidity of the material suppresses deformation of the four-bar linkage. The change in ring angle ψ (measured from the top view) for both head and tail oscillations is shown in the left panel. The driving parameters are $A = 8.7\text{mm}$, $f = 3.27\text{Hz}$.

To demonstrate that the directionality of the ADS relies on the phase coupling between two oscillators, the pendulum, θ and the spring extension η , we conducted control experiments in which the η degree of freedom was suppressed. This configuration is illustrated in Fig. S14 (middle, right panel); we mounted an effectively rigid acrylic ring in place of the elastic ring such that when the ADS is driven, no significant deformation in the four-bar linkage can be observed ($\eta = \dot{\eta} = 0$). However, all the other components of the ADS remain unchanged (including the coupling gear mechanism). We measured the update rate of the rigid ring under both tail and head oscillations at the same amplitude and frequency parameters. As illustrated in the left panel of Fig. S14, the update rate is nearly identical and thus directionality has also been suppressed.

2. Coupling gear produces $\text{sgn}(\dot{\eta})$ dependent torque on the elastic ring

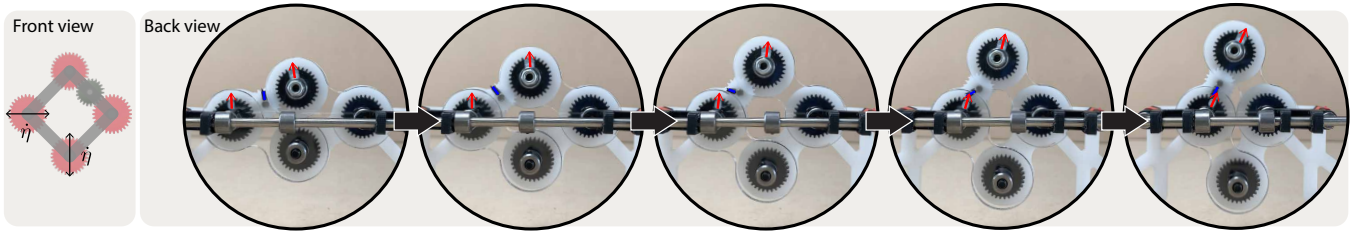


FIG. S15. **Coupling gear mechanism.** Snapshots of the ADS without the elastic ring, pendulum, and ratchet from the side-back view. Red and blue line segments are overlaid on the images to illustrate the rotation of the coupling, top, and adjacent gears.

Fig. S10C (bottom row) and Fig. S11 illustrate the gating effect of the coupling gear: when viewed front-on, as the four-bar linkage moves from a neutral state to a stretched state ($\dot{\eta} > 0$), a counter-clockwise torque is exerted on the coupling gear and a clockwise torque is exerted on the top and right adjacent gears (gate open). When the four-bar linkage moves from a neutral state to a compressed state ($\dot{\eta} < 0$), a clockwise torque is exerted on the coupling gear and a counter-clockwise torque (viewed front-on) is exerted on the top and right adjacent gears (gate closed). In order to illustrate this effect, we removed the pendulum, ratchet, and elastic ring from the ADS (configuration illustrated in Fig. S15, left panel), and imaged the rotation of the gears from the back. When viewed from the back, the top gear rotates clockwise as the four-bar linkage is compressed (Fig. S15, left to right). From the front, this would appear as the top and right gear rotating counter-clockwise when $\dot{\eta} < 0$, as expected. One drawback of the current implementation of the ADS is that the strength of this gating mechanism is limited by the magnitude of η . In cases

where $|\dot{\theta}| \gg |\dot{\eta}|$, directionality can be reduced or suppressed. This might correspond to driving frequencies close to the natural frequency of the pendulum, or very large driving amplitudes. Future iterations of the ADS mechanism will be needed to overcome this limitation.

3. ADS orientation depends on gear mechanism pattern

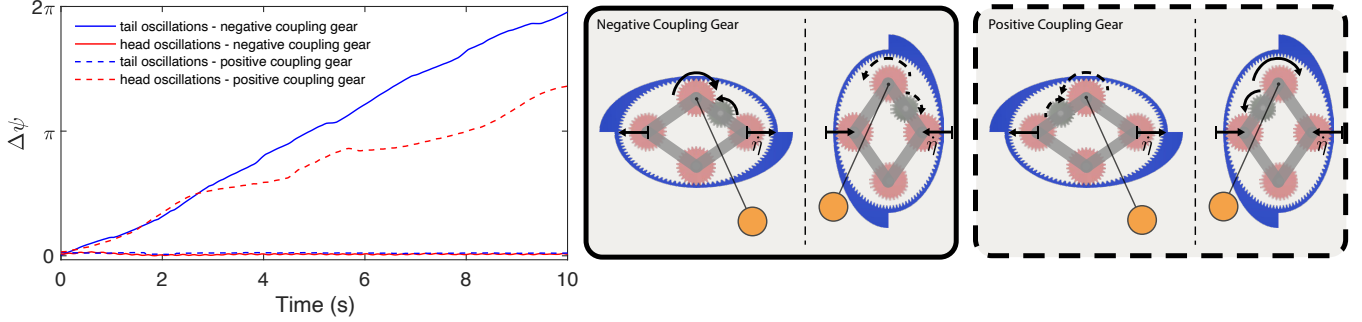


FIG. S16. **Control experiments for effect of coupling gear location.** The coupling gear is switched from being coupled to the right adjacent gear (middle panel) to being coupled to the left adjacent gear (right panel). The measured update of ψ (from the top view) for both tail and head oscillations for both coupling gear configurations are plotted. Head and tail ends are defined with respect to an ADS with negative coupling gear. Switching the coupling gear has the effect of flipping the behavior of the head and tail ends (dotted lines). The driving parameters are $A = 6.7\text{mm}$, $f = 3.68\text{Hz}$.

The head and tail of an ADS clearly depends on the pendulum and ratchet. Here we show that the gear pattern can also affect ADS orientation. In order to verify that the coupling gear gating mechanism (Fig. S10) is indeed a key mechanism responsible for directionality in an ADS, we conducted control experiments where the coupling gear is switched to sit on the left adjacent linkage (we denote this as a “positive coupling gear”) from its original location on the right adjacent linkage (we denote this as a “negative coupling gear”). The configurations are illustrated in Fig. S16 (middle, right panels). The location of the coupling gear affects the directionality of the ADS because it changes the sign of the induced torque on the top gear. The consequence of this is that during compression, a counter-clockwise torque is induced for the negative coupling gear configuration while a clockwise torque is induced for the positive coupling gear configuration. During extension, a clockwise torque is induced for the negative coupling gear configuration while a counter-clockwise torque is induced for the positive coupling gear configuration. This suggests that the head and tail of the ADS would switch. Our experimental results are shown in (Fig. S16, left panel) which indeed shows a change in the directionality of the ADS. To avoid confusion, we denote the head and tail directions of the ADS according to the negative coupling gear configuration. In the normal negative coupling gear configuration, the ADS only updates under tail oscillations. However, in the positive coupling gear configuration, the ADS only updates under what would be head oscillations in the negative coupling gear configuration (Fig. S16). Switching the coupling gear therefore flips the head and tail ends of the ADS. We further verified this result across multiple springs to ensure robustness of manufacturing. We note however that the mean update speed $\langle \dot{\psi} \rangle$ in the positive coupling gear configuration is slightly slower than that of the negative coupling configuration. To explain this, we consider the higher order effects of the linkage deformation in the section below.

4. Higher order effects of four-bar linkage at $k = 0$

As theoretically described in section IB4, the vertical oscillation of the pendulum as the four-bar linkage extends and compresses has (subleading) effects on directionality. This effect is intrinsic to the four-bar linkage, and does not change when the position of the coupling gear changes. As a result, we expect this to be the reason the ring’s update speed is slightly slower in the positive coupling gear configuration (Fig. S16, left panel). However, in order to experimentally verify the existence of this effect, we need to isolate this mechanism from the competing effects of any other component. We therefore conducted control experiments where the coupling gear and elastic ring are removed from the ADS, leaving only the four-bar linkage, pendulum, and ratchet as the remaining key components (Fig. S17). We oscillated the simplified ADS at its head and tail and measured a proxy for the update rate of the

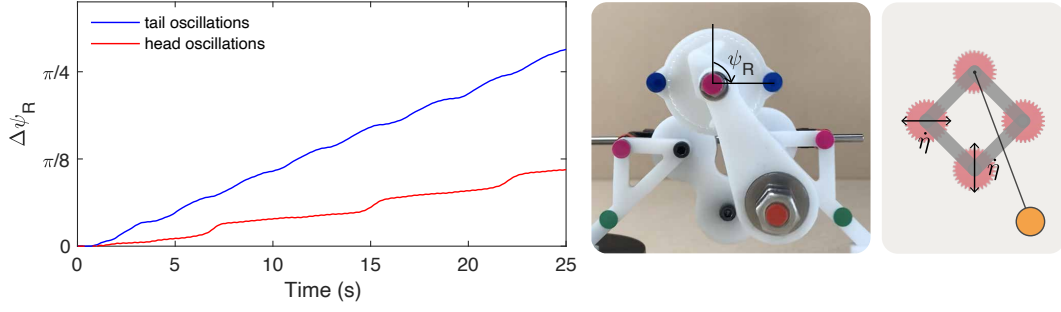


FIG. S17. **Effect of higher order linkage oscillations.** In special situations, the four-bar linkage can give rise to asymmetries in the ADS update rate. Here, the ADS is tested without the coupling gear and without the elastic ring (middle, right panel). As a result, its ability to update is measured via a proxy (ψ_R) from a front view camera. The update rate of ψ_R is plotted for both tail and head oscillations. The driving parameters are $A = 8.7\text{mm}$, $f = 3.68\text{Hz}$.

ring (ψ_R) using the rotation of the ratchet body (Fig. S17, middle panel). The experiment results are shown in Fig. S17 (left panel) which indeed illustrates that the update speed under head oscillations is reduced compared to that of head oscillations. This effect is weak, since $\dot{\psi} \approx \frac{\dot{\psi}_R}{\gamma} = \frac{\dot{\psi}_R}{3}$.

5. Phase coupling is robust to perturbations

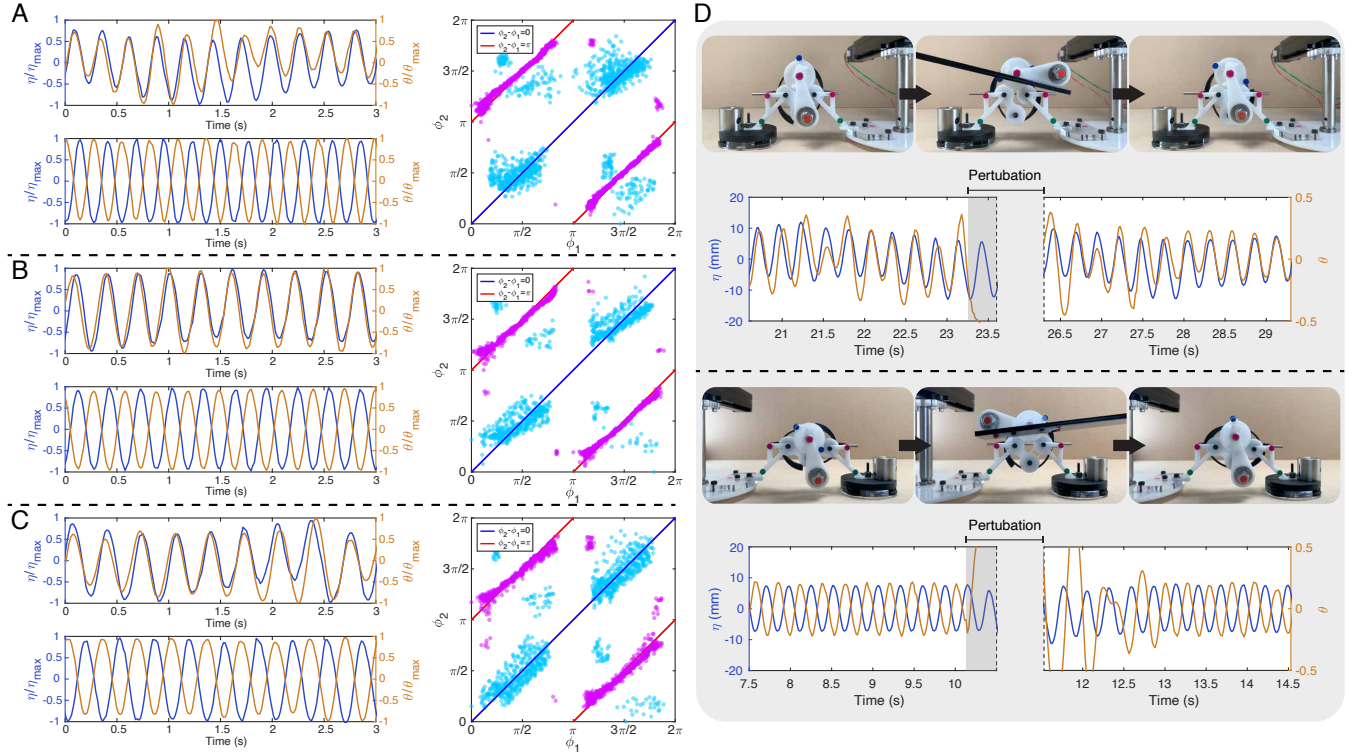


FIG. S18. **Robustness of phase coupling.** (A-C) Phase correlations between η and θ . Left η, θ as a function of time for tail (top) and head (bottom) oscillations at $A=6.7\text{mm}$ and with frequencies of $f=3.7\text{Hz}$, 3.3Hz , and 2.9Hz respectively. The phase angles ϕ_1, ϕ_2 , defined by $\cos \phi_1 \propto \eta$ and $\cos \phi_2 \propto \theta$, are also plotted (right) for tail oscillations (blue circles) and head oscillations (pink circles). (D) The effect of perturbations to θ on phase coupling. η and θ is plotted under tail (top row) and head (bottom row) oscillations (movie S2). The driving parameters are $A=6.7\text{mm}$ and $f=3.7\text{Hz}$.

In-phase and antiphase oscillations of the pendulum, θ and the spring extension η are a key component of the directional update mechanism in our ADS. In order to verify that these phase correlations are robust, we conducted experiments where the ADS is oscillated at various frequencies ($f=3.7\text{Hz}$, 3.3Hz , and 2.9Hz). Fig. S18 A-C illustrates that phase coupling is dependent on frequency in the regime explored. We also conducted experiments to determine if phase coupling is robust to perturbations (Fig. S18D). We perturbed the pendulum (θ) while the ADS was being driven, and measured η and θ before and after the perturbation. Our results indicate that after a transient phase following the induced perturbation, the expected phase coupling behavior is restored (movie S2).

6. *Effect of frequency on the directionality of an ADS*

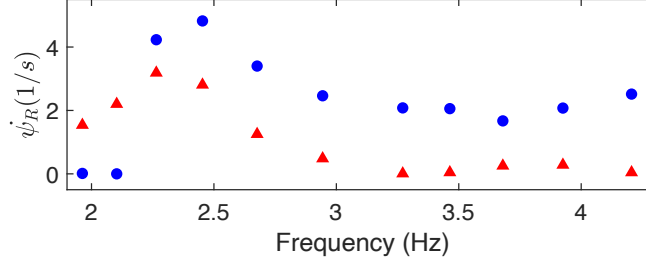


FIG. S19. **Effect of frequency on the update rate of an ADS.** The ADS is oscillated at its head and tail at a constant amplitude of $A = 7.6\text{mm}$, while the frequency is varied. The rate of rotation of the ratchet ($\dot{\psi}_R$) is plotted against frequency.

We explore the effect of frequency on the update rate of an ADS (without its elastic ring) oscillated at its head and tail at constant amplitude (Fig. S19). We measured the rotation rate of the ratchet $\dot{\psi}_R$ as a proxy for the rotation rate, $\dot{\psi}$ of the elastic ring ($\dot{\psi} = \gamma\dot{\psi}_R$ where the gear ratio $\gamma \approx 3$). Inspecting the rotation rate of the ratchet under head and tail oscillations reveals that the ADS retains its expected directionality in the range of 2.9Hz to 4.2Hz . However, directionality is lost near the pendulum's resonance frequency ($\approx 2.3\text{Hz}$), and η and ψ are no longer phase coupled. Above resonance, the directionality of the ADS flips because tail oscillations lead to anti-phase coupling whereas head oscillations lead to in-phase coupling. This effect is captured by equation (23). In our experiments, we restrict our operating frequency to be in the range of 2.9Hz to 3.7Hz .

III. EXPERIMENTAL METHODS

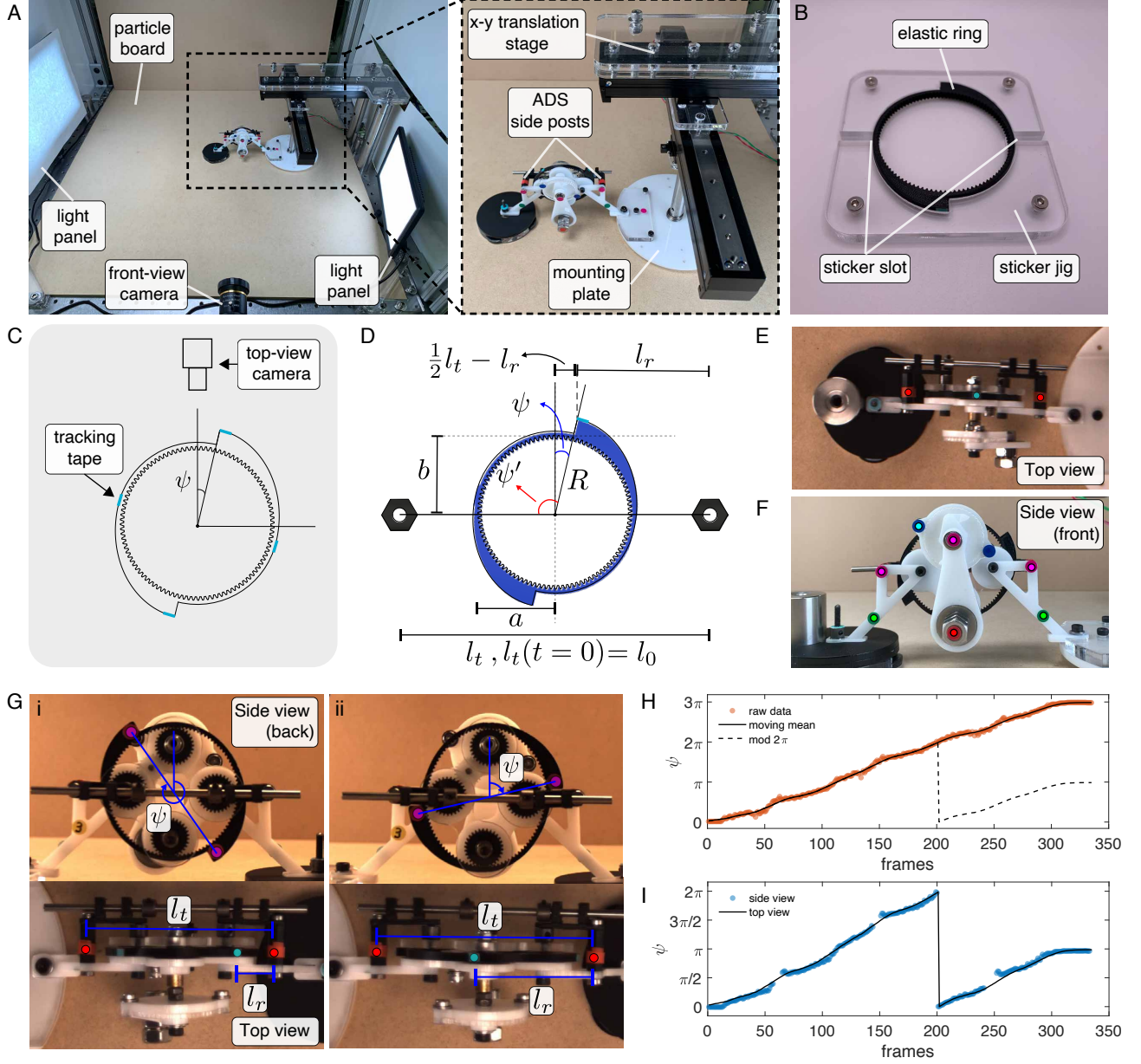


FIG. S20. **Experimental setup and tracking.** (A) Experimental setup, consisting of a particle board that acts as the friction substrate, light panels for illumination, and front and top view (not shown) cameras. The inset shows how the ADS is mounted to the x-y translation stage. (B) Acrylic jig used to mark the elastic ring with tracking tape for image tracking. (C) Illustration of how the top view camera is used to measure the projected location of the tracking tape. (D) Variables measured during image tracking used to infer ψ . (E) Example snapshot of the measured location of the side posts (red), and tracking tape (blue). (F) Example snapshot of the measured locations of the tracking tape used during side view tracking. (G) Example snapshots of the side view and top views used to validate the vertical imaging tracking code for angles of $\psi = 325^\circ$ in i and $\psi = 77^\circ$ in ii. The ADS is oscillated at its tail with driving parameters $A=6.7\text{mm}$, $f=3.7\text{Hz}$. (H) Raw and processed values of ψ as a function of time (frames) as measured from the top view. Video recorded at 20 frames per second. (I) Comparison of the measured values of ψ from the top view and side view.

A. Setup

The experimental setup is shown in Fig. S20A. To oscillate an ADS network, an x-y translation is used to generate sinusoidal motion (Fig. S20A, inset). The x-y stage consists of two synchronized linear translation stages (Kgg Robots SSD30) driven by Nema 11 stepper motors (however in the experiments documented here, only uni-directional oscillation inputs are used). A mounting plate is attached to the stepper motors which allows ADS units to be directly fastened. The translation stages are driven by an Arduino Due and TMC 2209 motor drivers. The ADSs are placed on a 60×60 cm particle board. Two USB cameras (MER2-160-227U3C) with 8mm focal length c-mount lens are mounted at birds-eye (top) and side views. The videos acquired are then post-processed with custom MATLAB (2018b) code.

1. Top view tracking

We measured the angular rotation of the ring by acquiring videos from the top view because it provides full unobstructed view of the elastic ring for all angles ψ . Red tracking tape is placed on side posts of the ADS (as shown in the inset of Fig. S20A) which is used in the tracking code to estimate the elastic ring's deformation. Using an acrylic jig, we placed blue tracking tape at $\pi/2$ intervals along the elastic ring so that as the ring rotates, at least one tracking tape is visible at all times from the top view (Fig. S20B,C). The tracking tape is placed at the ring's radial maxima, and the midpoints between the maxima (Fig. S20C). Our tracking code takes the projected position of the tracking tape from a top view to infer the angle of the elastic ring (ψ). Fig. S20D illustrates the relevant lengths we measure using the tracking code. For a rigid ring, we can directly infer its angle of rotation based on the measured length l_r , and from knowing the radius of the ring at the point of the tracking tape. For an elastic ring, we need to estimate its deformation in order to accurately determine the effective radius. As a result, we use the distance between the side posts (red tracking tape), which are rigidly attached to the four-bar linkage, to determine the compression of the four-bar linkage and in turn the elastic ring. The calculation for ψ is then as follows: First, the separation distance between the two side posts (l_t) is measured, where we denote the resting distance (when the elastic ring is undeformed) to be l_0 . The projected distance of the tracking tape onto the camera can also be measured (l_r). This gives us our first equation,

$$\sin \psi = \frac{\frac{1}{2}l_t - l_r}{R} \quad (26)$$

Next, the deformation of the elastic ring gives an estimate of $R = R(l_t)$. It follows that,

$$R^2 = (a \cos \psi')^2 + (b \sin \psi')^2 \quad (27)$$

where $a = R_0 + \frac{1}{2}(l_0 - l_t)$, $b = R_0 - \frac{1}{2}(l_0 - l_t)$ and $\psi' = \frac{\pi}{2} + \psi$. Here, R_0 denotes the undeformed radius of the ring. R_0 alternates between R_{max} and R_{min} depending on the location of the tracking tape. At the beginning of each experiment, the elastic ring on each ADS are manually rotated to approximately the $\psi = 0$ position, so that R_{max} is always the starting radius. Solving equations 26 and 27 gives us the value of ψ . We require that the tracking method is accurate up to $\pm 5^\circ$ in order to resolve cycles of maximum and minimum stiffness. Fig. S20E (top row) shows a snapshot of our tracking code, which obtains the location of the side post tapes (red circles) and ring tapes (blue circle) by thresholding each frame of the video in color space.

2. Side view tracking

While the top view videos give us ψ as a function of time, side view videos give us the relative phase between η and θ . The pendulum and various hinged points on the linkages and ratchet are labelled with tracking tape to assist with image tracking. We determine the location of the markers by thresholding each frame of the video in color space. The result of the thresholding procedure is shown in Fig. S20F where the tracked tape locations (colored circles) are overlaid on a frame of the video.

3. Validation of tracking code

In order to determine the validity of the approximations used to determine ψ from the top view, we conducted validation experiments where a single ADS is filmed from the top and side views. Both cameras used for both perspectives are triggered synchronously using a micro-controller. We imaged the side view of the ADS from the back facing side (the opposite side of the pendulum), so that by tracking two pieces of tracking tape placed diametrically opposite on the surface of the elastic ring, the true angle ψ can be used as a baseline to validate the top view tracking. Fig. S20Gi shows a snapshot of the tracked videos for $\psi = 325^\circ$ as viewed from the side and top views, while Fig. S20Gii shows snapshots for $\psi = 77^\circ$. Fig. S20H plots the raw data of the measured value of ψ from the top view (orange scatter points). We then apply a moving mean filter to the raw data in order to smooth over experimental measurement noise (due to slight changes in saturation and lighting of the tracking markers as the ADS oscillates). We choose a moving mean window of 30 frames, which corresponds to averaging over approximately 4 cycles of the active node's oscillations (3.6-4.4 cycles for the range of driving frequencies explored). We note that this is a reasonable window to average over since the update period of the elastic ring (ψ) is much slower than the period of the input oscillations. After smoothing ψ , we then take its value modulo 2π . Fig. S20I plots the post-processed ψ as measured from the top view (solid black line) with the values of ψ measured from the side view (blue scatter points). The side view measurements, excluding the intrinsic measurement noise, are an accurate representation of ψ since it is a direct measurement and no assumptions about the deformation of the elastic ring are needed. We observe good agreement between these two measurements which validates the procedure used to measure ψ from the top view. In the side view data, frames where the tracking tape passes behind the guide rails and are thus obscured are not plotted. The estimated accuracy of measuring ψ from the top view is approximately 3.4° based averaging the mean deviation of the measured values of ψ from the top view and side view.

4. Quality control of ADS

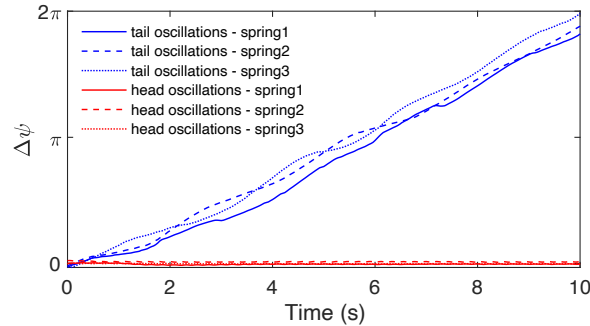


FIG. S21. **Comparison of update rate among different ADSs.** Three ADSs are oscillated at their heads and tails with driving parameters $A=6.7\text{mm}$, $f=3.7\text{Hz}$. All ADSs behave similarly.

To ensure that our manufacturing procedure doesn't produce significant differences in the update rate of an ADS, we conducted control experiments where we measured the update speed of three different springs oscillated individually at the same forcing parameters. Fig. S21 illustrates the measured results for both head and tail oscillations. Our results indicate that the update rate doesn't vary significantly across different springs during tail oscillations, and doesn't update for any of the springs during head oscillations.

B. Experimental parameters

1. Measuring $k(\psi)$

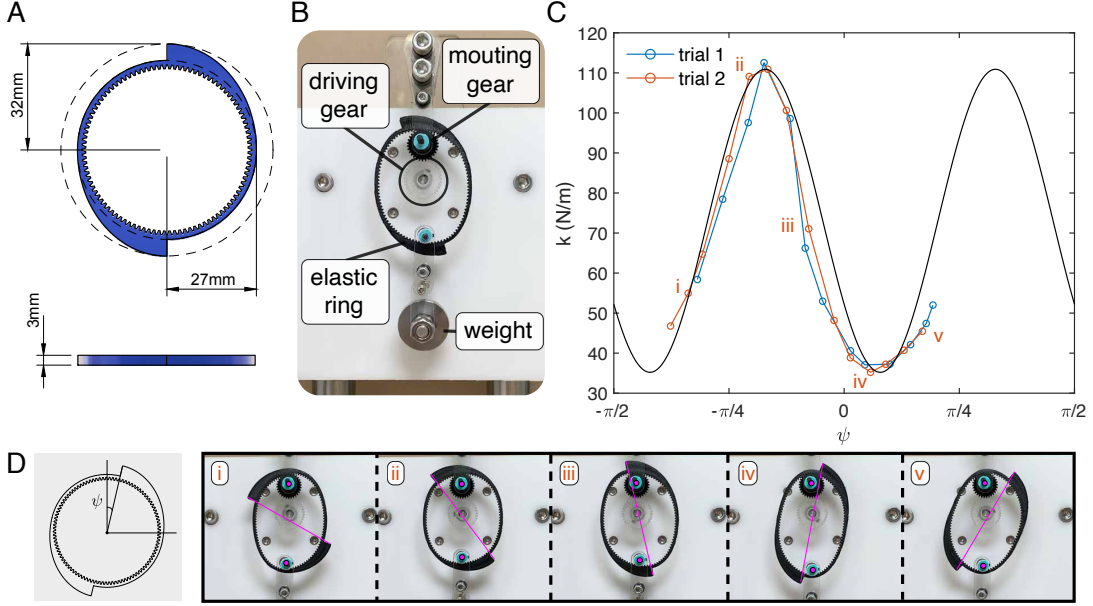


FIG. S22. **Spring stiffness measurement.** (A) Elastic ring dimensions and geometry. The geometry of the elastic ring was chosen to be one convenient for image tracking. (B) Experimental rig for measuring the spring constant of the elastic ring as a function of ψ by hanging weights and measuring the displacement of the ring. (C) Experimental data of the measured spring stiffness as a function of ψ . A least-squares fitted function is plotted (solid black line). (D) Snap shots of the measured angle (ψ) and extension of the ring.

In order to determine the stiffness as a function of ψ for the elastic ring (with thickness profile illustrated in Fig. S22A), an experimental setup shown in Fig. S22B was used to measure the extension of the elastic ring when stretched by a weight. The setup consists of a mounting gear used to suspend the elastic ring. A stepper motor driven ‘driving gear’ is coupled directly to the mounting gear in order to rotate the elastic ring by a constant, programmed angle. After each rotation, the weight is manually lifted and released at the vertical center-line of the elastic ring to ensure that the force exerted by the weight acts directly downwards along the center-line of the ring. By measuring the displacement, and assuming the force-displacement relationship to be approximately linear, we can calculate the spring constant since the mass of the suspended weight is known. Fig. S22C illustrates the experimental results for two trials, where the solid line is a fitted curve of the form

$$k(\psi) = \frac{k_{\min} - k_{\max}}{2}(1 - \cos(4\psi + \alpha_1)) + k_{\max}$$

where α_1 is a fitting parameter, and k_{\max} and k_{\min} are the maximum and minimum measured spring constants. A least squares regression gives $\alpha_1 = 2.1542$, $k_{\min} = 35.22$ N/m, and $k_{\max} = 110.9$ N/m. In experiments, we convert the measured value of ψ to k using this fitted function. Fig. S22D shows several snapshots of the elastic ring’s extension as a function of ψ for trial 2.

2. Damping on nodes

We assume that a linear drag force acts on a node as it slides on the substrate. To estimate the corresponding damping coefficient, we accelerate and release the weighted node (acrylic disk with mass 161g) and measured its deceleration as a function of time on the substrate (Fig. S23). Under sliding friction, the equation of motion of the node position, $x(t)$ is given by

$$m\ddot{x} = -b\dot{x} - \mu mg$$

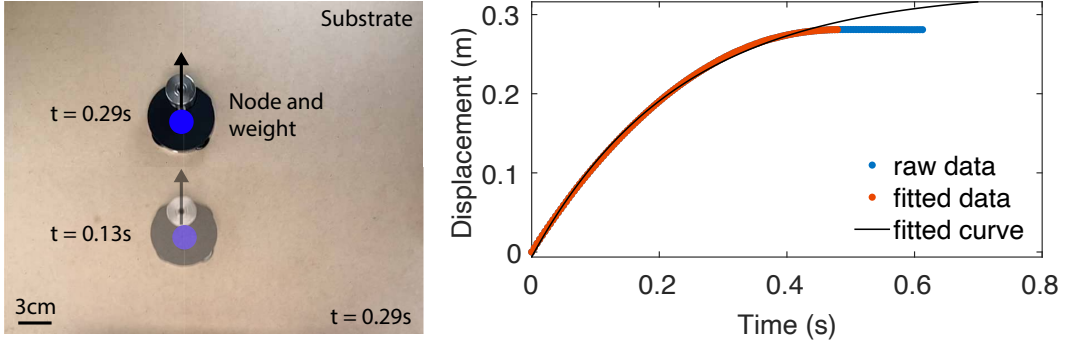


FIG. S23. **Measurement of damping on node.** Left: Experimental setup, a weighted passive node is launched across the substrate with initial velocity v_0 , and the deceleration as a function of time is measured. Right: The position of the passive node as a function of time, showing the raw data and the truncated data used for the fitted curve.

where g is gravity, μ is the coefficient of friction between the surface and the node, b is the damping coefficient, and m is the mass of the node. We assume the node has initial position $x(0) = 0$ and initial velocity $v_0 > 0$, so sliding friction acts in the negative direction. The velocity of the disk as a function of time is then

$$\dot{x}(t) = e^{-\frac{bt}{m}} \left(v_0 + \frac{\mu mg}{b} \right) - \frac{\mu mg}{b}$$

This solution is valid until $\dot{x}(t) = 0$. We truncate the raw data (blue) prior to the point at which the disk becomes stationary to remain in the sliding friction regime. Least squares regression is used to fit the data to a curve of the form $Ae^{-Bt} - C$ with the fitting parameters A, B, C . The damping coefficient is determined to be $b = 0.71$ kg/s.

3. Natural frequency and moment of inertia of pendulum

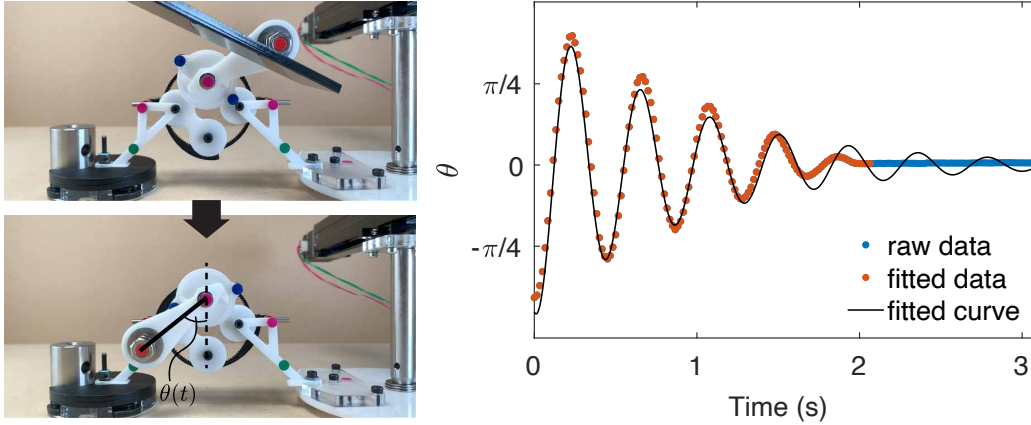


FIG. S24. **Measurement of the natural frequency and moment of inertia of the pendulum.** Left: Experimental setup of the ‘ring down’ experiment, where the pendulum is raised to an amplitude A_0 , and allowed undergo damped oscillations. Right: The measured value of θ , the pendulum’s angle, as a function of time. The raw data and the truncated data used for the fitted curve are shown.

We performed ‘ring down’ experiments on the damped pendulum mounted on the ADS in order to determine its natural frequency and moment of inertia (Fig. S24). We perturb the pendulum by raising it above its equilibrium position, and measuring its decaying oscillations using the tracking tape on the pendulum. The equation of motion for the pendulum is

$$\ddot{\theta} + b_p \dot{\theta} + \omega_p^2 \theta = 0$$

This equation has solution

$$\theta(t) = A_0 e^{-\frac{b_p}{2}t} \cos[\omega'_p(t - t_0)]$$

where A_0, t_0 are constants, and ω'_p is given by

$$\omega'_p = \sqrt{\omega_p^2 - \frac{b_p^2}{4}}$$

We can define an effective length, L_{eff} for pendulum, by $\omega_p^2 = g/L_{\text{eff}}$. We therefore have

$$\omega'_p = \sqrt{\frac{g}{L_{\text{eff}}} - \frac{b_p^2}{4}}$$

We truncate the raw data before the pendulum becomes completely static, and use least squares regression to fit a curve of the form $\theta(t) = Ae^{-Bt} \cos[C(t - D)]$, where we have assumed linear damping. Here, $A, B, C,$ and D are fitting parameters. We find

$$b_p = 2B = 2.1 \text{ s}^{-1}, \quad \omega'_p = C = 15 \text{ s}^{-1}, \quad \omega_p = \sqrt{\frac{g}{L_{\text{eff}}}} = 15 \text{ s}^{-1}, \quad L_{\text{eff}} = 4.5 \text{ cm}$$

to 2sf.

4. Friction coefficient between node and substrate

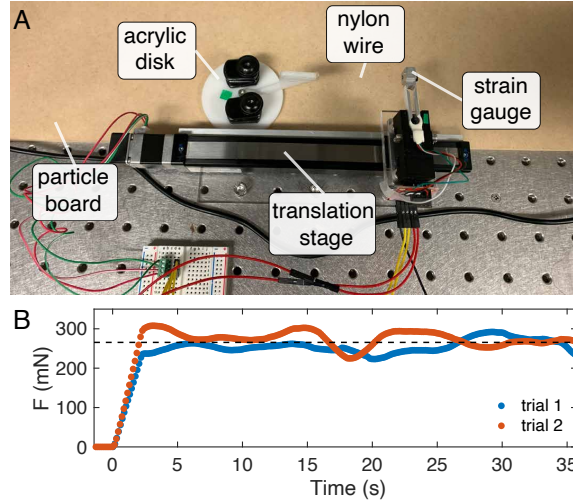


FIG. S25. **Measurement of friction coefficient.** (A) Friction measurement experimental setup consists of a translation stage pulling an acrylic disk with weight at a constant speed. (B) Experimental data of the measured force required to pull the acrylic disk at constant velocity.

In order to estimate the coefficient of friction between the nodes (acrylic disks) and the particle board substrate, we replicated the friction measurement setup from reference [8]. The setup (Fig. S25A) consists of a linear translation stage driven by a stepper motor. A strain gauge force sensor is mounted on the stepper motor, and an acrylic disk resting on the particle board substrate is tied to the strain gauge using a nylon string. Then, the linear translation stage begins moving with constant velocity, dragging the acrylic disk with an approximately constant force. The experimental data of the measured force as a function of time is plotted in Fig. S25B for two trials. In the start up phase (≈ 0 to 2 s), the force measured increases from zero to an approximately constant value as the nylon string becomes tensioned. We calculate the coefficient of friction by taking the mean force measured after the initial start up phase (> 5 s) over two trials, and dividing that value by the weight of the acrylic disk (including additional washers). The friction coefficient is measured to be 0.29 ± 0.02 , where the uncertainty is taken to be one standard deviation of the measured force over the two trials.

5. Learning rate estimate

The learning rate γ can be estimated by measuring the quantity $\dot{\psi}/\dot{\theta}$ over a period T where the elastic ring updates (equation 25). It can be shown that

$$\gamma = \frac{\psi(T_0 + T) - \psi(T_0)}{2Tf\theta_{\max}}$$

where f is the driving frequency and θ_{\max} is the amplitude of the pendulum's oscillation. Using the measured θ -dynamics from Fig. S18A and the measured ψ -dynamics from Fig. S13C, where the ADS is oscillated at its tail with driving amplitude $A = 6.7$ mm and frequency $f = 3.7$ Hz, we find $\gamma = 0.34$ over an interval of $T = 6$ s. Theoretically, γ should also be given by the gear ratio between the elastic ring and the top gear, because the ratchet is rigidly coupled to the top gear. Our measured value is close to this ideal value of $\frac{30 \text{ teeth}}{100 \text{ teeth}} = 0.3$, and is likely slightly different due to measurement error.

6. Parameters for each experiment

Figure	Driving Amplitude (mm)	Driving Frequency (Hz)	Mass of node (kg)	Floppy modes
2F	6.7	3.7	0.161	NA
2G	6.7	3.7	0.161	NA
2H	7.2	3.3	0.161	NA
3Ai	12	2.9	0.071	No
3Aii	9.2	3.3	0.154	Yes
3Aiii	9.2	3.3	0.154	Yes
3Aiv	9.6	3.3	0.154	Yes
S13B	6.7	3.7	0.161	NA
S13C	6.7	3.7	0.161	NA
S14	8.7	3.3	0.161	NA
S16	6.7	3.7	0.161	NA
S17	8.7	3.7	0.161	NA
S18A	6.7	3.7	0.161	NA
S18B	6.7	3.3	0.161	NA
S18C	6.7	2.9	0.161	NA
S18D	6.7	3.7	0.161	NA
S19G-I	6.7	3.7	0.161	NA
S20	6.7	3.7	0.161	NA

TABLE II. **Experimental parameters.**

IV. MECHANICAL CIRCUITS

In this section, we study the dynamics of ADS networks. We begin with the behavior of a single ADS, before deriving the equations of motion for ADS networks, and constructing flow diagrams to heuristically analyze their properties. We then consider applications of ADS networks.

A. Dynamics of a single ADS

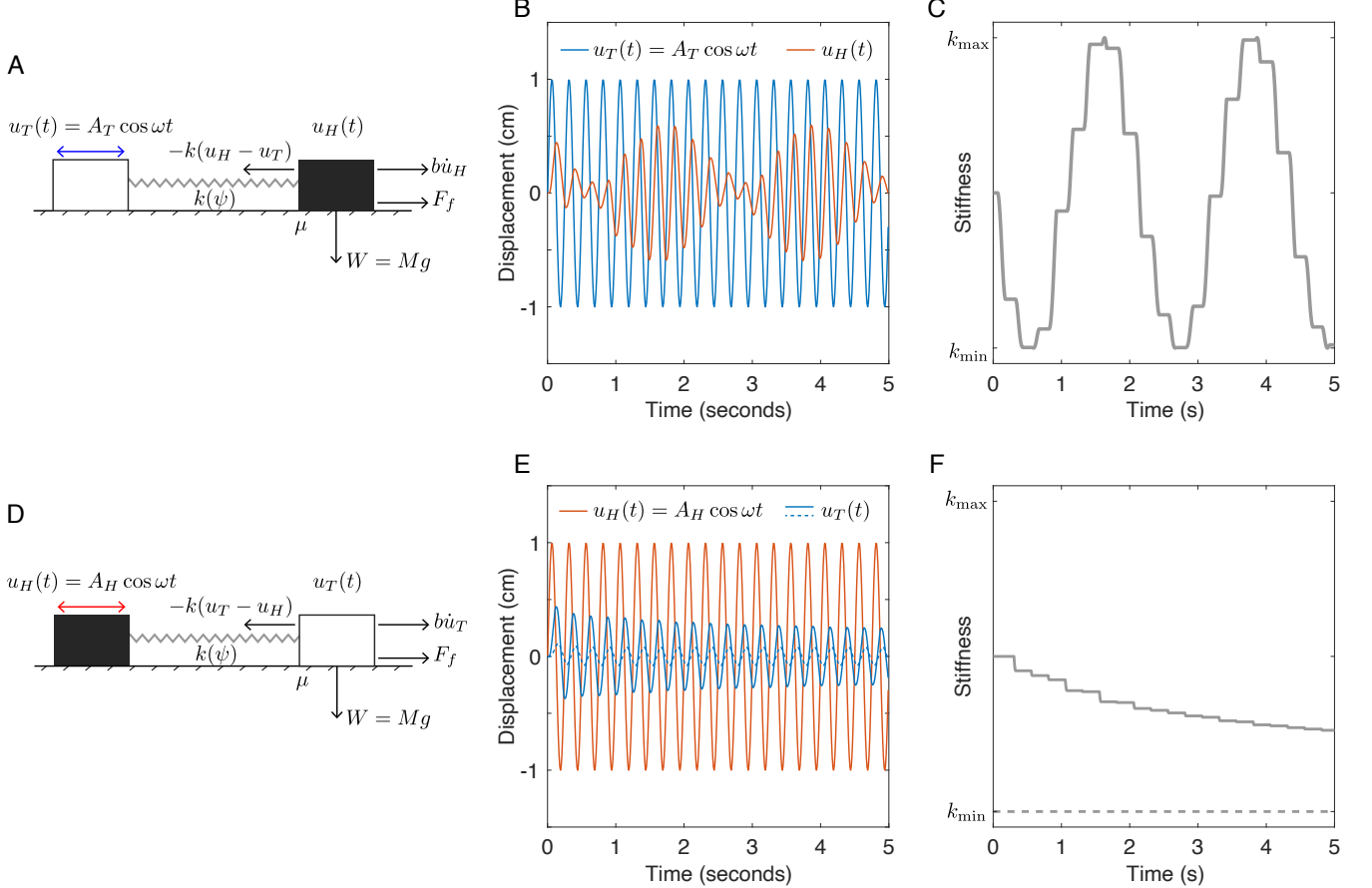


FIG. S26. **Dynamics of an ADS** (A-C) Behavior and update of an ADS in response to oscillation of the tail end (A). The tail is set to oscillate with frequency ω and amplitude A_T (B, blue curve). The oscillation amplitude of the head node, $u_H(t)$, varies (B, red curve) due to the spring changing stiffness (C). The maximum amplitude of $u_H(t)$ is less than A_T due to dissipative losses in the system. (D-F) Behavior and update of an ADS in response to oscillation of the head end (D). The head end oscillates at frequency ω (E, red curve). The response of the tail end (blue curves) is shown for two different initial values of spring stiffness: $k(0) = (k_{\max} + k_{\min})/2$ (solid blue curve) and $k(0) = k_{\min}$ (dashed blue curve). In both cases, the oscillation amplitude of the tail end stays approximately constant. Additionally, the spring stiffness stays approximately constant in both cases (F, solid and dashed grey curves), as expected for an ADS with larger head oscillation than tail oscillation. The small changes in stiffness are due to phase differences between u_T and u_H (see section IA 3).

Here we analyze the dynamics of a single ADS joining two nodes of mass M . We can simulate both the case where motion of the tail end is prescribed, and where the head motion is prescribed (Fig. S26). Under tail oscillations, the spring changes stiffness, and the oscillation amplitude of the free node varies (Fig. S26A-C). Under head oscillations, the free node oscillates at approximately constant amplitude, and the spring stiffness remains approximately constant (Fig. S26D-F).

We can explicitly write down the equations of motion for the dynamics in Fig. S26. For simplicity we will only write down the equations in the case where the tail is oscillated (Fig. S26A-C). These consist of equations for the

displacement u_H , the oscillators θ and η , the update rule for the elastic ring angle ψ , and the $k(\psi)$ relation determining spring stiffness

$$M\ddot{u}_H = -b\dot{u}_H - k(u_H - A_T \cos \omega t) + F_f(\dot{u}_H, F_0; \mu Mg) \quad (28a)$$

$$\begin{pmatrix} \ddot{\theta} + b_p \dot{\theta} + \omega_p^2 \theta \\ \ddot{\eta} \end{pmatrix} = \begin{pmatrix} -1 & 1 \\ -\frac{1}{2\ell_p} & -\frac{1}{2\ell_p} \end{pmatrix} \begin{pmatrix} u_T \\ u_H \end{pmatrix} \quad (28b)$$

$$\dot{\psi} = \gamma \text{Relu}(\dot{\theta} - \tau_0) \Theta(\dot{\eta} - \tau_1) \quad (28c)$$

$$k = k^0 - \Delta k \cos(4\psi + \alpha_0) \quad (28d)$$

where F_0 denotes the total non-friction force on u_H . The u_H equation is discussed in section IB 1, the oscillator equations are discussed in section IB 3, and the ψ and k equations are discussed in section IB 5.

The simulated u_T and u_H oscillations have a phase lag (Fig. S26B,E). This suggests that the simulation parameters used give rise to a highly non-ideal ADS (see section IA 3). Nevertheless, the simulations demonstrate that an ADS can still satisfy its axioms in this regime. In particular, tail oscillations lead to spring update, but head oscillations do not (Fig. S26). The fact that some slow update occurs under head oscillations here (Fig. S26F) is likely to be due to phase lag effects (see section IA 3).

We can identify the phase lag between u_T and u_H by approximating the ADS equations. Assuming the spring stiffness k is constant and complexifying, the u_H equation gives

$$M\ddot{u}_H = -b\dot{u}_H - k(u_H - A_T e^{i\omega t}) + F_f(\dot{u}_H, F_0; \mu Mg)$$

The equation of motion has terms for inertia, damping, elasticity and friction. This motivates the definition of the following dimensionless parameters

$$\rho = \frac{M\omega^2}{k} \quad \zeta = \frac{b}{M\omega} \quad \nu = \frac{\mu Mg}{kA_1} \quad (29)$$

In the weak friction case, when ν is small, we can look for solutions of the form $u_2(t) = A_2 e^{i\omega t}$. The equation becomes

$$-M\omega^2 A_2 = -b\omega A_2 i - k(A_2 - A_1)$$

We can solve for A_2 in terms of A_1

$$A_2 = \frac{kA_1}{k - M\omega^2 + b\omega i} = \left(\frac{1}{1 - \rho + \rho\zeta i} \right) A_1$$

The ADS simulations in Fig. S26 have

$$\rho = 1.6, \quad \zeta = 3.8, \quad \nu = 0.3$$

to 1 decimal place, where we have taken $k = k_{\min}$ in the definition of ρ and ν (equation 29). At these parameters, we therefore expect u_T and u_H to have a phase lag as seen in Fig. S26, since A_2/A_1 is complex.

B. Dynamics of ADS networks

An ADS network is a collection of N nodes joined by ADSs. Ignoring geometric information, such a network can be represented as a directed graph $G = (V, E)$. Labelling the nodes from 1 to N gives a vertex set $V = \{1, 2, \dots, N\}$. The edge set E consists of ordered pairs of vertices. The pair $e = (v, w)$ is in E if and only if there is an ADS joining nodes v and w , with the tail of the ADS at v and the head at w . Topological information is encoded in the incidence matrix, I_{ve} which establishes edge-vertex adjacency.

$$I_{ve} = \begin{cases} +1 & \text{if } e(1) = v \\ -1 & \text{if } e(2) = v \\ 0 & \text{otherwise} \end{cases}$$

For example, the network in Fig. S27 has edges

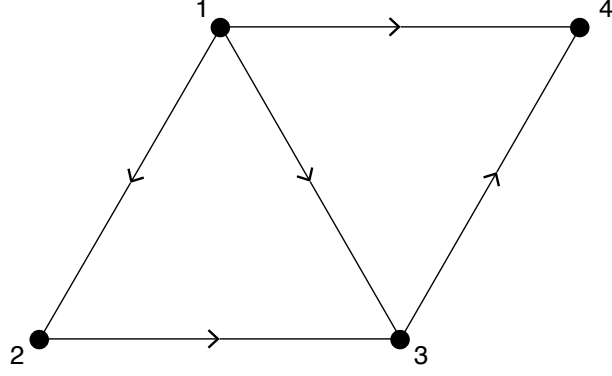


FIG. S27. A directed graph representing an ADS network.

$$e_1 = (1, 2), e_2 = (1, 3), e_3 = (1, 4), e_4 = (2, 3), e_5 = (3, 4)$$

The incidence matrix is

$$I = \begin{pmatrix} 1 & 1 & 1 & 0 & 0 \\ -1 & 0 & 0 & 1 & 0 \\ 0 & -1 & 0 & -1 & 1 \\ 0 & 0 & -1 & 0 & -1 \end{pmatrix}$$

To understand the dynamics of an ADS network with topology given by a graph G , we need to account for the geometric information of the network's embedding in the plane. Suppose the v 'th vertex has position $\mathbf{r}_v \in \mathbb{R}^2$. For $e \in E$, edge vectors are given by

$$\begin{aligned} \mathbf{b}_e &= \mathbf{r}_{e(2)} - \mathbf{r}_{e(1)} \\ \hat{\mathbf{b}}_e &= \frac{1}{|\mathbf{b}_e|} \mathbf{b}_e \end{aligned}$$

so $\hat{\mathbf{b}}_e$ is a unit vector in the direction of \mathbf{b}_e . The vector \mathbf{b}_e points from the tail to the head of the corresponding ADS. Energies follow from finding the extension of the edges under small displacements $\mathbf{r}_v \mapsto \mathbf{r}_v + \mathbf{u}_v$. To leading order in \mathbf{u} we find extension, η_e given by

$$\begin{aligned} \eta_e &= |\mathbf{r}_{e(2)} - \mathbf{r}_{e(1)} + \mathbf{u}_{e(2)} - \mathbf{u}_{e(1)}| - |\mathbf{b}_e| \\ &= (\mathbf{u}_{e(2)} - \mathbf{u}_{e(1)}) \cdot \hat{\mathbf{b}}_e \\ &= - \sum_v I_{ve} \hat{\mathbf{b}}_e \cdot \mathbf{u}_v \end{aligned}$$

In our ADS networks, each edge also has a pendulum with angle θ which satisfies

$$\ddot{\theta}_e + b_p \dot{\theta}_e + \omega_p^2 \theta_e = -\frac{1}{2\ell_p} \sum_v |I_{ve}| \hat{\mathbf{b}}_e \cdot \mathbf{u}_v$$

as in equation (24). We can define geometric incidence matrices Q and Q' as follows

$$Q_{ve} = \begin{cases} +\hat{\mathbf{b}}_e & \text{if } e(1) = v \\ -\hat{\mathbf{b}}_e & \text{if } e(2) = v \\ 0 & \text{otherwise} \end{cases} \quad Q'_{ve} = \begin{cases} \hat{\mathbf{b}}_e & \text{if } e(1) = v \\ \hat{\mathbf{b}}_e & \text{if } e(2) = v \\ 0 & \text{otherwise} \end{cases}$$

so that

$$\eta_e = -Q_{ve} \mathbf{u}_v \tag{30a}$$

$$\ddot{\theta}_e + b_p \dot{\theta}_e + \omega_p^2 \theta_e = -\frac{1}{2\ell_p} Q'_{ve} \ddot{\mathbf{u}}_v \tag{30b}$$

Let k_e be the stiffness of edge e , and $K = \text{diag}(k)$. The elastic energy of the network is then

$$\begin{aligned}\mathcal{E} &= \frac{1}{2} \sum_e k_e \eta_e^2 = \frac{1}{2} \mathbf{u}^T Q K Q^T \mathbf{u} \\ &= \frac{1}{2} \sum_{v, v', e} k_e I_{ve} I_{v'e} (\hat{\mathbf{b}}_e \cdot \mathbf{u}_v) (\hat{\mathbf{b}}_e \cdot \mathbf{u}_{v'})\end{aligned}$$

where for notational convenience, we have used \mathbf{u} to refer to the $2|V| \times 1$ column vector obtain by stacking $\mathbf{u}_1, \mathbf{u}_2, \dots$. The force on the v 'th vertex can be written

$$\mathbf{F}_v = - \sum_{v', e} k_e I_{ve} I_{v'e} (\hat{\mathbf{b}}_e \cdot \mathbf{u}_{v'}) \hat{\mathbf{b}}_e \quad (31a)$$

$$\mathbf{F} = -Q K Q^T \mathbf{u} \quad (31b)$$

Here, \mathbf{F} is a stacked $2|V| \times 1$ column vector, like \mathbf{u} .

1. Classical elastic networks

Using the above expression for force, we can write down the equations of motion for a classical elastic network. We assume that the mass M and viscous damping parameter b are the same for each node. The equations of motion are then

$$M \ddot{\mathbf{u}} + b \dot{\mathbf{u}} = -Q K Q^T \mathbf{u} \quad (32)$$

2. ADS networks

To write down the equations of motion for the ADS network, we must also include the friction equation and the stiffness update equation introduced earlier. Recall the friction equation (16)

$$\mathbf{F}_f(\mathbf{v}, \mathbf{F}_0; \mu M g) = \begin{cases} -\mu M g \hat{\mathbf{v}} & \text{if } |\mathbf{v}| > 0 \\ -\min(\mu M g, |\mathbf{F}_0|) \hat{\mathbf{F}}_0 & \text{if } |\mathbf{v}| = 0 \end{cases}$$

where μ is the coefficient of friction, and g is gravitational acceleration. The expression for \mathbf{F}_f can be extended to allow for stacked vectors \mathbf{u}, \mathbf{F}_0 with $2|V|$ entries by setting

$$\left[\mathbf{F}_f(\mathbf{u}, \mathbf{F}_0; \mu M g) \right]_v = \mathbf{F}_f(\mathbf{u}_v, (\mathbf{F}_0)_v; \mu M g)$$

for each node v . We further require the spring stiffness update equation (25)

$$\begin{aligned}k_e &= k^0 - \Delta k \cos(4\psi_e + \alpha_0) \\ \dot{\psi}_e &= \gamma \text{Relu}(\dot{\theta}_e - \tau_0) \Theta(\dot{\eta}_e - \tau_1)\end{aligned}$$

where $\gamma > 0$ is the learning rate, α_0 is an offset and τ_0 and τ_1 are thresholds.

Putting all of the above equations together, we can write down the full equations of an ADS network

$$M \ddot{\mathbf{u}} = \mathbf{F}_0 + \mathbf{F}_f(\dot{\mathbf{u}}, \mathbf{F}_0; \mu M g) \quad (33a)$$

$$\mathbf{F}_0 = -b \dot{\mathbf{u}} - Q K Q^T \mathbf{u} \quad (33b)$$

$$\boldsymbol{\eta} = -Q \mathbf{u} \quad (33c)$$

$$\ddot{\boldsymbol{\theta}} + b_p \dot{\boldsymbol{\theta}} + \omega_p^2 \boldsymbol{\theta} = -\frac{1}{2\ell_p} Q' \ddot{\mathbf{u}} \quad (33d)$$

$$k_e = k^0 - \Delta k \cos(4\psi_e + \alpha_0) \quad (33e)$$

$$\dot{\psi}_e = \gamma \text{Relu}(\dot{\theta}_e - \tau_0) \Theta(\dot{\eta}_e - \tau_1) \quad (33f)$$

3. Small viscous damping

We will also frequently assume that we can drop the $b\dot{\mathbf{u}}$, $b_p\dot{\theta}$ terms. This amounts to assuming

$$\frac{b}{M\omega^2}, \frac{b_p}{\omega} \ll 1$$

where ω is the characteristic oscillation frequency of the nodes in the network. Under these assumptions, the equations of motion can be simplified

$$\begin{aligned} M\ddot{\mathbf{u}} &= -QKQ^\top \mathbf{u} + \mathbf{F}_f(\dot{\mathbf{u}}, -QKQ^\top \mathbf{u}; \mu Mg) \\ \begin{pmatrix} \ddot{\boldsymbol{\eta}} \\ 2\ell_p(\ddot{\boldsymbol{\theta}} + \omega_p^2\boldsymbol{\theta}) \end{pmatrix} &= -\begin{pmatrix} Q \\ Q' \end{pmatrix} \ddot{\mathbf{u}} \\ k_e &= k^0 - \Delta k \cos(4\psi_e + \alpha_0) \\ \dot{\psi}_e &= \gamma \text{Relu}(\dot{\theta}_e - \tau_0) \Theta(\dot{\eta}_e - \tau_1) \end{aligned}$$

where $\boldsymbol{\eta}$, $\boldsymbol{\theta}$ are stacked vectors with $|E|$ entries, where $|E|$ is the number of edges (i.e. ADSs) in the network. Assuming that the system has a dominant frequency, ω , we can approximately write $\ddot{\boldsymbol{\theta}} = -\omega^2\boldsymbol{\theta}$, in which case the oscillator equations for $\boldsymbol{\eta}$, $\boldsymbol{\theta}$ can be written

$$\begin{pmatrix} \ddot{\boldsymbol{\eta}} \\ 2\ell_p\left(1 - \frac{\omega_p^2}{\omega^2}\right)\ddot{\boldsymbol{\theta}} \end{pmatrix} = -\begin{pmatrix} Q \\ Q' \end{pmatrix}$$

This form of the oscillator equations shows that the sign of the coefficient of $\boldsymbol{\theta}$ depends on the magnitude of ω_p/ω . We work at driving frequencies where $\omega_p/\omega < 1$, so the coefficient of $\boldsymbol{\theta}$ is positive. As discussed in equation (23), the orientation of an ADS can be flipped by decreasing ω so that $\omega_p/\omega > 1$.

4. Fixed points

We define quasi-stable fixed points of the stiffness update dynamics to be configurations for which the spring stiffnesses either update slowly or remain fixed, i.e. $\dot{k}_e \approx 0$ for all edges. These can occur when head oscillations within an ADS network produce a sufficiently large self-regulation effect. We can write this condition more precisely. We assume that the displacement profile in such a state is single frequency oscillation, with

$$\mathbf{u}_v = \mathbf{A}_v \cos \omega t$$

The condition that the springs remain fixed, or update slowly, is equivalent to requiring the head oscillation amplitudes to be large. Using the ADS axioms (equation 3), we can write this condition as

$$\mathbf{A}_{e(1)} \cdot \hat{\mathbf{b}}_e < \mathbf{A}_{e(2)} \cdot \hat{\mathbf{b}}_e + \delta$$

where δ is the threshold in equation (3), and \mathbf{A} is a stacked vector with $2|V|$ entries. This condition can be written more compactly using the geometric incidence matrix Q

$$(Q^\top \mathbf{A})_e < \delta$$

for each edge e .

C. Small mechanical circuits

To build intuition for the behavior of ADS networks, we analyze small mechanical circuits (Fig. S28). Due to the large combinatorial space of oriented graphs (main text Fig. 3), there are many such small circuits, with a broad range of learning behaviors. We analyse these by first constructing flow diagrams, and then using these to understand information propagation through a network.

1. Flow diagrams

Consider a mechanical circuit in which a set of input nodes are externally forced (Fig. S28, white nodes). These external forces represent environmental forces. The flow diagram is a tool for understanding how ADSs throughout the network will update. These diagrams depend only on circuit topology, and so can be constructed in terms of a directed graph $G = (V, E)$. As above, the vertex set V is the set of nodes of the mechanical circuit, and the edge set $E \subset V \times V$ is the set ADSs in the circuit. An edge $e = (v, w)$ is in E if and only if the mechanical circuit has an ADS with tail at node $e(1) = v$ and head at node $e(2) = w$. To construct a flow diagram, we further need a subset of vertices, $V_0 \subset V$, corresponding to the input nodes of the mechanical circuit. In the examples of Fig. S28, V_0 has a single element.

The flow diagram depicts oriented paths which start in V_0 in terms of edges. We define an oriented path as a sequence of adjacent edges which all point in the same direction along the path:

$$e_1, e_2, \dots, e_m \subset E \quad \text{s.t.} \quad e_i(2) = e_{i+1}(1)$$

We say that an edge e has distance d from V_0 if d is the length of the shortest oriented path (e_1, e_2, \dots, e) such that $e_1(1) \in V_0$. In other words, the distance is the length of the shortest oriented path which starts in V_0 and ends with e . Using these notions, the flow diagram can be constructed. The 0'th layer of the flow diagram consists of the vertices in V_0 (Fig. S28, white circles). The i 'th layer of the flow diagram consists of all edges distance i from V_0 (Fig. S28, colored circles). The depth of the diagram is the distance of the furthest edge from V_0 . To complete the flow diagram construction, we need rules for drawing interaction lines between edges in different layers. These lines capture how the corresponding ADSs in the mechanical circuit interact with each other.

To begin with, for every oriented path (e_1, e_2, \dots, e_m) starting in V_0 (i.e. $e_1(1) \in V_0$), we draw interaction lines between the circles representing e_i and e_{i+1} in the flow diagram, for $i = 1, 2, \dots, m - 1$. Furthermore, this line has an arrow pointing to e_{i+1} , and an inhibitor next to e_i . This represents the fact that e_i meets e_{i+1} at its tail, and so e_i promotes the update of e_{i+1} . On the other hand, e_{i+1} meets e_i at its head, and so e_{i+1} inhibits the update of e_i . All interaction lines within a flow diagram are drawn in this manner, so each end of every line is either an arrow or an inhibitor (Fig. S28).

The final set of interaction lines in a flow diagram arise when two paths intersect, or when a single path intersects itself. More precisely, this scenario occurs when two distinct oriented path segments, (e_1, e_2) and (e_3, e_4) , intersect at a vertex:

$$e_1(2) = e_2(1) = e_3(2) = e_4(1)$$

In other words, the vertex between e_1 and e_2 is the same as the vertex between e_3 and e_4 . Note that (e_1, e_2) and (e_3, e_4) could belong to different paths emanating from V_0 , or could represent a self-intersection in the same path as traced from V_0 . By construction, we know that $e_1 \neq e_2$, $e_3 \neq e_4$ and $(e_1, e_2) \neq (e_3, e_4)$. This leaves us with 3 cases: $e_2 = e_4$ (merging paths), $e_1 = e_3$ (branching paths) or e_1, e_2, e_3, e_4 all distinct (crossing paths). All three of these cases occur in several of the networks shown in Fig. S28. For example merging paths occur in row 2, column 2; branching paths occur in row 3, column 1; crossing paths occur row 4, column 2. For all such path intersections, the flow diagram additionally contains all interaction lines between e_1, e_2, e_3, e_4 (Fig. S28).

2. Circuit dynamics

The flow diagrams allow us to rationalize the k -dynamics of a mechanical circuit. In Fig. S28, the white node of each mechanical circuit is oscillated horizontally with prescribed displacement. ADSs at larger depth in the flow diagram are further away from the input forcing at the white nodes, and therefore typically update more slowly (e.g. Fig. S28, bottom row). Similarly, ADSs which experience more inhibitory interactions in the flow diagrams typically update more slowly. For example, the red ADS in Fig. S28, row 1, column 2 is inhibited by the yellow ADS and so doesn't update, whereas the red ADS in Fig. S28, row 3, column 1, does update because it is not inhibited. The network in Fig. S28, row 4, column 3, contains a similar example within the same network, where the red and green ADSs are the same depth but the red ADS updates more slowly due the inhibitor from the yellow ADS.

Certain features of mechanical circuit dynamics are not captured by flow diagrams. For example, geometric degrees of freedom also mediate the learning dynamics. In Fig. S28, row 3, column 2, the blue ADS and the yellow ADS are initially almost perpendicular. As a result the blue ADS only causes the yellow ADS to update very slowly, because the force projected along the yellow ADS is very small. In general, shape changes within circuits with floppy modes

can affect the overall learning rates of the ADSs (Fig. S28, row 2, column 3). In certain cases, loops also create effects which are surprising when viewed from the perspective of the flow diagram. For example, in Fig. S28, row 4, column 1, the green spring updates, albeit slowly, despite the fact that it is attached to the forcing node (white) at its head. This is because the circuit contains several paths which join the white forcing node to the tail of the green ADS. These loops cause sufficient force to be transmitted to the tail end of the green ADS, ultimately resulting in update.

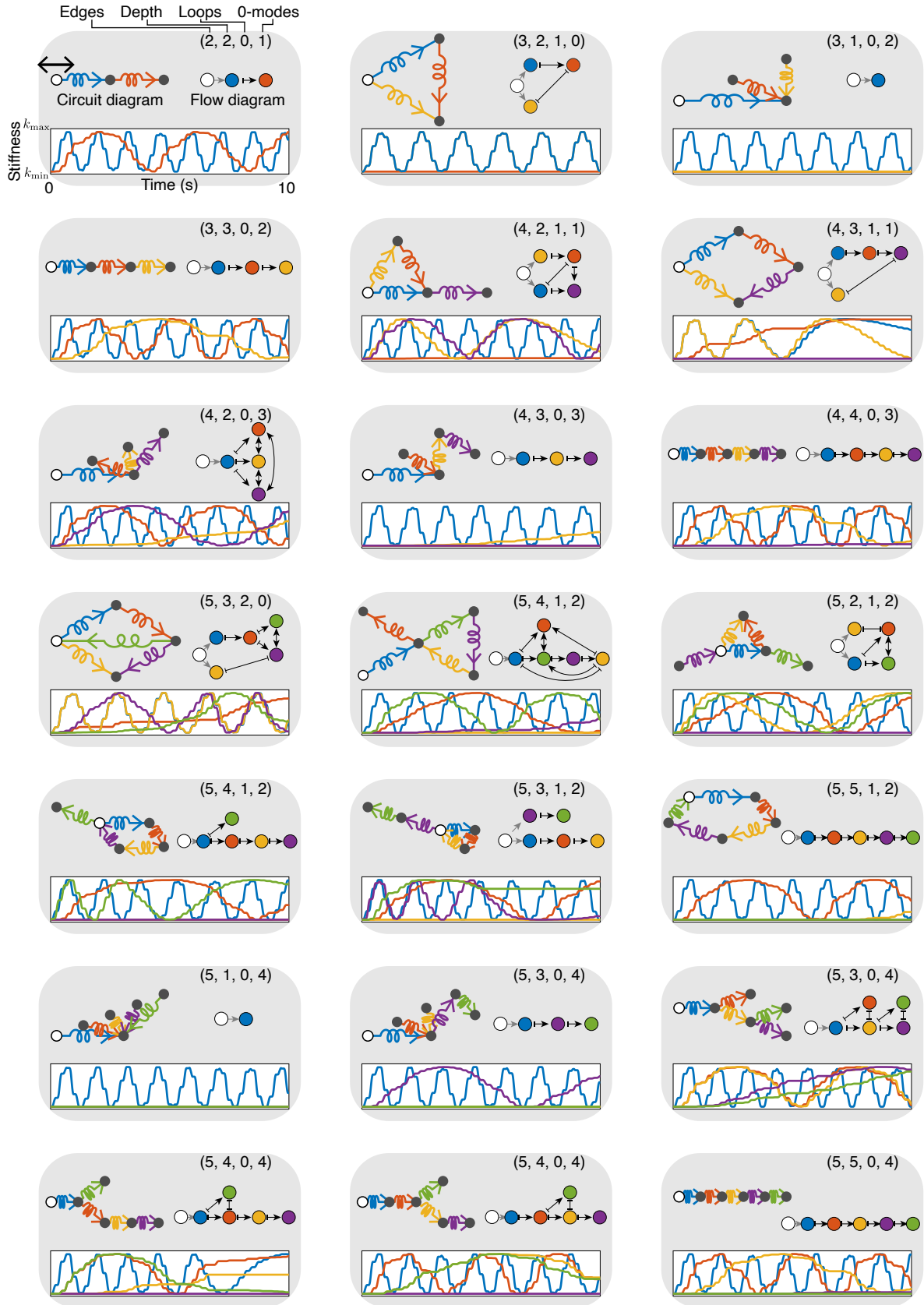


FIG. S28. **Learning dynamics in small mechanical circuits.** Different mechanical circuits (top left of each grey box) are excited by horizontal oscillations of the white nodes. In each case, the displacement of the white node is prescribed. The stiffness dynamics (bottom of each grey box) can be heuristically rationalized using the flow diagrams (top right of each grey box).

D. Applications

In this section we examine how functional behavior can arise from mechanical circuits. By setting up a specific statistical estimation task, we demonstrate that even a small network can learn patterns from environmental inputs. We then identify an adaptive damping behavior that arises in large networks of randomly oriented ADSs.

1. Pattern finding

Learning rules similar to the form of equation (33) are able to solve the streaming PCA problem [9]. Motivated by this, here we show how simple mechanical circuits can be applied to similar tasks. In general, a streaming problem consists of inputs received one at a time from a distribution, and the goal is to output a parameter of the distribution. For example, in the streaming PCA problem, the inputs are vectors drawn from a distribution, and the goal is to find the direction of maximum variance in the distribution. Streaming problems can be thought of as abstractions of the environmental learning problem for a smart material. In this analogy, the environment is a probability distribution, and the streaming input represents the network taking sequential measurements of the environment. Learning occurs when a particular attribute of the mechanical circuit reaches a steady state, from which a feature of the environmental distribution can be read. Continual learning occurs when the mechanical circuit can learn parameters of an environmental distribution even as the distribution changes.

More concretely, we consider the following streaming problem, which is a simplification of the streaming PCA problem. We assume the mechanical circuit receives sequential inputs, $\mathbf{A}^1, \mathbf{A}^2, \dots, \mathbf{A}^N$ which are independent and identically distributed random variables in \mathbb{R}^3 with mean zero. The first principle component of the distribution of \mathbf{A} is a unit vector \mathbf{v} along which the distribution has maximum variance. The goal is for the network to output the order of the components, $|v_1|, |v_2|, |v_3|$, which we assume are all distinct (Fig. S29A). In other words, the goal is to find the permutation P such that

$$|v_{P(1)}| > |v_{P(2)}| > |v_{P(3)}| \quad (34)$$

where $P \in S_3$, the symmetric group of order 3 (S_3 contains all permutations of 3 objects, so $|S_3| = 6$). We note that, from its definition as the direction of maximum variance, the first principal component, \mathbf{v} satisfies

$$\mathbb{E}[(\mathbf{A} \cdot \mathbf{v})^2] = \max_{|\mathbf{w}|=1} \mathbb{E}[(\mathbf{A} \cdot \mathbf{w})^2]$$

This is equal to the top eigenvector of the covariance matrix, $\Sigma = \mathbb{E}[\mathbf{A}\mathbf{A}^\top]$, by the following argument

$$\max_{|\mathbf{w}|=1} \mathbb{E}[(\mathbf{A} \cdot \mathbf{w})^2] = \max_{|\mathbf{w}|=1} \mathbb{E}[\mathbf{w}^\top \mathbf{A}\mathbf{A}^\top \mathbf{w}] = \max_{|\mathbf{w}|=1} \mathbf{w}^\top \Sigma \mathbf{w}$$

Succinctly, we can state the problem as follows: Given a sequence of i.i.d. random variables $\mathbf{A}^1, \dots, \mathbf{A}^N \in \mathbb{R}^3$, we want to find the permutation $P \in S_3$ such that the top eigenvector \mathbf{v} of the covariance matrix $\mathbb{E}[\mathbf{A}\mathbf{A}^\top]$ satisfies $|v_{P(1)}| > |v_{P(2)}| > |v_{P(3)}|$ (Fig. S29A). Memory is a key feature of this problem. A zero-memory estimator would have to estimate P based only off a single observation \mathbf{A}^i . As a benchmark, we can therefore define a zero-memory estimate, P_0 , defined to be the permutation which orders \mathbf{A}^N

$$|A_{P_0(1)}^N| > |A_{P_0(2)}^N| > |A_{P_0(3)}^N| \quad (35)$$

In order to use a mechanical circuit to solve the task described above, we need to specify how a network receives inputs and produces outputs. We additionally need to specify how the distribution \mathbf{A} is chosen.

Mechanical circuit inputs

We input the random variables \mathbf{A}^i into a circuit by constructing a network (Fig. S29B,C) which has 3 input nodes corresponding to the 3 components of \mathbf{A}^i . For $\alpha = 1, 2, 3$, the α 'th input node of the mechanical circuit is oscillated in the horizontal direction with varying amplitude. The horizontal displacement, $u_\alpha(t)$ of the α 'th input node at time $t > 0$ is given by

$$u_\alpha(t) = A_\alpha^{\lceil \frac{t}{\Delta T} \rceil} \cos \omega t \quad (36)$$

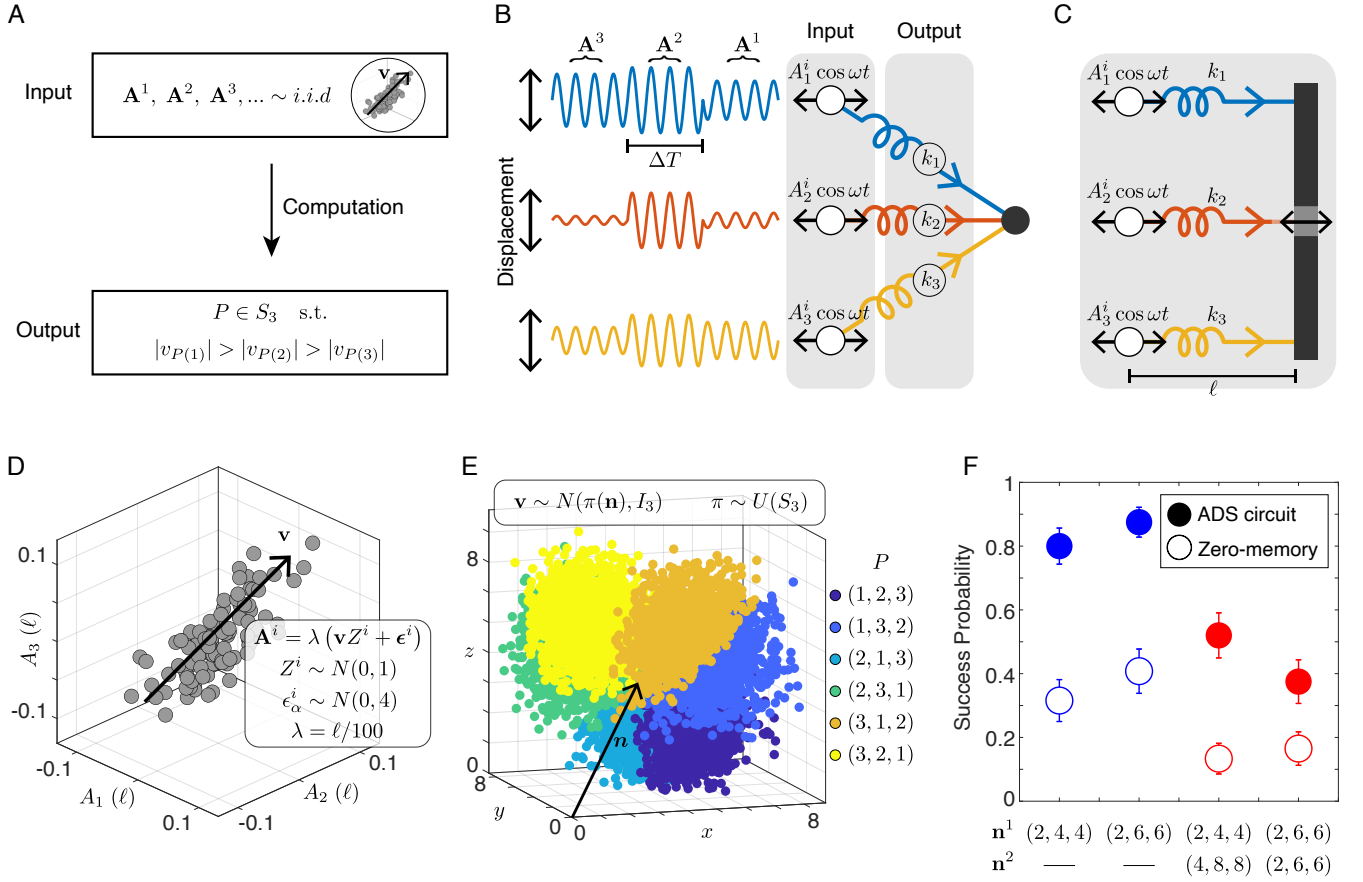


FIG. S29. **Pattern finding with small mechanical circuits** (A) Sketch of learning task. The inputs are a sequence of i.i.d. random variables, \mathbf{A}^i , whose distribution has first principal component \mathbf{v} , the top eigenvector of the covariance matrix $\mathbb{E}[\mathbf{A}\mathbf{A}^T]$. The goal is to find the ordering of the components $|v_i|$ of the eigenvector \mathbf{v} . Concretely, we seek to estimate the permutation P such that $i > j \Leftrightarrow |v_{P(i)}| > |v_{P(j)}|$ (equation 34). (B) To estimate P using a mechanical circuit (represented topologically), we input the vectors \mathbf{A}^i by oscillating the input nodes (white) at amplitude A_α^i , for $\alpha = 1, 2, 3$ (equation 36). Every time interval ΔT , the oscillation amplitude changes. The output of the circuit is the spring stiffnesses (k_1, k_2, k_3) at time $N\Delta T$, i.e. when the network has received N inputs. The estimator of the permutation P is the permutation P' which orders the spring stiffnesses, so $k_{P'(1)} > k_{P'(2)} > k_{P'(3)}$ (equation 37). (C) We implement the mechanical circuit in the depicted geometry, where all oscillations are horizontal and the ADSs are parallel and have length ℓ . The circuit in (B) is a topological representation of this network. (D) The inputs \mathbf{A}^i are drawn from a multivariate normal distribution with principal direction \mathbf{v} . In particular, $\mathbf{A}^i = \lambda(\mathbf{v}Z^i + \boldsymbol{\epsilon}^i)$ where Z and $\boldsymbol{\epsilon}$ are normally distributed and λ , which has dimensions of length, is given in terms of the ADS length ℓ . (E,F) To test the ability of the network to solve the learning task, we choose the direction \mathbf{v} at random, generate the sample $(\mathbf{A}^1, \dots, \mathbf{A}^N)$ from the distribution shown in (D), and input it into the mechanical circuit in (C). The direction \mathbf{v} is chosen from a multivariate normal distribution with mean $\boldsymbol{\pi}(\mathbf{n})$ and covariance matrix I_3 , where $\mathbf{n} \in \mathbb{R}^3$, $\boldsymbol{\pi}$ is a randomly chosen permutation which acts on the 3 components of \mathbf{n} , and I_3 is the 3×3 identity matrix (equation 39). As a result, the permutation P , which orders the components of the direction vector \mathbf{v} , can take any value with equal probability (colors). (F) Performance of a mechanical circuit (filled circles) and a naive zero-memory estimator (empty circles) described in equation (35) on the learning task. We choose a direction \mathbf{v}^1 from a distribution depending on \mathbf{n}^1 (equation 39), generate the sequence \mathbf{A}^i (equation 38), and obtain an estimate for the permutation P^1 , using the mechanical circuit. P^1 orders the components of \mathbf{v}^1 as in equation (34). The spring stiffnesses are set to $k_\alpha = k_{\min}$ at time 0. We then choose a second direction \mathbf{v}^2 from a distribution depending on \mathbf{n}^2 , and generate a new sequence $\tilde{\mathbf{A}}^i$. This new amplitude sequence is fed into the mechanical circuit without resetting it, to produce an estimate for the new permutation P^2 , which orders the components of \mathbf{v}^2 . Blue filled circles show the probability that the mechanical circuit correctly identifies the first permutation, P^1 ; red filled circles show the probability that the circuit correctly identifies both permutations P^1 and P^2 . In both cases, the circuit performs at least twice as well as the zero-memory estimator. Probabilities are obtained from 200 repetitions; error bars show 95% confidence intervals for success probability.

where ω is a fixed frequency and ΔT is the time interval between the network receiving the input \mathbf{A}^i and the input \mathbf{A}^{i+1} . The mechanical circuit thus receives a new oscillation amplitude every ΔT time interval. The number of

oscillation cycles input before the amplitude changes, n_c is given by

$$n_c = \frac{\omega}{2\pi\Delta T}$$

To obtain the data in Fig. S29, we have set $n_c = 4$. Typically, for learning to occur, we need the network to experience at least a few complete cycles of a particular amplitude, before switching to the next input.

Mechanical circuit outputs

For outputs, we examine the internal state of the network, which is determined by its spring stiffnesses. After time $N\Delta T$, the network has received N inputs, $\mathbf{A}^1, \dots, \mathbf{A}^N$. The final state of the spring stiffnesses is $k_\alpha(N\Delta T)$, for $\alpha = 1, 2, 3$. We can use the stiffness state to obtain a permutation, $P' \in S_3$, defined by

$$k_{P'(1)}(N\Delta T) > k_{P'(2)}(N\Delta T) > k_{P'(3)}(N\Delta T) \quad (37)$$

In Fig. S29, we have set $N = 100$. If $P' = P$, the network has completed the task, and thus learned a feature of the distribution of \mathbf{A} . We will compare the accuracy of P' to that of the zero-memory estimator P_0 defined in equation (35).

Choosing the distribution of \mathbf{A}

We apply a mechanical circuit to the above problem by choosing a family of distributions for \mathbf{A} (Fig. S29D). We do this by first choosing a direction $\mathbf{v} \in \mathbb{R}^3$ and then constructing the distribution for \mathbf{A} in such a way that its maximum variance direction is \mathbf{v} . We can then vary the distribution of \mathbf{A} by varying \mathbf{v} ; we therefore also specify how \mathbf{v} is chosen.

Given $\mathbf{v} \in \mathbb{R}^3$, we construct \mathbf{A}^i as follows. Let Z^i be a sequence of independent standard normals, so $Z_i \sim N(0, 1)$. Further, for $\alpha = 1, 2, 3$ let $\epsilon_\alpha^i \sim N(0, \sigma_\epsilon^2)$ be such that the random variables Z^i, ϵ_α^j are mutually independent for all i, j, α . Here, we have chosen $\sigma_\epsilon = 2$ (Fig. S29D). We then define \mathbf{A}^i as

$$\mathbf{A}^i = \lambda (\mathbf{v}Z^i + \boldsymbol{\epsilon}) \quad (38)$$

where $\lambda = \ell/100$ and ℓ is the length of an ADS in the mechanical circuit (Fig. S29C). The covariance matrix is therefore

$$\mathbb{E}[\mathbf{A}\mathbf{A}^\top] = \lambda^2 (\mathbf{v}\mathbf{v}^\top + 4I)$$

As required, the top eigenvector of this matrix is parallel to \mathbf{v} , with eigenvalue $\lambda^2(v^2 + 4)$ (the remaining 2 eigenvectors satisfy $\mathbf{v}^\top \mathbf{w} = 0$, and have eigenvalue $4\lambda^2$).

We can test the performance of the mechanical circuit on this task for a variety of different distributions of \mathbf{A} by varying \mathbf{v} . Accordingly, we choose \mathbf{v} from a distribution as follows (Fig. S29E)

$$\mathbf{v} \sim N(\pi(\mathbf{n}), I_3), \quad \pi \sim U(S_3) \quad (39)$$

Here $\mathbf{n} = (n_1, n_2, n_3) \in \mathbb{R}^3$ is fixed, π is a permutation which permutes the components n_1, n_2, n_3 , and the covariance matrix I_3 is the 3×3 identity matrix. π is chosen uniformly at random from S_3 . Note that the permutation P which gives the ordering of the components $|v_\alpha|$ (defined in equation 34) is not in general equal to π .

Learning using a mechanical circuit

We can now describe the procedure for testing the ability of the mechanical circuit to recover information about a distribution. We begin by initializing the mechanical circuit so that it is in its softest state $k_1, k_2, k_3 = k_{\min}$. We then input oscillation amplitudes from a first distribution, followed by amplitudes from a second distribution, without resetting the state of the mechanical circuit in between. This tests the ability of the mechanical circuit to learn from different initial internal states. Since we use two different distributions, there are two different permutations, P^1 and P^2 to estimate. The procedure is as follows:

1. Choose a fixed vector $\mathbf{n}^1 \in \mathbf{R}^3$ and choose \mathbf{v}^1 from the distribution $N(\pi(\mathbf{n}^1), I_3)$ (equation 39). The permutation P^1 orders the components $|v_1^1|, |v_2^1|, |v_3^1|$ (equation 34).

2. Generate a sequence $(\mathbf{A}^1, \dots, \mathbf{A}^N)$ from the \mathbf{v}^1 -dependent distribution in equation (38).
3. Initialize the mechanical circuit to be in its softest state ($k_1, k_2, k_3 = k_{\min}$), and input the \mathbf{A}^i into the mechanical circuit as oscillation amplitudes (equation 36).
4. Observe the spring stiffnesses, k_1, k_2, k_3 , of the mechanical circuit at time $N\Delta T$, and define P^1 as the permutation which orders the spring stiffnesses (equation 37). The zero-memory estimator, P_0^1 , is defined to be the permutation which orders $|A_1^N|, |A_2^N|, |A_3^N|$ (equation 35).
5. Choose a new vector $\mathbf{n}^2 \in \mathbf{R}^3$ and choose \mathbf{v}^2 from the distribution $N(\pi(\mathbf{n}^2), I_3)$ (equation 39). The permutation P^2 orders the components $|v_1^2|, |v_2^2|, |v_3^2|$ (equation 34).
6. Generate a sequence $(\tilde{\mathbf{A}}^1, \dots, \tilde{\mathbf{A}}^N)$ from the \mathbf{v}^2 -dependent distribution in equation (38).
7. Without resetting the mechanical circuit, input the $\tilde{\mathbf{A}}^i$ into the mechanical circuit as oscillation amplitudes (equation 36).
8. Observe the spring stiffnesses, k_1, k_2, k_3 , of the mechanical circuit at time $2N\Delta T$, and define P'^2 as the permutation which orders the spring stiffnesses (equation 37). The zero-memory estimator, P_0^2 , is defined to be the permutation which orders $|\tilde{A}_1^N|, |\tilde{A}_2^N|, |\tilde{A}_3^N|$ (equation 35).

The mechanical circuit thus produces estimates P'^1, P'^2 for permutations P^1, P^2 . Fig. S29F shows the accuracy of these estimates. The circuit recovers P^1 with high probability (Fig. S29F, solid blue circles), whereas the probability that the circuit recovers both P^1 and P^2 is lower (Fig. S29F, solid red circles). This is because the circuit obtains P^1 starting from the initial condition $k_1, k_2, k_3 = k_{\min}$, but when it receives the second distribution, its initial state is biased by the memory of the first distribution. When $|\mathbf{n}^2| > |\mathbf{n}^1|$, the amplitudes of the second distribution are larger, which has the effect of better erasing the memory of the first distribution stored within the mechanical circuit. As a result, the circuit recovers both P^1 and P^2 with higher probability (exceeding 50%) when $|\mathbf{n}^2| > |\mathbf{n}^1|$ (Fig. S29F). In all cases, the circuit recovers the true permutations with much higher probability than the zero-memory estimator (Fig. S29F).

2. Adaptive damping

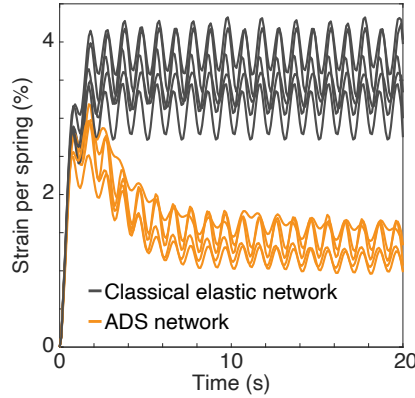


FIG. S30. **Adaptive damping.** A classical elastic network and an ADS network are initialized with identical spring stiffnesses and subject to the same, randomly chosen forcing protocol. Over several such trials, the ADS network distributes strain and thus experiences lower overall strains than a classical non-adaptive network.

In addition to analyzing small mechanical circuits, selected for specific functions, we also investigate large ADS networks chosen at random. In particular, large ADS networks with randomly chosen orientations display striking dynamical differences to classical elastic networks (Fig. S30). To compare these cases, we consider an adaptive and non-adaptive elastic network, where all springs in both networks initially have stiffness k_{\min} . A set of nodes, v_1, v_2, \dots, v_m within the network are chosen uniformly at random to experience an oscillating force. The i 'th chosen node experiences a force $F \cos \omega t (\cos \phi_i, \sin \phi_i)$, so F and ω are the same for each node, but ϕ_i is an angle chosen

uniformly at random. In other words all forced nodes experience the same force magnitude, and oscillate in-phase at the same frequency, but in randomly chosen directions. The stiffening of springs in an ADS network distributes the strain leading to a lower average strain than a non-adaptive network. This effect occurs over several trials (Fig. S30).

E. Simulation parameters

Our numerical results are obtained by simulating equation (33). We use a range of different parameters, demonstrating the robustness of the ADS framework in different regimes. We list the parameters of equation (33) used for various simulations here (correct to 2sf in each case). We also list the frequency, ω of the driven nodes in each simulation. When the nodes have prescribed displacement, the oscillation amplitude A is given, and when the nodes experience an oscillating force, the force amplitude F is given. Finally, we describe the size of the mechanical circuits simulated.

The simulation parameters for main text Fig. 3, Fig. S28 and movie S4 are

$$\begin{aligned} M = 100 \text{ g}, \quad b = 3 \times 10^3 \text{ g s}^{-1}, \quad k_{\min} = 4 \times 10^4 \text{ g s}^{-2}, \quad \frac{k_{\max}}{k_{\min}} = 3, \quad \mu = 0.3, \quad g = 1000 \text{ cm s}^{-2} \\ b_p = 2 \text{ s}^{-1}, \quad \omega_p = 14 \text{ s}^{-1}, \quad \frac{1}{2\ell_p} = 0.1 \text{ cm}^{-1} \\ \gamma = 1, \quad \tau_0 = 0.1 \text{ s}^{-1}, \quad \tau_1 = 1 \text{ cm s}^{-1}, \quad \alpha_0 = \pi \\ A = 1 \text{ cm}, \quad \omega/2\pi = 8 \text{ s}^{-1} \end{aligned}$$

The mechanical circuits shown in main text Fig. 3, Fig. S28 and movie S4 all have width 9 cm to 10 cm (e.g. each ADS in Fig. S28, row 1, column 1 has length ≈ 5 cm).

The simulation parameters for main text Fig. 4A-C and Fig. S29 are

$$\begin{aligned} M = 100 \text{ g}, \quad b = 3 \times 10^3 \text{ g s}^{-1}, \quad k_{\min} = 4 \times 10^4 \text{ g s}^{-2}, \quad \frac{k_{\max}}{k_{\min}} = 15, \quad \mu = 0.2, \quad g = 1000 \text{ cm s}^{-2} \\ b_p = 1 \text{ s}^{-1}, \quad \omega_p = 14 \text{ s}^{-1}, \quad \frac{1}{2\ell_p} = 0.1 \text{ cm}^{-1} \\ \gamma = 0.13, \quad \tau_0 = 1.2 \text{ s}^{-1}, \quad \tau_1 = 12 \text{ cm s}^{-1}, \quad \alpha_0 = \pi \\ \omega/2\pi = 8 \text{ s}^{-1} \end{aligned}$$

The oscillation amplitudes for these simulations vary, as they are chosen from a distribution. Fig. S29D shows the values of A in terms of the ADS length ℓ (see Fig. S29C); the simulations in Fig. 4A-C and Fig. S29 have length $\ell = 10$ cm.

The simulation parameters for main text Fig. 4D and movie S5A are

$$\begin{aligned} M = 100 \text{ g}, \quad b = 6 \times 10^3 \text{ g s}^{-1}, \quad k_{\min} = 4 \times 10^4 \text{ g s}^{-2}, \quad \frac{k_{\max}}{k_{\min}} = 10, \quad \mu = 0.5, \quad g = 1000 \text{ cm s}^{-2} \\ b_p = 2 \text{ s}^{-1}, \quad \omega_p = 14 \text{ s}^{-1}, \quad \frac{1}{2\ell_p} = 0.1 \text{ cm}^{-1} \\ \gamma = 0.75, \quad \tau_0 = 0.1 \text{ s}^{-1}, \quad \tau_1 = 1 \text{ cm s}^{-1}, \quad \alpha_0 = \pi \\ A = 1 \text{ cm}, \quad \omega/2\pi = 8 \text{ s}^{-1} \end{aligned}$$

The ADSs in the mechanical circuits in main text Fig. 4D and movie S5A all have length 10 cm.

The simulation parameters for main text Fig. 4E,F, Fig. S30 and movie S5B are

$$\begin{aligned} M = 100 \text{ g}, \quad b = 200 \text{ g s}^{-1}, \quad k_{\min} = 10^4 \text{ g s}^{-2}, \quad \frac{k_{\max}}{k_{\min}} = 10, \quad \mu = 0, \quad g = 1000 \text{ cm s}^{-2} \\ b_p = 0.1 \text{ s}^{-1}, \quad \omega_p = 0.31 \text{ s}^{-1}, \quad \frac{1}{2\ell_p} = 1 \text{ cm}^{-1} \\ \gamma = 1.3 \times 10^{-4}, \quad \tau_0 = 0.5 \text{ s}^{-1}, \quad \tau_1 = 0.1 \text{ cm s}^{-1}, \quad \alpha_0 = \pi \\ F = 6.5 \times 10^3 \text{ cm}, \quad \omega/2\pi = 0.5 \text{ s}^{-1} \end{aligned}$$

In contrast to the earlier simulations, the oscillating nodes in these large network simulations experience an oscillatory force with amplitude F , so F is listed above, instead of an oscillation amplitude A . The large ADS network in these simulations has width 10 cm. In general, ADS dynamics depends on specific combinations of the above parameter values, so parameters in different ranges can give rise to similar dynamics.

V. SUPPLEMENTARY MOVIES

Supplementary Movie 1: *Physical implementation of an adaptive directed spring (ADS)*. (A) Components of an ADS. (B) Side view of ADS dynamics. Oscillating the ADS from the tail node causes in-phase motion of the pendulum and spring extension, leading to rotation of the elastic ring. In contrast, oscillating the head node produces anti-phase motion, for which the elastic ring does not rotate. This is the hallmark of directionality. (C) Top view of ADS dynamics. (D) Tail node forcing causes the spring stiffness to update: the magnitude of the resulting oscillations changes with spring stiffness.

Supplementary Movie 2: *Origin of directionality in an ADS*. (A) Replacing the elastic ring with a rigid acrylic ring suppresses the spring extension degree of freedom. As a result, the ADS updates under both head and tail oscillations. (B) Reflecting the gear mechanism (insets, top corners) flips the coupling between elastic ring rotation and spring extension, thereby switching the head and tail end of the ADS. (C) The direction-dependent phase locking between the pendulum oscillations and spring extension is robust to noise and insensitive to initial conditions.

Supplementary Movie 3: *Small mechanical circuit experiments*. Measurements of ADS stiffness demonstrate that mechanical circuits can continually adapt. Mechanical circuits can be constructed with rotationally constrained joints (A) or freely rotating joints (B-D).

Supplementary Movie 4: *Landscape of mechanical circuits*. Simulations of mechanical circuits demonstrate the directional adaptivity of each ADS. Force transmission throughout the network is determined by the stiffening and softening of the ADSs.

Supplementary Movie 5: *Adaptive damping*. (A) Forced nodes (white) with large out-degree (multiple outwards pointing ADSs), cause adjacent ADSs to update, thereby distributing strains and forces throughout the network. In the special case where every ADS meets the forced node at their tail-ends, the ADSs fail to stiffen, causing the input force to be effectively caged and leading to larger strains on adjacent edges. (B) Adaptivity distributes loads in large networks with randomly oriented ADSs and randomly chosen forcing nodes (white), leading to smaller overall strains than a non-adaptive network.

-
- [1] J. D. Hartog, Lxxiii. forced vibrations with combined viscous and coulomb damping, *Philos. Mag.* **9**, 801 (1930).
 - [2] N. Makris and M. Constantinou, Analysis of motion resisted by friction. i. constant coulomb and linear/coulomb friction, *J. Struct. Mech.* **19**, 477 (1991).
 - [3] H.-K. Hong and C.-S. Liu, Coulomb friction oscillator: modelling and responses to harmonic loads and base excitations, *J. Sound Vib.* **229**, 1171 (2000).
 - [4] G. L. Wagner and E. Lauga, Crawling scallop: friction-based locomotion with one degree of freedom, *J. Theor. Biol.* **324**, 42 (2013).
 - [5] L. Marino, A. Cicirello, and D. A. Hills, Displacement transmissibility of a coulomb friction oscillator subject to joined base-wall motion, *Nonlinear Dyn.* **98**, 2595 (2019).
 - [6] S. Shaw, On the dynamic response of a system with dry friction, *J. Sound Vib.* **108**, 305 (1986).
 - [7] X. Zhou, C. Majidi, and O. M. O'Reilly, Energy efficiency in friction-based locomotion mechanisms for soft and hard robots: Slower can be faster, *Nonlinear Dyn.* **78**, 2811 (2014).
 - [8] R. Acharya, E. J. Challita, M. Ilton, and M. Saad Bhamla, The ultrafast snap of a finger is mediated by skin friction, *J. R. Soc. Interface* **18**, 20210672 (2021).
 - [9] E. Oja, Simplified neuron model as a principal component analyzer, *J. Math. Biol.* **15**, 267 (1982).